GLANCING-ANGLE PULSED DC MAGNETRON SPUTTERED NANOSTRUCTURED ALUMINUM-DOPED ZINC OXIDE FILMS TO BE UTILIZED AS TRANSPARENT CONDUCTING FILMS

Kittikhun Seawsakul

A Thesis Submitted in Partial Fulfillment of the Requirements for the

Degree of Doctor of Philosophy in Physics

Suranaree University of Technology

Academic Year 2019

ซิงค์ออกไซด์เจือด้วยอลูมิเนียมที่มีโครงสร้างนาโนสำหรับใช้เป็นฟิล์มโปร่งใส
นำไฟฟ้าเตรียมโดยการเคลือบแบบมุมต่ำด้วยวิธีพัลส์ดีซีแมกนีตรอนสปัตเตอร์

นายกิตติคุณ เซียวสกุล

วิทยานิพนธ์นี้เป็นส่วนหนึ่งของการศึกษาตามหลักสูตรปริญญาวิทยาศาสตรดุษฎีบัณฑิต

สาขาวิชาฟิสิกส์

มหาวิทยาลัยเทคโนโลยีสุรนารี

ปีการศึกษา 2562

GLANCING-ANGLE PULSED DC MAGNETRON SPUTTERED

NANOSTRUCTURED ALUMINUM-DOPED ZINC OXIDE FILMS

TO BE UTILIZED AS TRANSPARENT CONDUCTING FILMS

Suranaree University of Technology has approved this thesis submitted in partial fulfillment of the requirements for Doctor of Philosophy in Physics.

Thesis Examining Committee

_____

(Asst. Prof. Dr. Panomsak Meemon)

Chairperson

_____

(Assoc. Prof. Dr. Prayoon Songsiriritthigul)

Member (Thesis Advisor)

_____

(Dr. Mati Horprathum)

Member

_____

(Asst. Prof. Dr. Chinorat Kobdaj)

Member

_____

(Dr. Hideki Nakajima)

Member

_____   _____

(Assoc. Prof. Flt.Lt. Dr. Kontorn Chamniprasart)   (Assoc. Prof. Dr. Worawat Meevasana)

Vice Rector for Academic Affairs   Dean of Institute of Science

and Internationalization

กิตติคุณ เซียวสกุล : ซิงค์ออกไซด์เจือด้วยอลูมิเนียมที่มีโครงสร้างนาโนสำหรับใช้เป็นฟิล์ม
โปร่งใสนำไฟฟ้าเตรียมโดยการเคลือบแบบมุมต่ำด้วยวิธีพัลส์ดีซีแมกนีตรอนสปัตเตอร์
(GLANCING -ANGLE PULSED DC MAGNETRON SPUTTERED
NANOSTRUCTURED ALUMINUM-DOPED ZINC OXIDE FILMS TO BE UTILIZED
AS TRANSPARENT CONDUCTING FILMS) .
อาจารย์ที่ปรึกษา : รองศาสตราจารย์ ดร.ประยูร ส่งสิริฤทธิกุล, 152 หน้า.

ฟิล์มบางโครงสร้างนาโนซิงค์ออกไซด์เจือด้วยอลูมิเนียม /การเคลือบแบบมุมต่ำ / พัลส์ดีซีแมกนีต
รอนสปัตเตอริง

วิทยานิพนธ์ฉบับนี้มุ่งเน้นไปที่การสังเคราะห์ฟิล์มบางซิงค์ออกไซด์เจือด้วยอลูมิเนียมที่มี
โครงสร้างนาโนเพื่อทำการศึกษาและปรับปรุงพัฒนาคุณสมบัติทางไฟฟ้าและทางแสง ที่สามารถ
นำไปใช้งานได้กับฟิล์มประเภทออกไซด์โปร่งใสนำไฟฟ้า (TCO) ในอุปกรณ์ต่าง ๆ เช่น เซลล์
แสงอาทิตย์ LCD และไดโอดเปล่งแสง ฯลฯ ฟิล์มบางซิงค์ออกไซด์เจือด้วยอลูมิเนียมที่มีโครงสร้าง
นาโนนี้ได้ถูกเตรียมบนแผ่น Si ระนาบ (100) และบนแผ่นกระจก ถูกเคลือบด้วยวิธีพัลส์ดีซีแมกนีต
รอนสปัตเตอริง ที่มีมุมในการเคลือบแตกต่างกัน โดยใช้เทคนิคการเคลือบแบบมุมต่ำ (Glancing
angle deposition: GLAD) ขั้นตอนของการสังเคราะห์นั้นมีพารามิเตอร์มากมายที่จะส่งผลกระทบ
ต่อคุณสมบัติของฟิล์มบางซิงค์ออกไซด์เจือด้วยอลูมิเนียมที่มีโครงสร้างนาโน โดยในงานวิจัยนี้ได้
ทำการศึกษาพบว่าค่าของพารามิเตอร์ที่เหมาะสมในการสังเคราะห์มีดังนี้ ปริมาณของอัตราการไหล
ของออกซิเจนที่อยู่ที่ 0 sccm มุมในการเคลือบโดยวิธี GLAD อยู่ที่ 85° ปริมาณของอัตราการไหล
ของอาร์กอนที่ 80 sccm ค่ากำลังไฟฟ้าของระบบสปัตเตอริงอยู่ที่ 125 วัตต์และ ความเร็วในการหมุน
ของฐานรองอยู่ที่ 10 รอบต่อนาที ด้วยค่าที่เหมาะสมของพารามิเตอร์นี้ทำให้ได้ค่าความต้านทาน
ไฟฟ้าและการส่งผ่านแสงเฉลี่ยในย่านของแสงที่ตามองเห็นอยู่ที่ 4.9×10^{-3} Ω.cm และ 87%
ตามลำดับ ในการเพิ่มคุณสมบัติทางไฟฟ้าและทางแสงฟิล์มบางซิงค์ออกไซด์เจือด้วยอลูมิเนียมที่มี
โครงสร้างนาโน นั้นยังสามารถทำได้โดยการอบร้อนในระบบสุญญากาศ ค่าความต้านทานยัง
สามารถลดลงเหลือ 1.708×10^{-3} Ω.cm ในขณะที่ยังคงคุณสมบัติของการส่งผ่านแสงรอบทิศทางไว้

สาขาวิชาฟิสิกส์
ปีการศึกษา 2562

ลายมือชื่อนักศึกษา _____
ลายมือชื่ออาจารย์ที่ปรึกษา _____
ลายมือชื่ออาจารย์ที่ปรึกษาร่วม _____

KITTIKHUN SEAWSAKUL : GLANCING-ANGLE PULSED DC
MAGNETRON SPUTTERED NANOSTRUCTURED ALUMINUM-
DOPED ZINC OXIDE FILMS TO BE UTILIZED AS TRANSPARENT
CONDUCTING FILMS. THESIS ADVISOR : ASSOC. PROF. PRAYOON
SONGSIRIRITTHIGUL, Ph.D. 152 P.

NANOSTRUCTURED AZO FILMS /GLAD / PULSED DC MAGNETRON
SPUTTERING

This thesis focuses on the fabrication of nanostructured aluminum-doped zinc
oxide (AZO) films to study and improve electrical and optical properties, as well as to
employ these films as transparent conducting oxide (TCO) in various devices, e.g. solar
cells, LCDs and light-emitting diodes, etc. The nanostructured AZO films were
deposited on Si wafer (100) and glass substrates prepared by pulsed DC magnetron
sputtering with different deposition angles by glancing angle deposition (GLAD)
technique. The fabrication process has many parameters that affect the properties of
nanostructure AZO films. In this work, it was found that the optimum parameters are
the following: 0 sccm oxygen flow rate, 85° deposition angles, 80 sccm argon flow rate,
125 watts sputtering power, and 10 rpm substrate rotation speed. With the optimum
condition, electrical resistivity and average of the films were 4.9×10^{-3} Ω.cm and 87%
in the visible range, respectively. Improvements in electrical and optical properties of
nanocolumnar AZO films have been demonstrated by post-annealing treatment in

vacuum. The resistivity could be reduced to 1.708×10^{-3} Ω.cm while the films exhibit omnidirectional property.

School of Physics   Student's Signature

Academic Year 2019   Advisor's Signature

         Co-advisor's Signature

ACKNOWLEDGEMENTS

his guidance of XPS and UPS techniques. I also like to thank the BL3.2 staffs for their helps at the beamline.

Finally, I am extremely grateful to my family for their great support and inspiration. My parents helped me with everything and always give me the greatest love.

Kittikhun Seawsakul

CONTENTS

CONTENTS (Continued)

CONTENTS (Continued)

LIST OF TABLES

LIST OF FIGURES

LIST OF FIGURES (Continued)

LIST OF FIGURES (Continued)

LIST OF FIGURES (Continued)

LIST OF FIGURES (Continued)

LIST OF FIGURES (Continued)

LIST OF FIGURES (Continued)

LIST OF FIGURES (Continued)

LIST OF FIGURES (Continued)

LIST OF ABBREVIATIONS

TCO   Transparent conducting oxide

ZnO   Zinc Oxide

AZO   Aluminum doped zinc oxide

ITO   Indium Tin Oxide

eV   Electron volt

GLAD   Glancing angle deposition

DC   Direct current voltage

RF   Radio frequency

Ar   Argon

O   Oxygen

B   Magnetic field

v   Vector velocity

α Deposition angle

φ Angle of substrate rotation

SZDs   Structure-zone diagrams

XPS   X-ray photoelectron spectroscopy

E_K Kinetic energy

W   Work function

UPS   Ultraviolet photoemission

SEM   Scanning electron microscope

LIST OF ABBREVIATIONS (Continued)

FESEM   Field-emission scanning electron microscopy

AFM   Atomic force microscope

TEM   Transmission electron microscopy

UV   Ultraviolet

Vis   Visible

NIR   Near-infrared

R   Reflection

T   Transmission

XRD   X-ray diffraction

GIXRD   Grazing incidence X-ray diffraction

sccm   Standard cubic centimeters per minute

rpm   Revolutions per minute

CHAPTER I

INTRODUCTION

Transparent conducting oxide (TCO) films are essential for current and future optoelectronic devices such as solar cells, flat panel displays, photodetectors, light-emitting diodes (LEDs), smart windows and many others. High quality TCO materials exhibit high transmittance in the visible light region with low electrical resistivity. Both inorganic and organic materials have been developed as TCO materials. The most commonly used materials are Indium Tin Oxide (ITO) and Fluorine doped Tin Oxide (FTO) which are used in LEDs and solar cells, respectively. ITO films exhibit high performance in electrical conductivity with resistivity of about 10^{-4} $\Omega \cdot$cm and high transmittance of about 85% (Hwa-Min et al., 2011). The main disadvantages are the followings. Indium is not an environmental-friendly element. The price of indium is dramatically increasing every day due to a mix-up between the supply and demand of raw materials by the exhaustion of indium source. In addition, amorphous ITO films require low-temperature deposition resulting in the low resistance under moist heat, which leads to a decrease in its conductivity and light transmittance. FTO films exhibit 70-80% total transmittance and 10-15 $\Omega/\square$ sheet resistance, satisfying the basic requirements as TCO materials (Shanting, 2017). In fact, FTO films have some fabrication issues introduced by the difficulty of working with fluorine, and that limits the method for film deposition (Ginley et al., 2010).

Zinc Oxide (ZnO) is one of interesting and promising TCO materials. It exhibits salient properties such as large exciton binding energy of 60 meV, wide optical band gap of about 3.37 eV at room temperature, high thermal and chemical stability. In fact, ZnO is used in various applications. The ZnO production worldwide is approximately 10^5 tons/year. The large fraction of that is used in rubber such as in vehicle tires for heat dissipation and in concrete for increasing processing time and improving the resistance of concrete against water (Floro et al., 2011).

In addition to electrodes, TCOs are dreamed to be used as semiconducting materials for fabricating semiconductor devices. All known TCO materials are naturally n-type semiconductors. Fabricating of high-quality p-type TCO materials has always been the main obstacle in front of the production of fully transparent semiconductor devices (Klaus et al., 2008). The n-type of TCO such as ZnO, SnO_2, and In_2O_3, are key components in a variety of technologies. The development of TCO films could significantly impact a new generation of transparent electrical contacts for semiconductors devices (Liu et al., 2010).

To improve the electrical conductivity and optical transmittance of ZnO thin film, aluminum is doped into ZnO, known as aluminum-doped zinc oxide (AZO). AZO film has attracted considerable attention as an alternative TCO material due to the high conductivity, good transparency, inexpensive, and non-toxic (Proost et al., 2016). In addition, AZO thin film possesses high c-axis orientated crystalline structure (002) that can improve the mobility by reducing the probability of the scattering of charge carriers at grain boundary (Gao and Li, 2008).

Recently, nanotexture, nanorod, and nanowire AZO films have been demonstrated showing an advantage in anti-reflection property, which produces a

gradient-refractive index profile between material and air interface. Generally, the AZO thin film have been developed to deposit including sol gel process, chemical vapor deposition, pulsed-laser deposition, molecular beam epitaxy, magnetron sputtering, etc (Ayadi et al., 2011). Among of these methods, the magnetron sputtering technique has been offered the numerous advantages, including effective control of deposition conditions, non-toxic and ease of scaling up for large-scale production. Magnetron sputtering with glancing angle deposition (GLAD) is a technique widely used for preparation of nanostructured metal and metal oxide. It employs an oblique angle deposition (OAD) and a substrate rotation to fabricate nanostructured thin-film materials with controllable porosity and shape-based on self-shadowing effect and surface diffusion during the deposition process (Horprathum et al., 2013; 2014). The GLAD technique can create the nanostructure by choosing proper substrate temperature, substrate rotation speed, and deposition angle. However, the investigations of the nanostructured AZO film developed from GLAD has only been a few reports (Yildiz et al., 2015; Daza et al., 2019). This report presented the applications of nanostructured AZO films as transparent conductive films.

Research objective

In this research, AZO films were deposited on Si wafer (100) and glass substrates prepared by pulsed DC magnetron sputtering with various conditions, such as oxygen gas flow rates, deposition angle, argon gas flow rates, sputtering power, and rotation speed, to find the optimum conditions. Extensive work involving the characterization for the sample was carried out to understand the effect of various conditions and improve optical and electrical properties on the AZO films. The influence of various conditions on the preparation processes of the AZO films were systematically investigated and discussed in this research. Further improvement of the films was experimented by post-annealing.
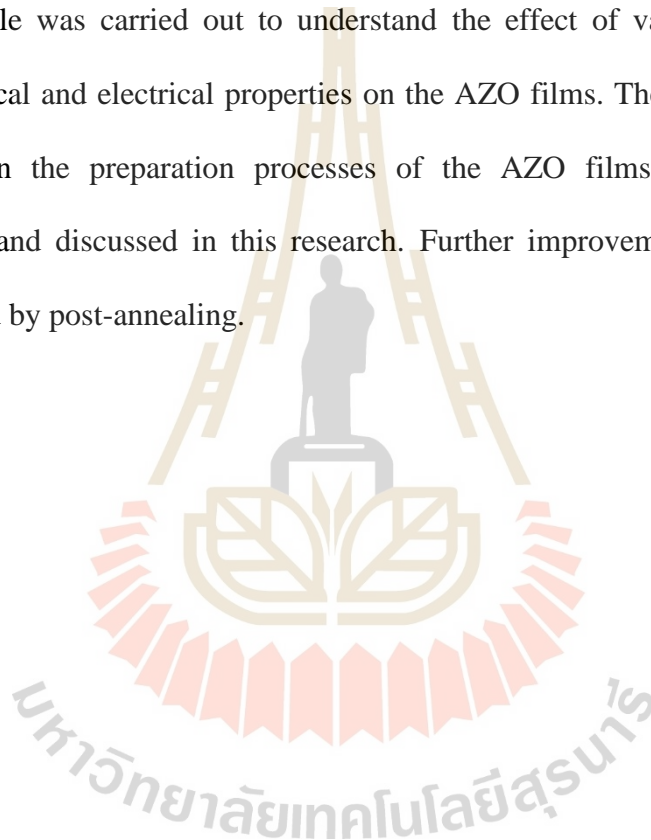
CHAPTER II

THEORY

2.1 Properties of ZnO

ZnO is one of the promising semiconducting materials for the development of optoelectronic devices. Because ZnO has interesting physical properties such as high transparency in the visible and near-ultraviolet (UV–VIS) spectral regions, wide band gap (~3.3 eV) n-type semiconductor with superior electron mobility and high exciton binding energy of ~60 mV and that makes it suitable for applications in short wavelength emitting devices such as light emitting diodes (Proost et al., 2016). It also presents excellent thermal stability, high transparency, pyroelectric and piezoelectric properties, and chemical sensing capabilities that are appropriate for gas detector applications. Aside from its interesting characteristics, it has a relatively low cost and low toxicity. The doping of ZnO films with the group III elements can increase the conductivity of the films. In comparison with other elements, aluminum (Al) and gallium (Ga) are the best dopants because their ionic radii are similar to that of Zn^{2+} (Silva et al., 2014; Tanusevskia et al., 2010).

Un-doped and doped ZnO, and most of the ZnO-based alloys crystallize under normal condition in the wurtzite structure. However, ZnO-based alloys may form in a rocksalt structure for high content of alloying atoms. Thus, a phase transition with change of coordination might occur, resulting in the changes in some physical properties.

The wurtzite crystal structure belongs to the hexagonal system with space group C_{6v}^4 (P6$_3$mc) in the Schoenflies (shot standard) notation. Two atom species occupy the positions of a closest packed hexagonal lattice each. These two sublattices are shifted along the c-axis against each other (Figure 2.1(a)). The wurtzite-structure lattice is fourfold coordinated i.e. each atom has four nearest neighbor atoms. Figure 2.1(b) shows the cuts of different orientations of a crystal with hexagonal structure.
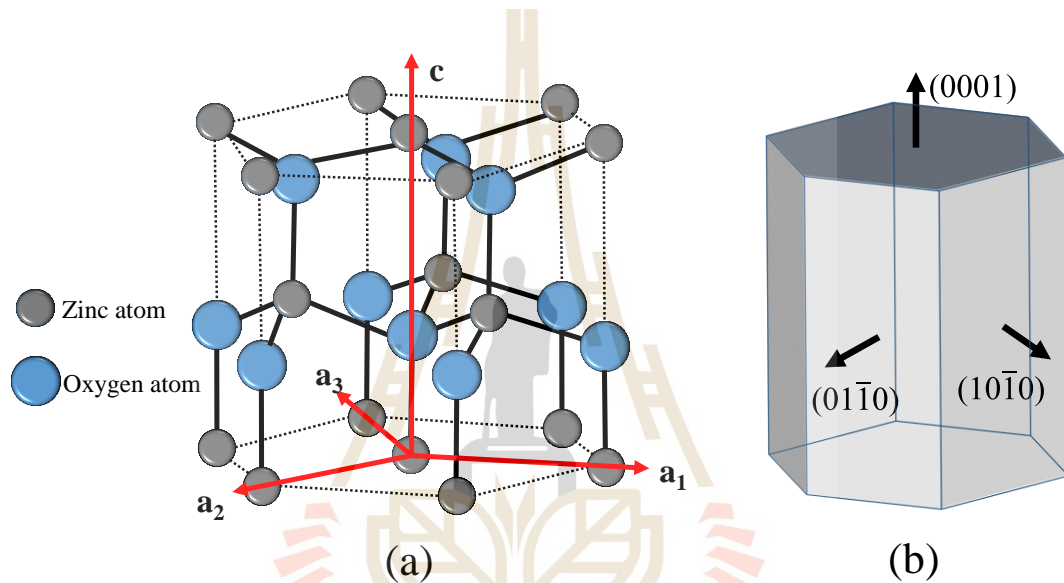
Figure 2.1 (a) The hexagonal wurtzite structure with a red wireframe represented as a unit cell. The zinc and oxygen atoms are tetrahedrally coordinated by sp^3-hybridization. (b) Schematic drawing of surface cut from a hexagonal single crystal with different crystallographic orientation (surface planes).

Lattice parameters of ZnO have been investigated over many decades. The room temperature lattice constants are determined by various experimental measurements and theoretical calculation for the wurtzite ZnO. The lattice constants mostly range from 3.2475 to 3.2501 Å for the a-parameter and from 5.2042 to 5.2075 Å for the c-parameter. The c/a ratio and u parameter vary in a wider rage, from 1.5930 to 1.6035

and 0.383 to 0.3856, respectively. The lattice parameters of a semiconductor can be affected by (i) free electron concentration acting via deformation potential of a conduction band minimum occupied by these electrons, (ii) concentration of foreign atoms and defects and their difference of ionic radii with respect to the substituted matrix ion, (iii) external strains (those induced by substrate), and (iv) temperature. Because the *c/a* ratio also correlates with the difference of the electronegativities of two constituents, components with the greatest difference show the largest departure from the ideal *c/a* ratio. It has been reported that free charge is the dominant factor responsible for expanding the lattice proportional to the deformation potential of the conduction band minimum and inversely proportional to the carrier density and bulk modulus. The point defects such as zinc antisites, oxygen vacancies, and extended defects, such as threading dislocations, also increase the lattice constant, albeit to a lesser extent in the heteroepitaxial layers (Hadis and Ümit, 2009).

2.2 Aluminum doped zinc oxide (AZO) thin films

ZnO thin films function as a highly conductive transparent material was reported by Minami in 1982. Later in 1984, he found that although the pure ZnO thin film is conductive, the thermal stability is not good enough. It became unstable beyond 150°C. At high temperature more than 150°C, the resistivity may not be stable. The pure ZnO films have a lower stability in corrosive, humid ambient due to large amount of oxygen (O) vacancy. The properties of such ZnO thin films are often altered by adsorption of O_2 and water. Another factor limiting the applications of pure ZnO thin films as a transparent conductive film is its thermal instability and high resistivity.

Therefore, ZnO thin films usually are doped with Al. It was found that the ZnO thin film became more stable compared with un-doped ZnO thin films.

Table 2.1 The dopants of elements in zinc oxide.

Element	structure	Doping Content (at.%)	Resistivity ($10^{-4}\Omega$cm)
Al	Al_{zn}	1.6 – 3.2	1.3
B	B_{zn}	4.6	2.0
Ga	Ga_{zn}	1.7 – 6.1	1.2
In	In_{zn}	1.2	8.1

Table 2.1 (Meyer et al., 2005) shows the resistivity, and dopant content for ZnO thin films doped with various dopants. It may be concluded that Al, Ga and B doped zinc oxide has the highest conductivity. Among them, AZO attracts our attention for two reasons: (i) aluminum and zinc are two cheap elements and the reserves are huge, and (ii) aluminum and zinc are non-toxic materials and environmentally friendly.

The potential of mass production of the non-toxic and inexpensive AZO thin film in the future drives us to explore the compromise between optical properties and electrical properties for AZO thin films and its application in solar cells. Namely, AZO thin films are widely used because the films have electrical and optical properties similar to those of ITO, and it is stable in a hydrogen atmosphere. AZO thin films can serve as transparent conductive electrodes because of their low electrical resistance and high transmittance in the visible range of the spectrum. In addition, AZO thin films have an excellent chemical stability and specific electronic properties of a wide band gap (E_g = 3.3 to 3.9) semiconductor. ZnO thin films should be doped by Al, since it has

been remarked that extrinsic donors due to the dopant atom are more stable than intrinsic donors due to the native defects. The electrical conductivity in AZO thin film is higher due to the Al^{3+} ions in substitutional sites of the Zn^{2+} ions and the Al interstitial atoms, in addition to oxygen vacancies and Zn interstitials (Klaus et al., 2008).

2.3 Preparation of AZO thin films

AZO thin films can be prepared by several techniques such as sol gel process, chemical vapor deposition, pulsed-laser deposition, RF-magnetron sputtering and pulsed dc magnetron sputtering (Jimenez et al., 1998; Roth et al., 1981; Lu et al., 2000; Jiang et al., 2003; Chierchia et al., 2014). Among these techniques, however, sputtering offered several advantages as the followings. It permits a high deposition rate with no toxic gas emissions and is easy to adapt for coating on large scale substrates. Moreover, it is relatively low cost and simple to maneuver (Ayadi et al., 2011). For sputtering technique, in the case of large surface deposition, the pulsed DC magnetron sputtering mode is preferable compared to conventional RF due to reduction in the cost of the plasma generators. It is known that the structural, optical and electrical properties of the AZO thin films depend on different deposition parameters (Leem and Yu, 2010).

Thus, this thesis focuses on the pulsed DC magnetron sputtering method since this technique deliver the best films with respect to low resistivity and high transparency. Especially, magnetron sputtering is a technique, which is already used for large area coating deposition in both research and industry. Magnetron sputtering is one of the dominant deposition techniques for the preparation of AZO layers for transparent conductive materials.

2.3.1 Magnetron Sputtering

Magnetron sputtering in a production line has proven to be a high precision and high-rate coating technique based on simple and rugged components. The technique was first employed in the production of metallization of polymer parts for the automotive industry and the metallization of wafer for microelectronics (Waits and Vac, 2000). Today, magnetron sputtering processes are essential for the industrial manufacturing of thin film solar cells, where transparent electrodes and back contacts are deposited by magnetron sputtering. Magnetron sputtering is a high vacuum deposition process where the film-forming atoms are generated by sputtering from a metallic or compound target plate, which is the cathode of a glow discharge process. The sputtered atoms are transported to the substrate through a low-pressure plasma environment. The atoms of the target material are passed into the vapor phase via momentum exchange caused by energetic particle impact rather than by a chemical or thermal process, virtually any material is a candidate for coating. The condensation of mostly neutral atoms and film growth is under concurrent bombardment by energetic species from the plasma, which promotes nucleation, compound formation, and film growth on the substrate. Films containing almost every solid element in the periodic table have been prepared by sputtering. Alloys and compounds can be sputtered such as their stoichiometry are preserved, so oxide films such as AZO materials can be sputtered either reactively from a metallic alloy target, where reactive gas is introduced into the process chamber, or from ceramic compound targets in a pure Ar atmosphere.
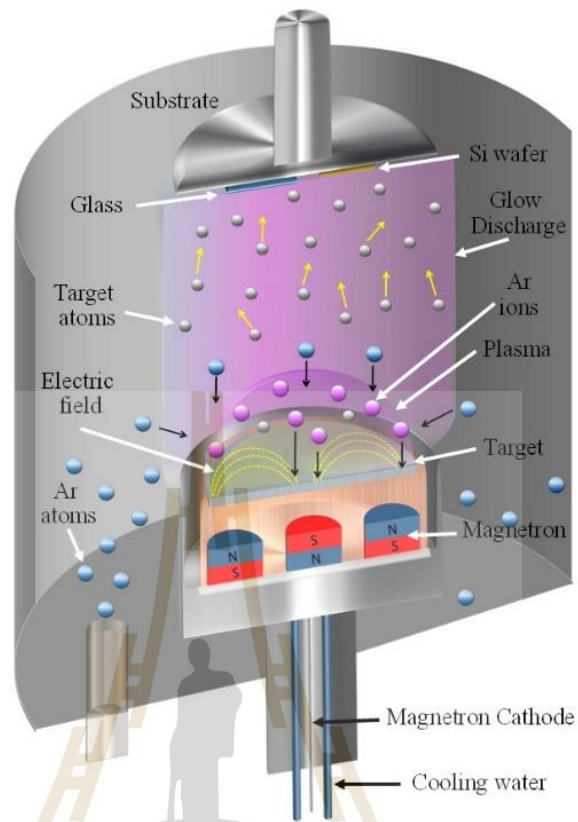
Figure 2.2 The basic components of a magnetron sputtering system. Ionized Ar bombards a target, releasing atoms which form layers on a substrate. Electron and Ar⁺ form plasma, which is located near the target due to the magnetic field, results in greater efficiency and quality.

Figure 2.2 depicts DC magnetron sputtering processes. The electrons that are ejected from the cathode are accelerated away from the cathode and are not efficiently used for sustaining the discharge. By the suitable application of a magnetic field, the electrons can be deflected to stay near the target surface and by an appropriate arrangement of the magnets. The electrons can be made to circulate on a closed path on the target surface. This high flux of electrons creates a high-density plasma from which

ions can be extracted to sputter creates a high-density plasma from which ions can be extracted to sputter the target material producing a magnetron sputtering configuration (Kiyotaka et al., 2012).

The interaction between the magnetic field **B** and an electron with velocity **v** results in a force **F** acting on the electron, where $\mathbf{F} = e\mathbf{v} \times \mathbf{B}$, so that **F** is in a direction orthogonal to both the magnetic field and electron velocity vectors (Figure 2.3). As a result, there is a strong tendency for the electron to travel in an epicycloidal motion close to the target surface where both the magnetic field strength and electron velocity are large. By contrast, the relatively large mass and low velocities of the ions produces much less trapping of the ions, although this can still be a significant effect. By this means of magnetic enhancement, ion fluxes can be increased to several tens of milliamps per square centimeter, with corresponding increases in deposition rates (Krishna 2002).

Figure 2.3 The influence of a magnetic field on the electron trajectory.

2.3.2 Glow Discharge Characteristics

The sputtering target is the cathode of a low pressure glow discharge operating in either in a non-reactive (compound target sputtering in Ar) or reactive atmosphere (elemental target sputtering in Ar/O_2 mixture). High pressure in the order of 5×10^{-2} - 15×10^{-2} mbar is necessary for sputtering without the support of a magnetic field. The target is

subject to an ion bombardment by Ar^+ and O^+ ions, which are cathode sheath toward the target (Chapman, 1980; Raizer, 1991).

2.3.3 Pulsed DC magnetron sputtering

An effective way to prevent arcing during reactive magnetron sputtering (discussed below) is by Appling pulsed voltage. In contrast to RF magnetron sputtering, the pulse frequency is typically 50-250 kHz depending upon the application which is much longer than RF frequency. Generally, the discharge voltage cycles between a high negative voltage and a low positive voltage. The negative voltage part of the cycle is used to perform the sputtering as the ions bombard the cathode. The low positive voltage part of the cycle is used to attract electrons to prevent charge buildup. Due to the higher mobility of the electrons, this part of the cycle can be relatively short compared to the total cycle time. An alternative approach is the use of two magnetron sources, i.e. dual magnetron sputtering and switches the negative and positive voltage between both targets. In this way, each magnetron alternately has the function of a sputtering target and an anode. Thus, both targets can be neutralized during each cycle. This not only prevents charge buildup but also solves problems related to anodes being covered with insulating thin films (the disappearing anode). This helps to eliminate the "disappearing anode" effect found when sputter depositing electrically insulating films with continuous DC power. This technique can be used to reactively sputter non-conductive oxide targets. In sputter deposition using pulsed DC, the optimal frequency pulse duration, and relative pulse heights depend on the material being sputtered and deposited. For example, when reactively sputtering of a good dielectric material such as Al_2O_3, a frequency of about 50 kHz is best, but when sputter depositing of a somewhat conductive film material such as TiN or ITO, a higher frequency (150 kHz)

is best due to the conduction of surface charge away from the surface. The disadvantage here is the higher cost and the fact that power to each target must be turned off before igniting the other target when using mid-frequency ac power supplies. Thus, transients are more severe in this approach. For pulsed DC dual magnetron sputtering, plasma ignition may be required after each half-cycle depending upon operating conditions. Dual magnetron power supplies also require electromagnetic and RF interference shielding (Donald, 2010; Aicha et al., 1998).
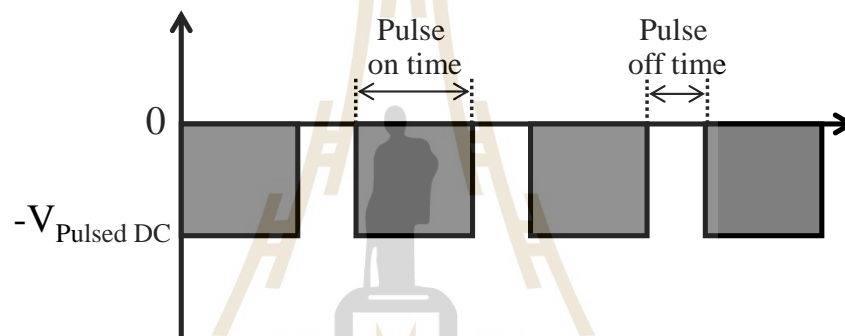
Figure 2.4 Ideal voltage sequence applied to asymmetrical pulsed dc magnetron sputtering of dielectrics.

2.3.4 Glancing Angle Deposition

Glancing angle deposition (GLAD) is a thin film deposition process as a combination of Top-Down and Bottom-Up nanofabrication approaches. GLAD technique provides a method to fabricate nanostructure using existing and prevalent physical vapors deposition processes such as sputtering while requiring only minor modifications to enable carefully controlled substrate tilt and rotation. In the GLAD technique, the substrate is tilted to a glancing angle and does not rotate, thus creating an oblique deposition geometry. Figure 2.5(a) shows the atoms condense on the substrate to spontaneously form nucleation and grow into island. The island growth

prevents incoming vapour from condensing into regions behind the island, causing the island to develop into tilted columns nanostructure at the vapour source direction (Figure 2.5(b)). Hence, the thin film growth from bottom-up aspect of the GLAD process and the shadowing mechanism in an angle deposition geometry cause the condensing vapour to self-assemble into nanostructures.
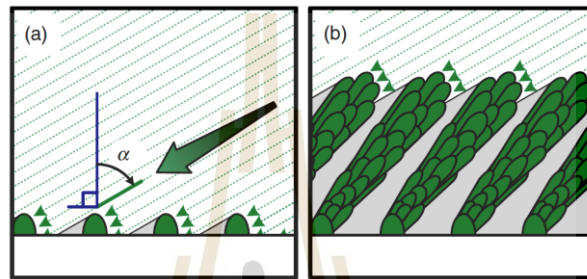
Figure 2.5 The cross-section view of thin-film growth with the GLAD process. (a) The incident vapour of atoms arriving at the surface with an angle α are intercepted by the growing island. (b) These islands capture other surface-adsorbed atoms and develops into a thin film with a tilted columns nanostructure that continue to grow, but shadowed regions are created where no growth occurs (Matthew et al., 2014).

During the substrate rotation, the combining shadowing environment is controlled. GLAD substrate rotation is shown in Figure 2.6. The island has already developed into the nanostructure. The black vapour flux particles on the top of structure turn are those captured by the black helix in the center of the field, slowly grows towards the vapour source to the substrate orientation in the growing nanostructure. As the substrate continues to rotate, the thin film completes additional turns. The substrate rotation speeds and substrate position control the ballistic shadowing effect and guide the nanostructure direction growth.
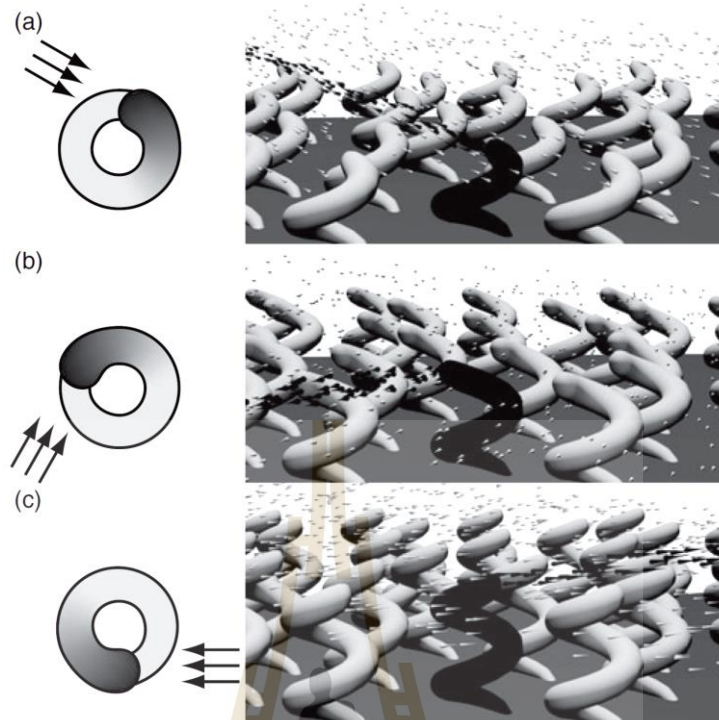
Figure 2.6 The helical film is built up by controlling substrate rotation speed around its axis, shown at (a) one full turn, (b) and (c) continue turns (Matthew et al., 2014).

The substrate position in a GLAD process is specified by two angles. The deposition angle α is defined as the angle between the substrate normal and the incident vapour flux direction. The angle φ measures the substrate rotation about its normal, thus providing the azimuthal position of the substrate. Controlling α and φ provides sufficient rotational freedom to set the apparent vapour source position at any desired altitudinal (controlled by α) and azimuthal (controlled by φ) coordinates, as viewed from the substrate surface (Figure 2.7). The α angle can vary between $0°$ (normal incidence) to $90°$ (parallel to the substrate), whereas the φ angle can assume any value and is periodic (Tang et al., 2003; Alouach et al., 2004).
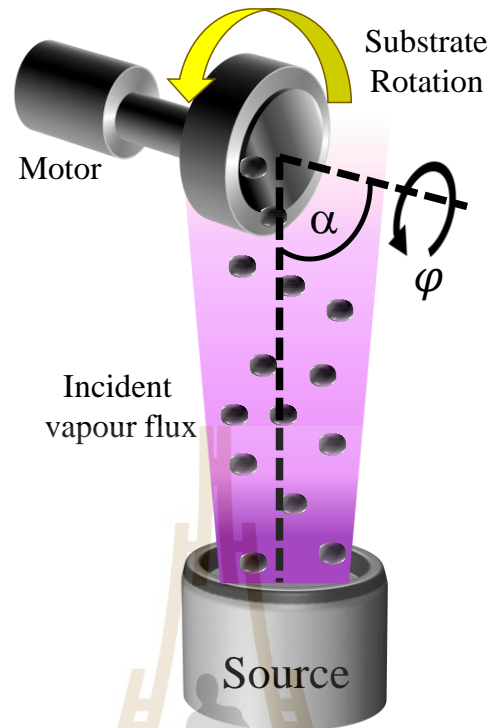
Figure 2.7 The sputtering with GLAD apparatus showing key hardware components.

For AZO nanostructure with different shapes such as tilted rods, vertical rods, spirals, and zigzags can be fabricated by utilizing the GLAD technique in a magnetron sputtering growth unit at room temperature. During GLAD, the flux of the sputtered atoms comes to the surface of the substrate at high angles. At initial stages, atoms form island-like structures on the substrate and shorter islands cannot capture enough flux, whereas longer islands get sufficient flux and continue to grow. The shadowing effect results in the formation of isolated nanostructures through a physical self-assembly process. If no substrate rotation is used, longer islands tend to grow in the flux direction and form the tilted nanorods. If the substrate is rotated around its surface normal axis continuously, then the structures are forced to grow in lateral and vertical directions at different rates depending on the rotation speed (Matthew et al., 2014).

2.4 The structure-zone models

The influence of deposition variables on the structural feature that develops in physically deposited films has been universally depicted in terms of structure-zone diagrams (SZDs). In film grow process, condensation from the vapor involves incident atoms becoming bonded adatoms which then diffuse over the film surface until they desorb or, more commonly, are trapped at low-energy lattice sites. The incorporated atoms reach their equilibrium position in the lattice by bulk diffusive motion. This atomic odyssey involves four basic processes: 1) shadowing, 2) surface diffusion, 3) bulk diffusion, and 4) desorption. The last three are quantified by the characteristic diffusion and sublimation activation energies whose magnitudes scale directly with the melting point (T_M) of the condensate. Shadowing is a phenomenon arising from the geometric constraint imposed by the roughness of the growing film and the line-of-sight impingement of arriving atoms from the GLAD process. The dominance of one or more of these four processes as a function of substrate temperature (T_S) is manifested by different structural morphologies. This is the basis of structure-zone models (SZMs), which have been devised to characterize film and coating grain structures. The SZMs consist of four distinct zones named Zone 1, Zone 2, Zone T ,and Zone 3 shown in Figure 2.8.These zones were established based on the relationship existing between the structure of thin-film and the values of T_S/T_M, indicating that film strength is adversely affected by lattice and grain-boundary imperfections (Milton, 2002).
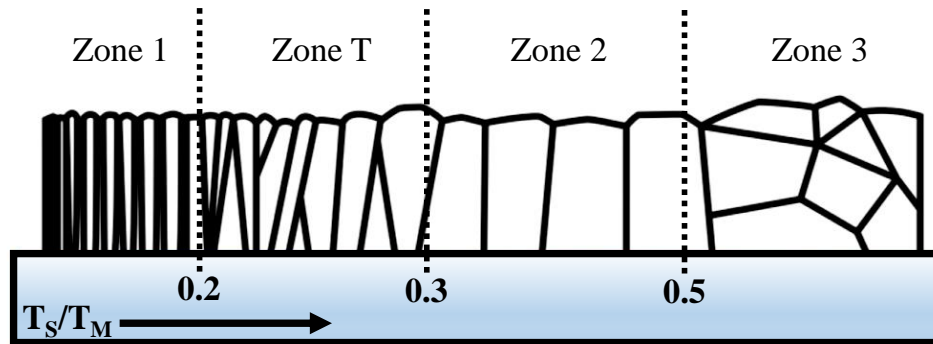
Figure 2.8 Structure zone diagrams for sputtering films.

The thin-film deposit with the low-temperature Zone 1 structures, corresponding to $T_S/T_M < 0.2$, where the result of shadowing effects which overcome limited adatom surface diffusion and unable to fill-in void regions that form in the microstructure. This result is produced by varying the velocity in the growth columns and the angle of the sputtered flux incident at which the atoms from the target reach the surface of the substrate are responsible for the columnar structure in this zone.

A transition zone (Zone T) was introduced between zone 1 and zone 2 ($0.2 < T_S/T_M < 0.3$). This zone is a character of a dense array of poorly defined fibrous grains and formed by grains defined by limits of the low porosity. Films in Zone T exhibit a fibrous texture, as in Zone I. However, Zone T shows no voids and domes, due to the additional adatom transport associated with energetic bombardment, which may be viewed as the transition between zones 1 and 2.

At higher temperatures, the ratio of the T_S/T_M ranges from 0.3 to 0.5 is showed in Zone 2. The surface of Zone 2 appears to be more uniform with an increased grain size width and can be extended in equiaxed form from the substrate interface to film structure. Thus, the film structure consists of columnar grains with defined dense grain boundaries.

Zone 3 represents the region above the ratio of 0.5 for T_S/T_M. Volumetric diffusion processes like annealing and re-crystallization during growth in these zones, which activated bulk diffusion processes, enabling grain boundary diffusion. Due to bulk diffusion processes, enabling grain boundary diffusion, it leads to the structure exhibits equiaxed grains and re-crystallization and produces growth of the grain. Zone 3 determines the last structure of the film, produces a greater crystalline structure and the overall films are very dense. Finally, the film structure transitions gradually between the zones and that other SZMs have been proposed, incorporating additional zones and encompassing the effects of other processing parameters (John, 1987; Messier et al., 1984; Mukherjee and Gall, 2012).

2.5 Characterization of Thin films

2.5.1 X-ray photoelectron spectroscopy (XPS)

In XPS a special form of photoemission is concerned, i.e., the ejection of an electron from a core level by an X-ray photon of energy $h\nu$. The energy of the emitted photoelectrons is then analysed by the electron spectrometer and the data presented as a graph of intensity (counts or counts/s) versus electron energy the X-ray induced photoelectron spectrum.

The kinetic energy (E_K) of the electron is the experimental quantity measured by the spectrometer, but this is dependent on the photon energy of the X-rays employed and is therefore not an intrinsic material property. The binding energy of the electron (E_B) is the parameter which identifies the electron specifically, both in terms of its parent element and atomic energy level. The relationship between the parameters involved in the XPS experiment is:

$$E_B = h\nu - E_K - W \qquad (2.1)$$

where $h\nu$ is the photon energy, E_K is the kinetic energy of the electron, and W is the spectrometer work function. As all three quantities on the right-hand side of the equation are known or measurable, it is a simple matter to calculate the binding energy of the electron. In practice, this task will be performed by the control electronics or data system associated with the spectrometer and the operator merely selects a binding or kinetic energy scale whichever is considered the more appropriate.

The process of photoemission is shown schematically in Figure 2.9, where an electron from the *K* shell is ejected from the atom. The photoelectron spectrum will reproduce the electronic structure of an element quite accurately since all electrons with a binding energy less than the photon energy will feature in the spectrum (Figure 2.10). This is illustrated in Figure 2.10 where the XPS spectrum of lead is superimposed on a representation of the electron orbitals. Those electrons which are excited and escape without energy loss contribute to the characteristic peaks in the spectrum; those which undergo inelastic scattering and suffer energy loss contribute to the background of the spectrum. Once a photoelectron has been emitted, the ionized atom must relax in some way. This can be achieved by the emission of an X-ray photon (X-ray fluorescence). The other possibility is the ejection of an Auger electron. Thus, Auger electrons and X-ray fluorescence are produced as a consequence of the XPS process (John and John, 2003).
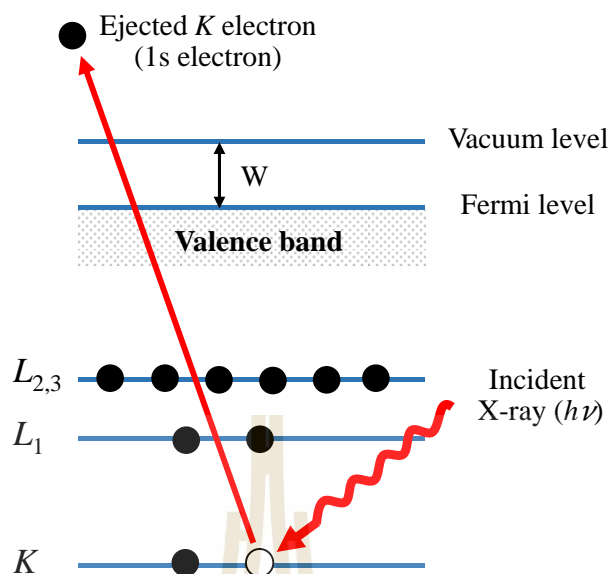
Figure 2.9 Schematic diagram of the XPS process, showing photoionization of an atom by the ejection of electron.
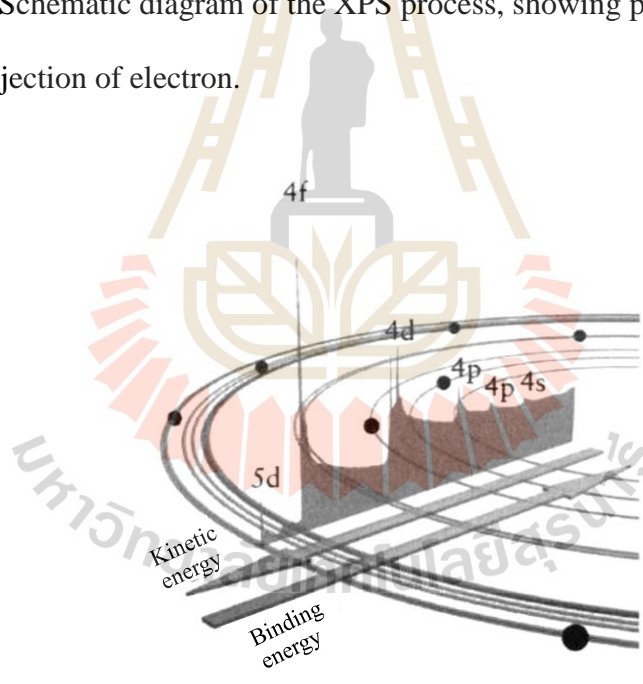
Figure 2.10 Photoelectron spectrum of lead showing the manner in which electrons escaping from the solid can contribute to discrete peaks or suffer energy loss and contribute to the background; the spectrum is superimposed on a schematic of the electronic structure of lead to illustrate how each orbital gives rise to photoelectron lines (John and John, 2003).

2.5.2 Ultraviolet Photoelectron Spectroscopy (UPS) - Work function

The work function is the minimum amount of energy needed to remove an electron from the sample to a point in the vacuum immediately outside the solid surface. The work function of a sample can be measured by photoemission spectroscopy (PES). PES process generates free electrons with a certain kinetic energy depending on the photon energy (hν) to a selected level. The kinetic energy can be detected by electrons photoemitted from the sample and send to the kinetic energy analyzer into the detector. The data are displayed in kinetic energies relative to the Fermi edge of the sample. In a semiconductor, the Fermi level becomes a somewhat theoretical construct since there were no allowed electronic states within the band gap. Thus, the states above the Fermi level do not emit electrons (Schlaf et al., 2001; John and John, 2003).
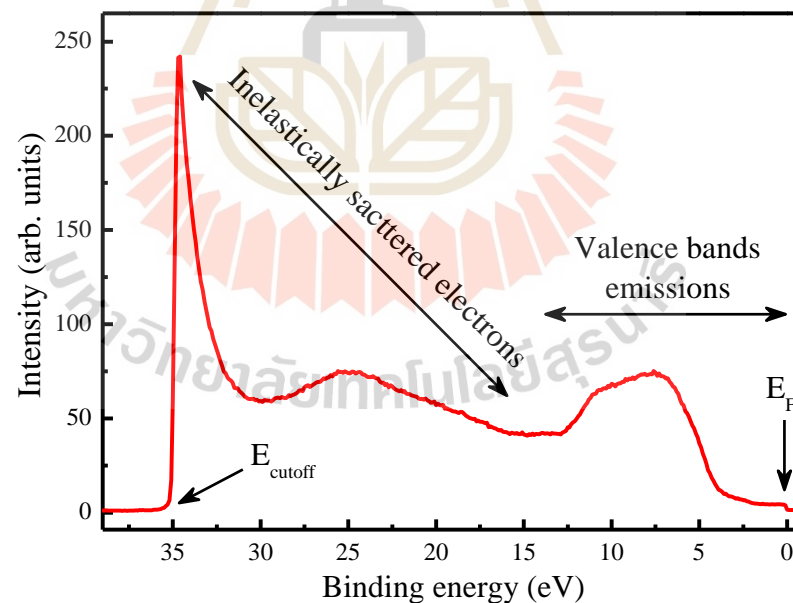
Figure 2.11 UPS spectrum of gold.

Figure 2.11 shows the ultraviolet photoemission (UPS) spectrum of a gold sample. The spectrum can be calibrated with the Fermi level located at 0 eV of binding

energy. The valence bands structures of Au are observed on the right of the spectrum at low binding energies (0-10 eV). The strong peaks correspond to the d-bands of Au, which have a high density of states and are fairly narrow. There is a high binding energy cutoff (secondary edge), where the spectrum ends. Electrons close to the edge were the slowest electrons of the spectrum and have a kinetic energy of zero after leaving the sample surface and had barely enough energy to overcome the work function of the sample.
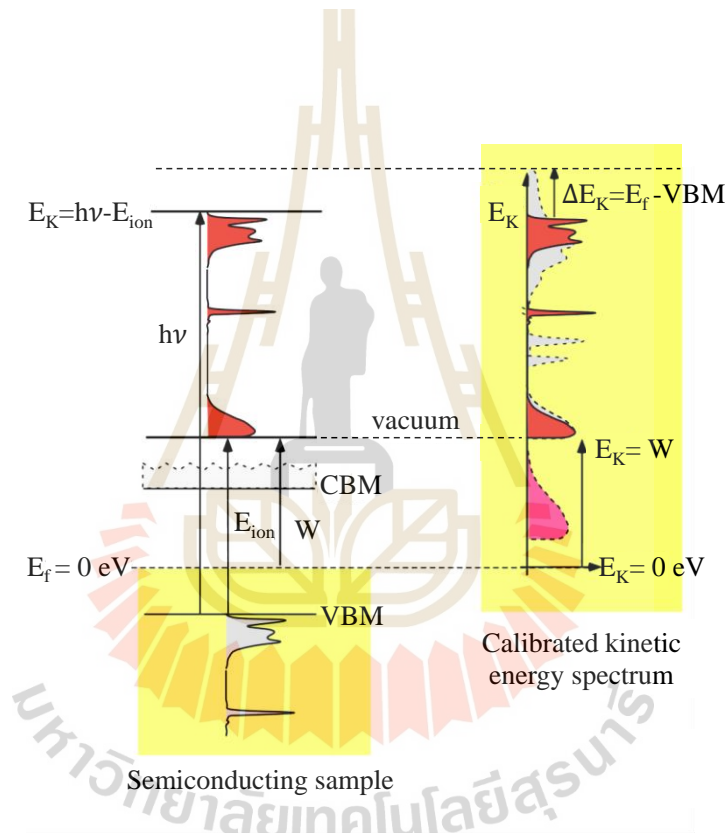
Figure 2.12 Photoemission spectroscopy on a semiconducting sample (By Dr. Rudy Schlaf).

The work function (W) is calculated from the exciting photon energy ($h\nu$), the cutoff (E_{cutoff}) of sample and the Fermi energy (E_F) of Au defined as

$$W = (h\nu - E_F) + E_{cutoff} . \qquad (2.2)$$

In summary, even if there were no electrons right at the Fermi level in a semiconductor, the work function can be measured by PES (Park et al., 1996).

2.5.3 Scanning electron microscope (SEM)

The SEM is an instrument of electron microscope that produces images of a sample by using a focused beam of electrons and reveals levels of detail inaccessible by light microscopy. The electron gun emits the electron beam which is held within a vacuum and moves in vertical travel path through condenser lenses. The electron beam is focused by the objective lens and scans over a specific area of the surface sample with support by scanning coils, which is controlled by the scan generator. The electron beam from an electron gun hits on the sample surface and interact with atoms of the sample by elastic and inelastic scattering in the sample, producing a huge number of signals. These signals are detected by the detector and converted to signals that give detailed information about the surface topography, morphology, composition, the orientation of grains, crystallographic information, etc. about the sample (István Z. J., 2012).
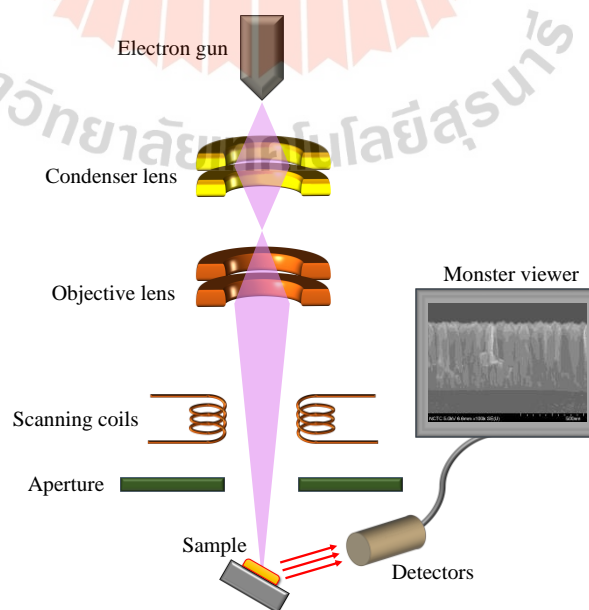
Figure 2.13 The elementary working system of SEM.

Figure 2.14 show the diagram which displays a cross section of the volume of excitation illustrating area from which signals can be detected. The incident electron undergoes elastic scattering, it continues its path after the interaction without losing kinetic energy and velocity remain essentially constant. The result is the generation of backscattered electrons (low resolution of image). The inelastic scattering, the incident electron loses part of kinetic energy and it can activate other electrons or it can excite atoms of the specimen. The result is the generation of phonon excitation (heating), cathodoluminescence (visible light fluorescence), X-ray radiation (elemental composition), secondary electrons (the surface structure of a sample with a resolution of ~10 nm or better) and auger electrons (ejection of outer shell electrons) (Kalsoom et al., 2018; Andres K., 2013).
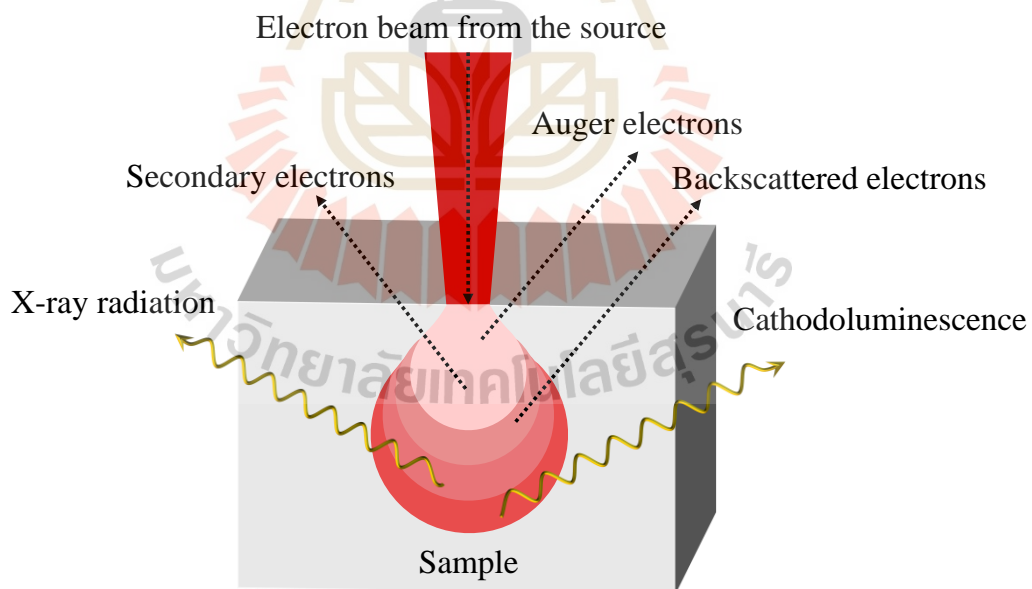
Figure 2.14 The interaction volume of the electron beam and the signals emitted from the sample.

2.5.4 Atomic force microscope (AFM)

Since the development of a scanning tunneling microscope (STM) by Binnig and Rohrer has been rewarded with the Nobel Prize in 1986. During that year, Binnig et al. have developed scanning probe techniques in surface science and the first atomic force microscope (AFM) was invented. AFM is a technique used to study the properties and map the topography of materials on a nanoscale.

The topography of the sample is scanned line-wise (arrow) by a very sharp tip and the tip-sample interaction is recorded with spatial resolution. If the sharp tip and surface of the sample were close to each other, the attractive force deflects the cantilever towards the sample, and when the tip is brought into contact with the sample, the repulsive force deflects the cantilever away from the sample. Thus, the force between a sample and a sharp tip is measured using a laser and a detector to monitor the cantilever motion. The incident laser beam was reflected off the surface of the cantilever, any deflection will cause changes in the direction of the reflected beam into the position-sensitive detector. The detector was sensitive enough to amplify even the very small deflections. The measured cantilever deflections are used to generate a map of the topography of material on a nanoscale. The sample holder can move up and down via a piezoelectric scanning tube so as to maintain the interaction force to a preselected level. The piezoelectric scanner is responsible for the movements between the sharp tip and sample to do imaging in three dimensions.

The interaction force can take effect through very different mechanisms such as van der Waals forces, magnetostatics, electrostatics, capacitance, conductivity, and friction. The AFM technic can be operated in two general modes, the static mode also

known as the contact mode and the dynamic mode (the non-contact mode and the tapping mode) (David B., 2016; Robert A. W., and Heather A. B., 2006).

2.5.4.1 Contact Mode

The sharp tip is adjusted until contact on surface of the sample and the deflections of the cantilever were measured. The scanner moves up and down the relative position of the tip or the sample to maintain a constant deflection and the motion is directly proportional to the sample topography. The advantages of contact mode are fast scanning, good for rough samples and used in friction analysis. The contact mode has a disadvantage on the sample and the sharp tip may experience damages due to normal force and lateral forces during contact mode imaging in the air, the sharp tip has to overcome the effects forces of surface contamination or surface moisture. The result is high contact stresses that can damage either the sample or the sharp tip or both.
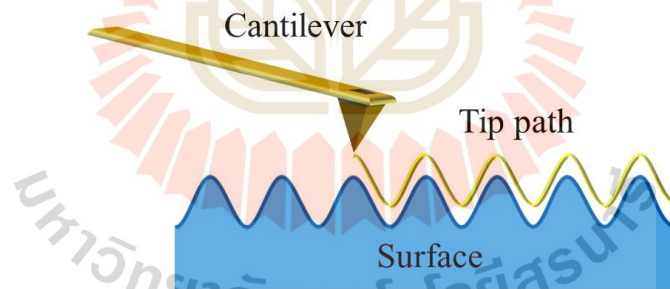
Figure 2.15 Contact Mode, the force on the tip is repulsive.

2.5.4.2 Non-contact Mode

In this mode, the sharp tip does not contact the sample surface but oscillates above the surface during scanning at a distance of about 5-10 nm from the surface sample. The sharp tip is oscillated at near its resonance frequency (about 100 kHz) and amplitude is of the order of 1-10 nm. The interaction forces are very weak on the surface

sample. Thus, the cantilever must be stiffer because this allows the cantilever to have a small bending and a high force sensitivity. For these advantages are good for supported imaging of soft samples. However, the weak force has caused the signal to be small and the contaminant layer on the surface can interfere with oscillation.
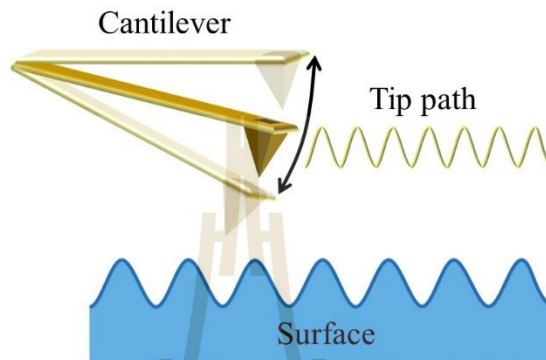
Figure 2.16 Non-Contact Mode; the probe does not touch the sample.

2.5.4.3 Tapping Mode

In the tapping mode, the sharp tip is contacted to the sample similar to contact mode but the cantilever oscillates at the resonance frequency and the oscillation amplitude is 20-200 nm much greater than the non-contact mode. The sharp tip hits the surface for a very short duration at every oscillation cycle. The interaction force alters the amplitude, resonance frequency and phase angle of the oscillating lever. The amplitude of the cantilever is such that the probe maintains enough energy for the sharp tip to tap through and move out of the surface contamination layer. The tapping mode allows high resolution of samples and good for the samples are easily damaged on a surface but slower scan speeds needed.
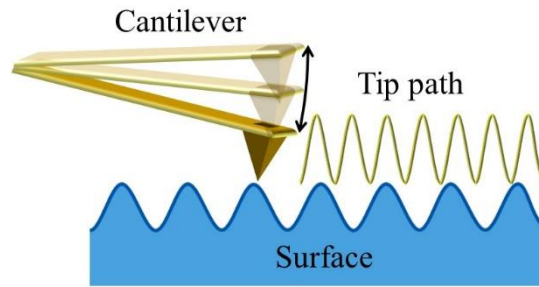
Figure 2.17 Tapping mode; the cantilever makes intermittent contact with the surface in a resonant frequency.

The surface topographical images of the sample obtained by AFM are treated by using the image processing software. The roughness can be characterized by several parameters and determined by the AFM is the root mean square (RMS) roughness (R_q). The R_q is a statistical measure and function R_q defined as

$$R_q = \sqrt{\frac{1}{L}\int_0^L |Z^2(x)|dx} \qquad (2.3)$$

Where $Z(x)$ is the function that describes the surface profile analyzed in terms of height (Z) and position (x) of the sample over the evaluation length L (Bob K., 2017).

2.5.5 Transmission electron microscopy (TEM)

Transmission electron microscopy (TEM) technique is developed to obtain magnification and hence details of a specimen, to a much better level than the conventional optical microscopes. TEM forms a major analysis method in a range of scientific fields, in thin-film, nanotechnology, and semiconductor research. The electron beam of TEM technique is transmitted through an ultra-thin sample followed by a series of lenses, forming a highly magnified image of the sample on a screen and able to achieve a resolution of about 2Å. However, a smaller resolution of TEM image

is maybe the absorption of electrons, the thickness, and the composition of the sample. The alternate modes of use allow for the TEM to determine the position of atoms and observe modulations in chemical identity, crystal orientation, electronic structure and sample induced electron phase shift as well as the regular absorption-based imaging.
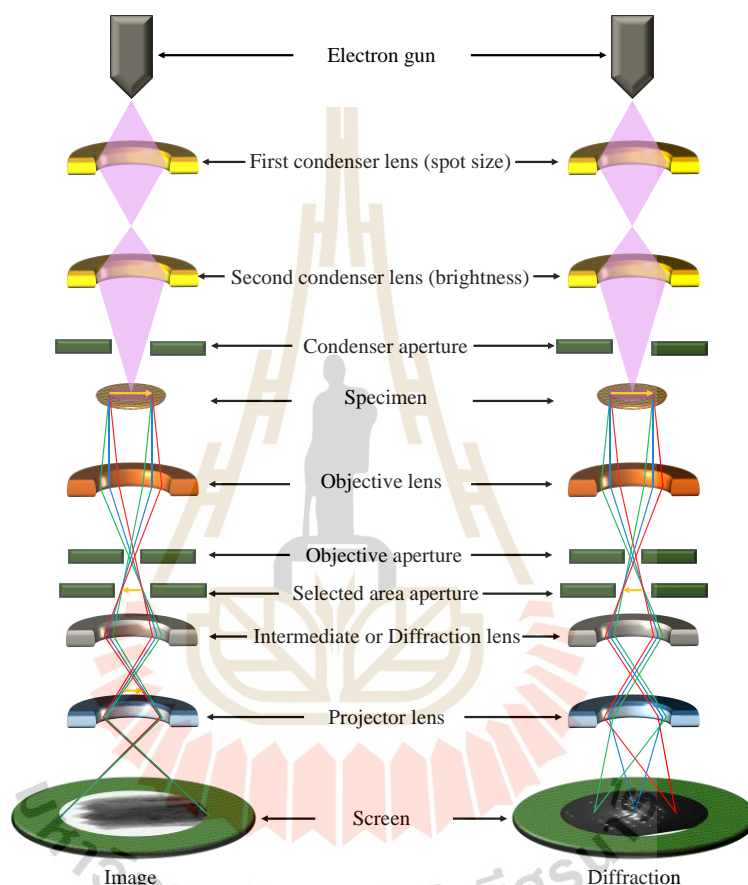
Figure 2.18 The layout of optical components in a basic TEM for image and diffraction modes.

The Figure 2.19 shows the interaction of the electron beam with the sample. When electrons are accelerated up to high energy levels and focused on the sample, they can scatter or backscatter elastically or inelastically, or produce many interactions, resulting in different signals such as X-rays, auger electrons or light. In TEM analysis,

the elastically scattered electrons are mainly used for imaging and inelastically scattered electrons are recorded as well with the imaging device (Peter G., 2011).
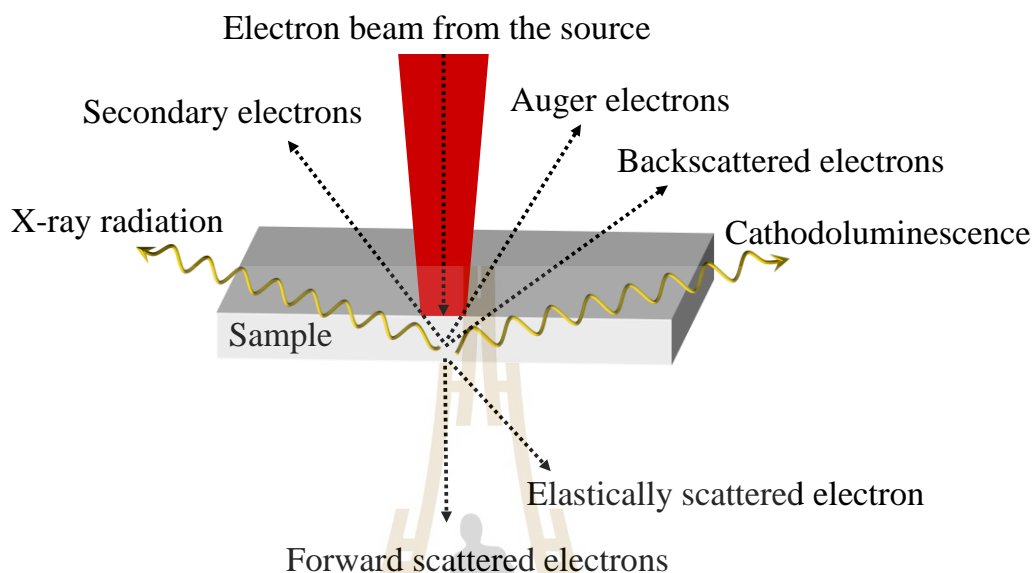
Figure 2.19 The probable interactions between an electron and a specimen.

2.5.6 UV−Vis−NIR Spectroscopy

Optical thin film and coating technologies can be found in applications from research and space optics to consumer items and industry. The various applications of an optical thin film such as eyewear, automotive glass, displays, solar cell, and medical optics. Spectral reflection (R) and transmission (T) are the fundamental measurements for characterizing the optical properties of optical thin films. The performance of optical thin film depends on the specifications of the coating and substrate materials, which can be determined by UV-Vis-NIR spectroscopy with different accessory attachments. UV-Vis-NIR spectroscopy can measure transmission with different angles of the incident light being tested due to the movement of the detector between measurement modes and tilted of the sample holder as shown in the Figure 2.20. The incident light source produces radiant energy in the ultra−violet (UV), visible (Vis) and near-infrared

(NIR) regions of the electromagnetic spectrum. Thus, UV-Vis-NIR spectroscopy is a system designed for applications over the UV-Vis-NIR wavelength range 250–2,500 nm (Travis B. and Farinaz H., 2013).
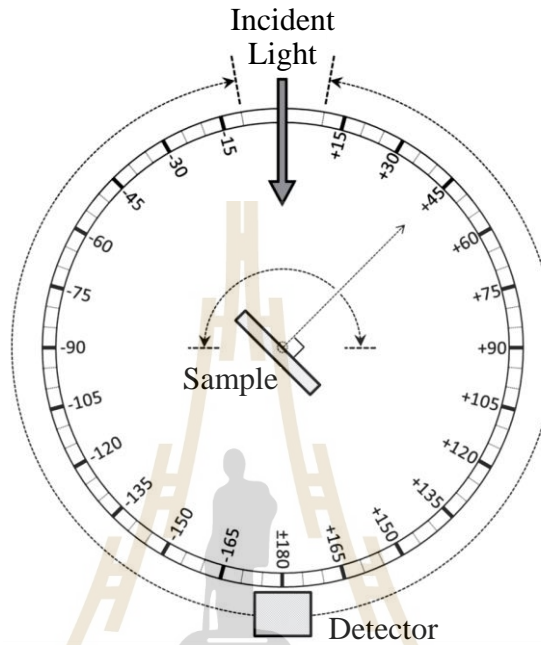
Figure 2.20 The angles of incidence on the sample and the detector position can be set independently with ranges from -85° to 85° (David D. and Farinaz H., 2014).

Figure 2.20, the angle on the sample and the detector position can be set independently. The detector can be placed at angles ranging from -85° to 85°. The instrument operates by passing an incident light through a sample and measuring the wavelength of light reaching a detector. From figure. 2.21 shows the incidence of light has transmittance ($T(\lambda)$), reflectance ($R(\lambda)$) and absorbance ($A(\lambda)$) of a sample placed between two media.
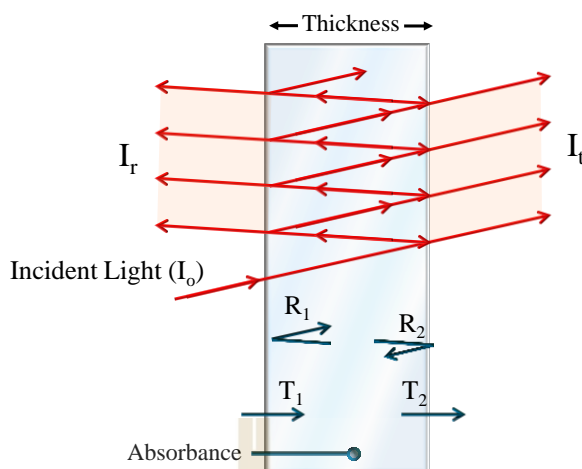
Figure 2.21 Transmission and reflection of light by a plane-parallel sample.

Transmittance is the amount of flux transmitted and reflectance is the amount of flux reflected by a surface. Any flux not reflected or transmitted is absorbed. Analytical information can be revealed in the results of energy in the wavelength range on select. The relationship between transmittance, reflectance and absorbance shown in the conservation of energy requires that

$$T(\lambda) + R(\lambda) + A(\lambda) = 1 \qquad (2.4)$$

The transmittance of the incidence light through a sample placed between two media equals to the light intensity ratio of the transmitted light ($I_t(\lambda)$) and the incident light ($I_o(\lambda)$). The reflectance of a filter ($I_r(\lambda)$) is defined in a similar way with the light intensity of that reflectance. Normally they are shown by percentage of transmittance ($\%T(\lambda)$) and reflectance ($\%R(\lambda)$).

$$T(\lambda) = \frac{I_t(\lambda)}{I_o(\lambda)} \quad , \quad R(\lambda) = \frac{I_r(\lambda)}{I_o(\lambda)} \qquad (2.5)$$

The average percent of visible transmittance (%T_{avg}) can be calculated by equations (2.6) below, using the incidence light transmittance (T(λ)) measured in the wavelength range of 380 – 780 nm. In the equation, E(λ) is the relative solar energy in the table of the standard spectrum distribution of solar energy as specified in JIS R3106 (James M. P., 1995).

$$\% \ T_{avg} = \frac{\sum_{\lambda=380}^{780} T(\lambda) \ E(\lambda)}{\sum_{\lambda=380}^{780} E(\lambda)} \tag{2.6}$$

2.5.7 Hall Effect

The Hall Effect is used for characterization of electrical properties in electrically conductive materials. For semiconductors, Hall Effect measurements are used for determination of the charge carriers, e.g. electron (n-type) or holes (p-type) and density in electrical properties. The Hall element is constructed from a thin sheet of conductive material with output connections perpendicular to the direction of current flow. The Hall Effect is attributable to the Lorentz force which deflects the charge carriers producing an electric current through a sample perpendicularly with respect to the electric field (E) and the magnetic field. If a charge e moves with velocity v through the electric field and the magnetic field then a force $\vec{F}$ acting on electron, given by

$$\vec{F} = e(\vec{E} + v\vec{B}) \text{ for p-type} \tag{2.7}$$

$$\vec{F} = e(\vec{E} - v\vec{B}) \text{ for n-type.} \tag{2.8}$$

The sample subjected to an applied magnetic field (B), it responds with an output voltage proportional to the magnetic field strength. This voltage is used to determine the density and sign of charge carriers in a sample. Thus, an atom in the

crystal lattice of the sample lost its valence electrons and move along the electric field lines with a directed velocity, superimposed on their random thermal velocity. The electrons are accelerated by the electric field but periodically they collide with an atom of the crystal lattice and lose the directed velocity. This fluctuating velocity directed along the field lines, distinct from the thermal velocity ($\tilde{v}$) is called the drift velocity (v_d). So, Electron mobility (μ) is defined as:

$$\mu = \frac{v_d}{E} = \frac{a\,\tau}{E} = \frac{(\frac{E.e}{m})(\frac{\lambda}{\tilde{v}})}{E} = \frac{e\,\lambda}{m\tilde{v}} \tag{2.9}$$

where a is the acceleration of the electrons, τ is the mean time between collisions, λ is the mean free path, e is the charge on the electron and m is the mass of the electron. The drift of the electron in response to the applied voltage gives rise to a current I given by

$$I = neA\mu E \tag{2.10}$$

where n is the number of electrons per unit volume or the electron concentration and A is the cross-sectional area of the conductor. If l is the length of the conductor, the voltage across it is

$$V = El. \tag{2.11}$$

Thus, the resistance (R) from Ohm's law can also be written in terms of the dimensions of the conductor and its resistivity (ρ) is given by

$$\rho = \frac{RA}{l} = \frac{VA}{Il} = \frac{1}{ne\mu} \ . \tag{2.12}$$
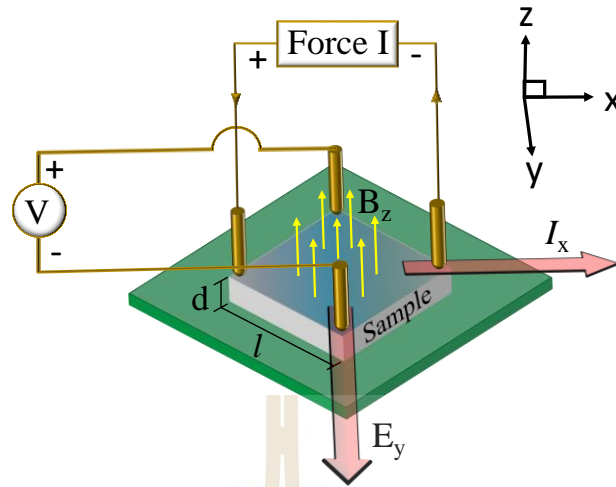
Figure 2.22 The measurement of Hall Effect. Current and voltage are applied between contacts in the presence of a magnetic field.

Figure 2.22 illustrate Hall effect measurements of a sample with applied electric field on x axial and magnetic field on z axial. The Lorentz force is on -y axial. When the Hall voltage has established the force on the electrons is balanced, so that

$$e\mathrm{E}_y = -\mathrm{B}_z e v_x . \tag{2.13}$$

Before $I = neA\mu\mathrm{E}$, the current density J, I and v give their directions. Since $J = \sigma\mathrm{E}$ where σ is the conductivity, can be found as

$$J_x = \frac{I}{A} = \sigma\mathrm{E}_x . \tag{2.14}$$

So, if the current I and magnetic field are known, measurement of the Hall voltage gives the electron concentration n is

$$n = \frac{I}{eA\mu\mathrm{E}_y} = \frac{-\mathrm{B}_z J_x}{e\mathrm{E}_y} . \tag{2.15}$$

Thus, The Hall Effect is a device used to measure mobility, resistivity and carrier concentration of electron in a given sample to allow for more accurate dopant concentration measurements (Hidetoshi F. et al., 1969; Bradley A. G., 2007).

2.5.8 Four -point probe

The four-point probe is a widely used contact technique to measure resistivity or emitter sheet resistance values of any semiconducting materials. It can measure either bulk or thin film specimen. The four-point probe contains four equally spaced tungsten metal probes with a finite radius. The probe spacing in this technique have to be reduced to a micro-scale for obtaining expected surface sensitivity and spatial resolution. Each probe is supported by springs on the other end to minimize sample damage during contact with the surface.
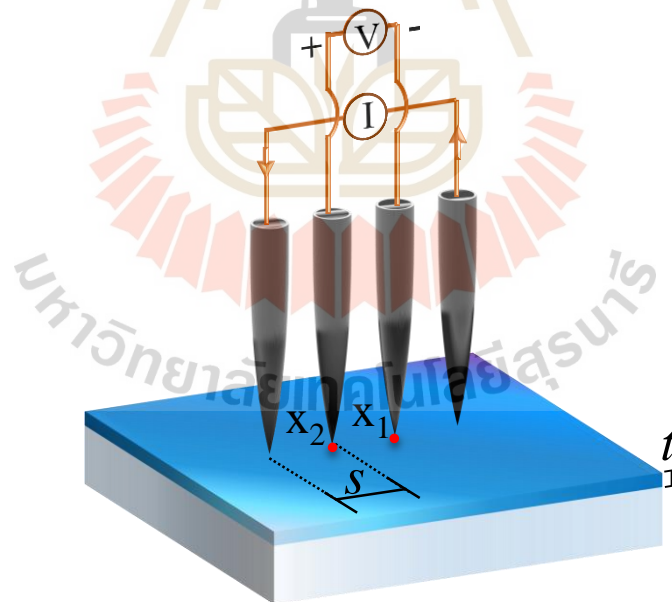
Figure 2.23 Geometry for four-point-probe measurements on a thin layer.

The current probes are used to supply current I through the outer two probes and the voltmeter probes are measured between the two inner probes to determine the

sample resistivity, as shown in Figure 2.23. The separation of current and voltmeter probes eliminates the effect of contact resistance from the measurement result. This is an advantage for the precise measurement of low resistance values.

For the sample of a thin film or the thickness (t) lowest than probe spacing (s) ($s \sim 1$ mm). The current probe gets current rings of current emanating from the outer probe. Therefore, the expression for the area $A=2\pi xt$. The resistance is found to be

$$R= \int_{x_1}^{x_2} \rho \frac{dx}{2\pi xt} = \frac{\rho}{2\pi t} ln\, 2 \; . \tag{2.16}$$

Consequently, for $R=\frac{V}{2I}$, the sheet resistivity (ρ) for a thin sheet is

$$\rho = \frac{\pi t}{ln\, 2}\left(\frac{V}{I}\right) . \tag{2.17}$$

Note that this expression is independent of the probe spacing and frequently used for characterization semiconductor layers (Severin P. J., 1971).

2.5.9 X-ray Diffraction

X-ray Diffraction (XRD) method is useful for determining the atomic and molecular structure of crystallite on an atomic level. X-ray Diffraction effects are observed when electromagnetic radiation impinges on molecular structures with geometrical variations on the length scale of the wavelength of the X-rays radiation. The beam of incident X-rays on the atomic in crystalline structure causes the diffraction many specific directions of radiation. Thus, all the X-rays that came through the receiving slit are collected by the detector. The detector collects X-rays diffraction from an area of the sample by using divergent beam, it is possible to make the intensity to several ten times. The results obtained are plotted with the intensity against the

diffraction angle 2θ. XRD method is useful not only for the structure analysis of crystallite but also for stress analysis, texture and size distribution of crystallite. Thus, it is clear that XRD method is important tool in the field of materials science.
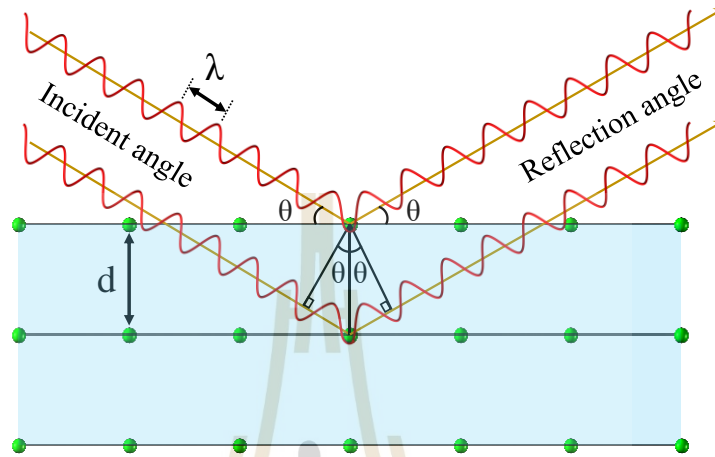
Figure 2.24 Bragg's representation of the diffraction condition as the reflection of X-rays by lattice planes.

In XRD, Bragg's description of diffraction by a crystal is useful to explain diffraction and to provide a mathematical method for computing diffraction directions. Diffraction is described as the reflection of an X-ray beam by crystallographic planes defined by indices the Miller indices of the plane. Thus, Bragg diffraction of different sets of crystallographic planes occurs (Figure 2.24) according to the Bragg equation

$$n \, \lambda = 2 \, d \, \sin(\theta_n) \tag{2.18}$$

where n is an integral number of wavelengths (λ), d is the spacing between the planes in the atomic lattice, and θ is the angle between the incident ray and the scattering planes (Richard J. D. T., 2006; Nicodemus E. W., 2016; Zhdanov G. S., 1965).

2.5.10 Grazing incidence X-ray diffraction of BL7.2W: MX

X-ray diffraction techniques are normally used for determination of crystal structure materials. XRD patterns provide the X-ray intensity as a function 2-theta. In XRD set up, the detector distance and X-ray wavelength are kept constant during the measurements. For ultra-thin film samples, interaction of X-rays with the analyzed films can be enhanced by grazing geometric set up. X-rays impinges on the sample with the angle of incidence near to 90 degrees. This special set up technique is called grazing incidence X-ray diffraction (GIXRD).
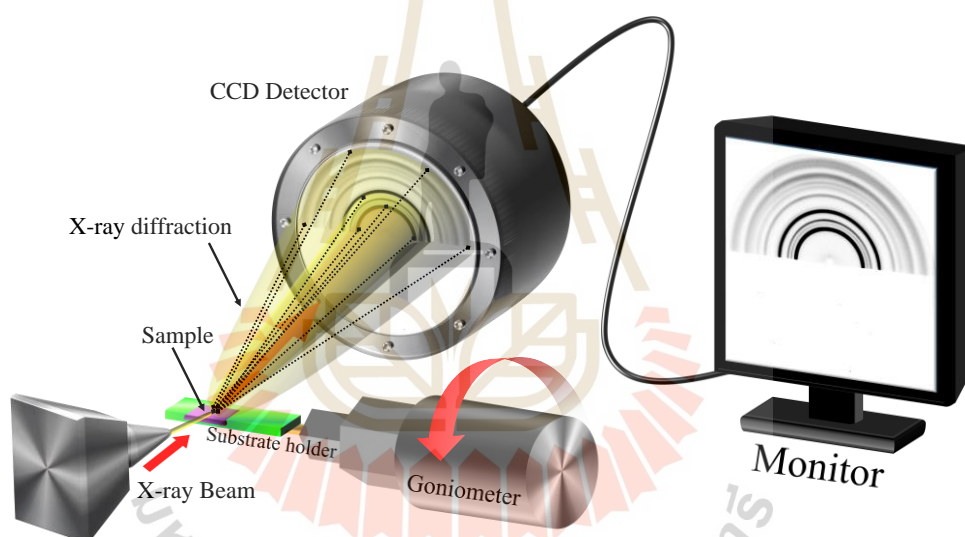
Figure 2.25 The modification of BL7.2W: MX beamline for thin films measure by GIXRD technique.

The GIXRD measurements in this work were carried out at the experimental station of BL7.2W: MX beamline of the Synchrotron Light Research Institute of Thailand. The BL7.2W: MX can be operated with a hard of X-ray energy range of the order of 10^{10} photons/s of photon flux. The XRD techniques apply with the facility of the instrument at the BL7.2W: MX. The major instrument of optical set up in the

BL7.2W: MX such as a cylindrical collimating mirror (CM), a commercial double-crystal monochromator (DCM) and a toroidal focusing mirror (FM) (Klysubun et al., 2010) used to produce and focused of hard X-ray beam with required characteristics for the crystalline studies of thin film. The instrument of the GIXRD measurement at beamline BL7.2W: MX which consists of a cryo-cooler, the substrates holder and Mar165 CCD detector system (Rayonix LLC, Evanston, Illinois, USA). The substrates holder and detector are mounted with a MarDTB Goniometer system (Marresearch GmbH, Norderstedt, Germany). The distance between the substrates holder and detector can be set from 45 to 390 mm for resolution of the X-ray diffraction plane to detect. The substrates holder can be moved and oblique angle to study the crystal plane of thin film growth. Hence, the X-ray diffraction results of this technique depend on the diffraction angle (θ) of the crystals plane in the sample (m) and the distance between the substrates holder to the detector (s). The equation that describes this relationship is

$$\theta = \arctan\left(\frac{m}{s}\right). \tag{2.19}$$

In addition, the double-crystal monochromator (DCM) at BL7.2W: MX can be selected energy of X-ray source, which provides the flexibility of choosing appropriate photon energy for types of experiments (Miskawan S., 2018).

CHAPTER III

EXPERIMENTATION AND METHODOLOGY

The chapter III provides details of experiments for fabrication and characterizations of AZO thin films. The AZO thin films investigated in this work were prepared by pulsed DC magnetron sputtering with Al dropped ZnO. Characterization of the AZO thin films were carried out by using various instruments, e.g. scanning electron microscopy, atomic force microscopy, X-ray diffraction, transmission electron microscopy, macromolecular crystallography, UV-Vis-NIR spectrophotometer, four-point probe, hall effect, X-ray and ultraviolet photoemission spectrometers.

3.1 Instruments and substrate preparation

The pulsed DC magnetron sputtering system used in this research was designed and developed by the Opto-Electrochemical Sensing Research Team (OEC) Laboratory at National Electronics and Computer Technology Center (NECTEC), Thailand. The photo of the system is shown in Figure 3.1.

3.1.1 The sputtering systems

The main power unit for the sputtering system is the DC voltage power supply with tunable power, pulse width (T) and frequency (F). The sputtering chamber is evacuated by a turbomolecular pump backed by a rotary pump, capable of generating vacuum with base pressure down to 5×10^{-6} mbar. Pure Argon (99.99%) gase is the main

gas to feed into the sputtering chamber. The vacuum pressure during sputtering is measured by a Pirani gauge which is connected on top of the chambers.

Figure 3.1 The pulsed DC magnetron sputtering system by OEC laboratory.

In the sputtering system, the magnetron sputter gun is the cathode of a glow discharge process and the substrate holder is the anode. The target size on magnetron sputter gun is 3 inches in diameter and made of compound $ZnO:Al_2O_3$ target with 2% Al_2O_3 by weight. The target is covered by cathode shield and surrounded a magnetic field for controlling the sputtering area.

The cooling water is fed to the magnetron sputter gun for cooling down the target during sputtering. The substrate orientation can be manipulated to allow GLAD technique and oblique angle deposition during film deposition. The sputtered atoms from the target plate are transported to the substrate holder through a low-pressure plasma environment and forming to thin film. The AZO thin film growth depends on ballistic shadowing and formation of columnar microstructures during deposition.

(a)   (b)
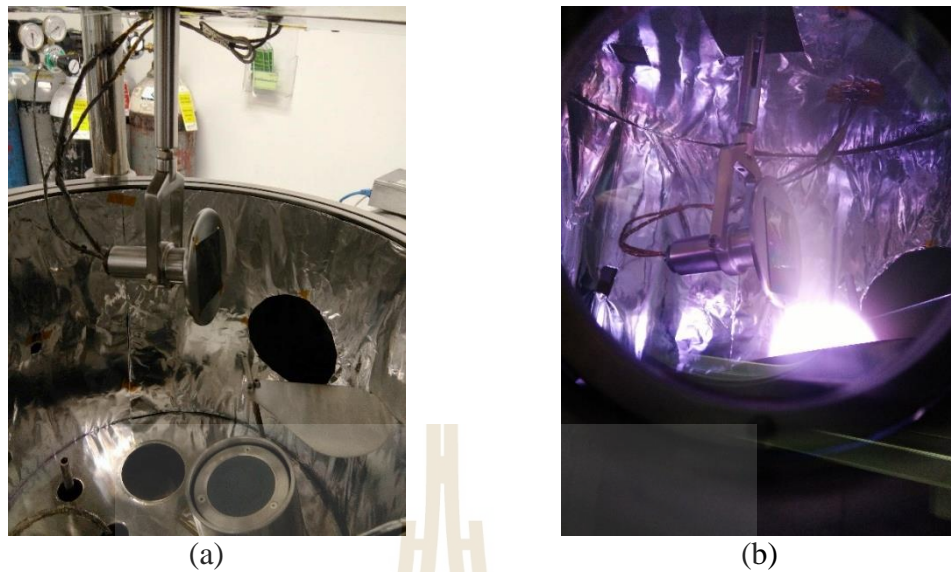
Figure 3.2 The sputtering chamber (a) substrate–target distance and (b) magnetron
sputtering deposition.

3.1.2 Preparations of substrate

The substrates for AZO thin films deposition were silicon wafer (100) and
glass slides. Before fabrication, the glass substrates are cleaned to avoid the formation
of defects in the deposited film because the surface of the substrates might be in contact
with contaminants. The glass substrates were chemically cleaned using the following
procedures. First, the glass slides were cleaned with acetone in an ultrasonic bath to
remove organic contaminants for 15 minutes and then in deionized (DI) water to
remove acetone and decrease charges on glass surface. Second, the substrates were
cleaned by 2-propanol solution in an ultrasonic bath for 15 minutes and then followed
by cleaning with DI water. The 2-propanol solution helps to dissolve oils and remove
oil traces. 2-propanol evaporates quickly and relatively non-toxic, compared to
alternative solvents. Third, the glass slides from step two are cleaned by DI water in an

ultrasonic bath for 15 minutes. Then the glass substrates were dried in nitrogen flow
and in a furnace at 80°C for 5 min before placing them into the deposition chamber.

(a)   (b)

Figure 3.3   Chemical laboratory, (a) cleaning substrates by a chemical in a hood and
(b) equipment for cleaning.

3.2 AZO thin film and deposition condition.

Glass substrates with different dimensions were prepared for different
characterization techniques. Hall Effect and UV-Vis-NIR spectroscopy measurements
require samples with dimensions of 1×1 cm^2 and 2.5×2.5 cm^2, respectively. The silicon
substrates with area about 2 cm^2 were prepared for other measurement techniques. To
prepare AZO thin films, the substrates were transferred to the substrate holder inside
the chamber. The substrates holder can be oriented to allow the angle of deposition to
be varied from 0 to 89 degrees for fabricating nanostructured films. A compound of
ZnO:Al$_2$O$_3$ with 2% Al$_2$O$_3$ by weight was used as the target, the source materials. The
speed of the substrate rotation can be controlled to allow uniformity of thin film. The
base pressure of the deposition chamber is about 5×10^{-6} mbar. Argon flow rate can be
control for the deposition. Before deposition, the target was pre-sputtered about 5
minutes to remove the oxide layer surface of AZO target. After that the shutter was

opened and the deposition started. The operating pressure was maintained in the range at 10^{-3} mbar.

(a)   (b)
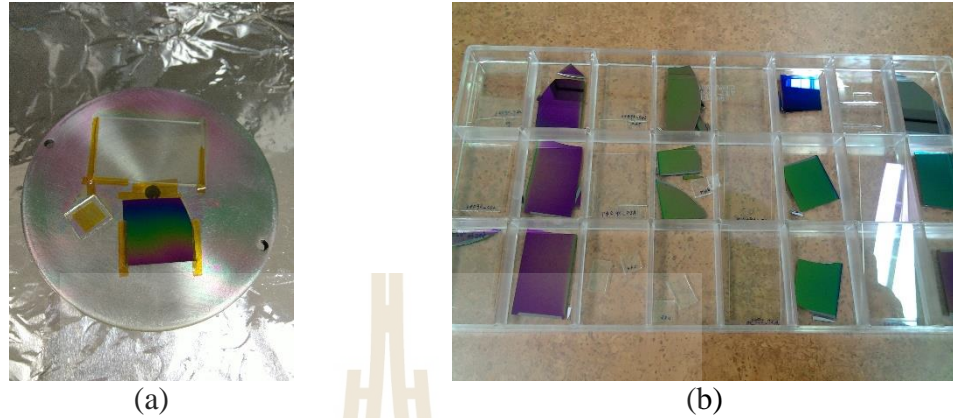
Figure 3.4 (a) Samples on the substrate holder after sputtering and (b) samples preparation with different conditions.

In order to obtain the best possible performance AZO films as TCO materials, the deposition of AZO films was optimized by varying all important deposition parameters, i.e. oxygen flow rate, argon flow rate, deposition angle, DC power, rotation speed of substrate, and post-annealing processes. Table 1 summarizes the lists of values for all parameters investigated in this work.

Table 3.1 List of the values of the deposition parameters studied in this work.

Parameter of study	Condition	
Oxygen flow rate	0, 5, 10, 20, 40 sccm	
Deposition angle	0, 45, 60, 75, 80, 85 degree	
Argon flow rate	40, 60, 80, 100, 120 sccm	
DC power	25, 50, 75, 100, 125, 150 watt	
Rotation speed of substrate	0, 0.02, 0.04, 0.08, 0.16, 1.67, 10 rpm	
	Air	[200, 300, 400°C]
Post-annealing	Low vacuum	[200, 300, 400°C]
	High vacuum	[200, 300, 400°C]

3.3 Physical morphologies and Crystal structures

3.3.1 Filed Emission Scanning Electron Microscopy (FE-SEM)

The physical morphologies were observed by FE-SEM (SU8030, Hitachi) at NSTDA Characterization and Testing Service Center (NCTC) and FE-SEM (S-4700, Hitachi) at Thai Micro Electronic Technology Center Thailand (TMEC) as shown in Figure 3.5. The FE-SEM was used to examine surface and cross-section images of AZO thin films deposited on silicon substrates. The AZO samples were coated with very thin of the platinum layer on the surfaces for a decreasing effect from electron charging during FE-SEM measurements.

(a)   (b)

Figure 3.5   (a) FE-SEM (SU8030, Hitachi) at NSTDA and (b) coatings platinum for insulators or low conductive samples.

3.3.2 Atomic force microscope (AFM)

The AFM (AFM5500M, Hitachi) measurements were carried out at NCTC. AFM is used for the studies of surface topography at nanoscale. The AFM images in this work were obtained in a non-contact mode of measurement. Thus, the cantilever must be stiffer because this allows the cantilever to have a small bending and a high force sensitivity. The cantilevers use in the study topography of the AZO thin films

employed a triangular pyramid-shaped tip (Type: SI-DF40P2). A probe material made of Si with a spring constant of 33 N/m was incorporated into the cantilever. The typical values of the resonant frequency were 300 kHz and the tip-sample interaction was recorded with spatial resolution.

(a)   (b)
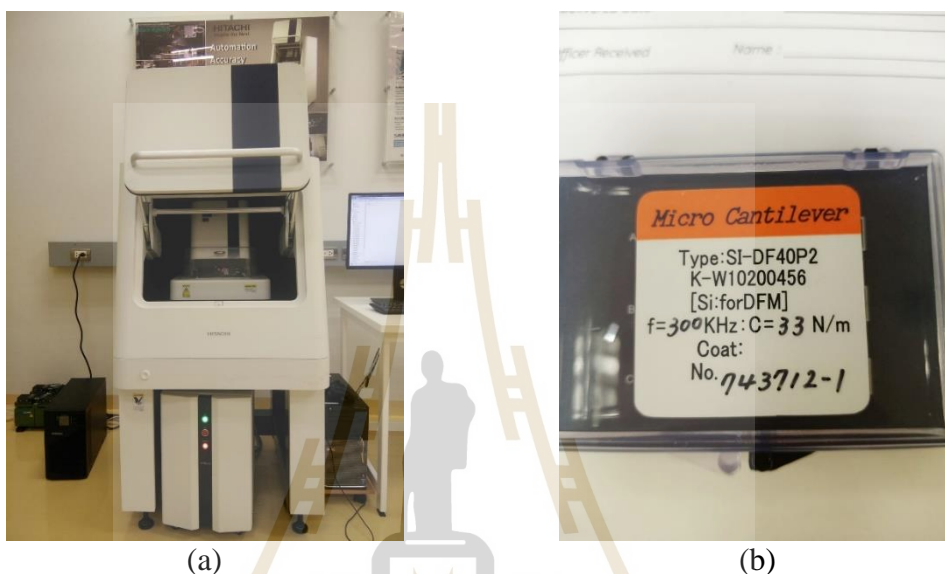
Figure 3.6 (a) Hitachi AFM-5500M at NCTC and (b) AFM probe triangular pyramid-shaped.

3.3.3 Grazing-incident X-ray diffraction (GIXRD)

The crystal structures of the AZO thin films were investigated by the GIXRD technique (Cu Kα radiation, KTTRAXIII, Rigaku) at Material Technology Center Thailand (MTEC), as seen in Figure 3.7. The GIXRD used angle incident mode for thin-film material. The 2-theta angle scans range between 30 to 70 degrees for AZO thin film and stored as an x-ray diffraction pattern to show with the peak intensity. The 2-theta position of peak intensity identifies crystal planes by standard reference from the JCPDS files. Peaks of the crystal planes were used to analyze the full width at half maximum (FWHM) and d-spacing.

(a)   (b)
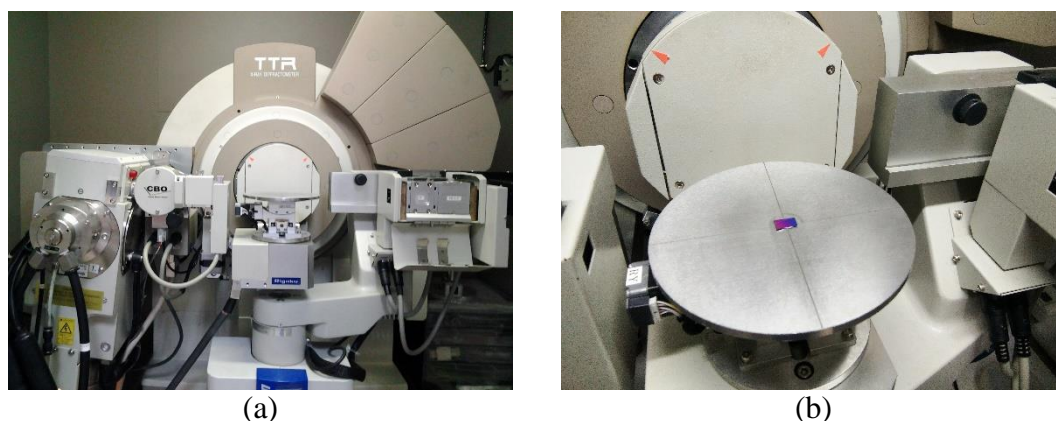
Figure 3.7 (a) The GIXRD technique (Cu Kα radiation, KTTRAXIII, Rigaku) at MTEC and (b) the center position on substrate holder for the sample.

3.3.4 Transmission electron microscopy (TEM)

Transmission electron microscope (TEM, JEOL Model JEM-2010) at MTEC was employed to investigate the structural properties, film crystalline, and chemical composition. TEM was used for taking images with high-resolution lattice image, the selected area diffraction (SAD) pattern, and energy-dispersive X-ray (EDX) spectra, as shown in Figure 3.8. The high-resolution transmission electron microscopy (HRTEM) experiments were performed with an acceleration voltage of 200 kV for observing microstructure. The study of crystalline and orientation by TEM was used for confirming XRD results.

(a)   (b)
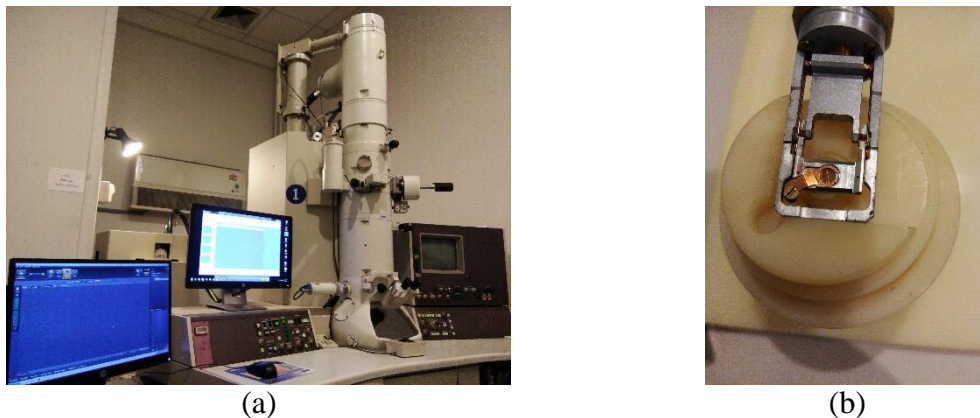
Figure 3.8   (a) TEM (JEOL Model JEM-2010) at MTEC and (b) mounting of TEM grid in grid-holder.

The AZO thin films on silicon substrates were investigated by TEM. AZO films were scraped and attached to TEM grid. Then, a focused ion beam (FIB) electron microscope, as shown in Figure 3.9, was used to prepare TEM samples to be thin enough for observation. The sample on the TEM grid was transferred to a single sample holder and into the column of TEM. Most of electrons in the beam in TEM transmits through the sample. A contrast image was formed on an imaging screen after the electrons transmit through the sample with proper setting of the electron optics in TEM.

(a)   (b)

Figure 3.9   (a) FIB at NANOTEC and (b) monitors for prepare samples.

3.3.5 Synchrotron light beamline: BL7.2W: MX

The photon energy of the BL7.2W: MX available was between 7 to 18 keV. The detector and sample holder were manipulated with the MarDTB goniometer system and can be controlled by a computer. The first step of measurement was to align the X-ray beam, and the position on the sample exposing the X-rays on a burning paper. After that, the distance from position of the detector to sample was calibrated by using a 4-bromo benzoic acid as a reference sample, the sample with known lattice constant. 2D diffraction pattern can be analyzed by using SAXIT programs (Miskawan S., 2018).

(a) (b)

Figure 3.10 (a) Set up for GIXRD measurements at the BL7.2W: MX beamline and (b) "Zoom-in" photo of GIXRD set up showing the sample holder.

3.4 Optical transmission

The optical properties of the AZO films were studied by using the UV-Vis-NIR spectrophotometer (Cary 7000, Agilent) at NECTEC laboratory, as shown in Figure 3.11. The AZO thin films were deposited on large glass slides with dimensions of about 2.5×2.5 cm^2. This large samples were due to the hole of the sample holder is of 2.0 cm in diameter for the incidence of light transmitted. The light transmittance was measured in the wavelength ranging from 200 to 2,200 nm with fixed position of the detector.

The wavelength from 380 to 780 nm was taken into account when calculating the average transmission values of the prepared AZO thin film in the visible region. The data was collected using the Cary 7000 UMS, which is a highly automated variable angle absolute specular reflectance and transmittance system. The instrument is equipped with independent motorized control over the angle of incidence onto the AZO thin film and the position of the detector, which can be freely rotated in an arc around the sample for omnidirectional anti-reflection measurement. The properties of omnidirectional anti-reflection were measured in visible wavelength with an angle of incidence between -80 and 80 degrees. The independent control of sample rotation and detector position was follow setting and unattended measurements. The data from the UV-Vis-NIR spectrophotometer was in the Excel file format. They include the relationship between percent of transmittance and wavelength for transmittance properties or incident angles for omnidirectional anti-reflection measurement.

(a)   (b)

Figure 3.11 (a) UV-Vis-NIR spectrophotometer (Cary 7000, Agilent) at NECTEC and (b) A multi-sample holder.

3.5 Electrical properties

3.5.1 Four-point probe

The elementary method for check electrical properties can be performed by using the four-point probe (RM3, Jandel) technique at OEC laboratory, NECTEC. The four-point probe system is a combined constant current source and digital voltmeter, which connected to high voltage. The unit of voltage or the sheet resistance of the AZO thin films in ohms/square ($\Omega/\square$), depending on which function is chosen. The probe head is material is made of tungsten carbide with 50 μm tip in radius and probe spacing of 1 mm, in which the probe head can easily be damaged. Thus, voltage and sheet resistance can be measured on glass samples ranging from 5×5 mm^2 to 5 diameter area. Before the measurements, the voltage or sheet resistance must compare measurement values by a device under test with an ITO standard sample of calibration and selecting program settings for the appropriate sample. The operating was to move probe head to contact on a sample surface, the apply current source and measure sheet resistance. After that, the probe head must be lifted all the way up to the lock position. The sample can be moved out and, then, anew sample can be loaded.

<div align="center">(a)   (b)</div>
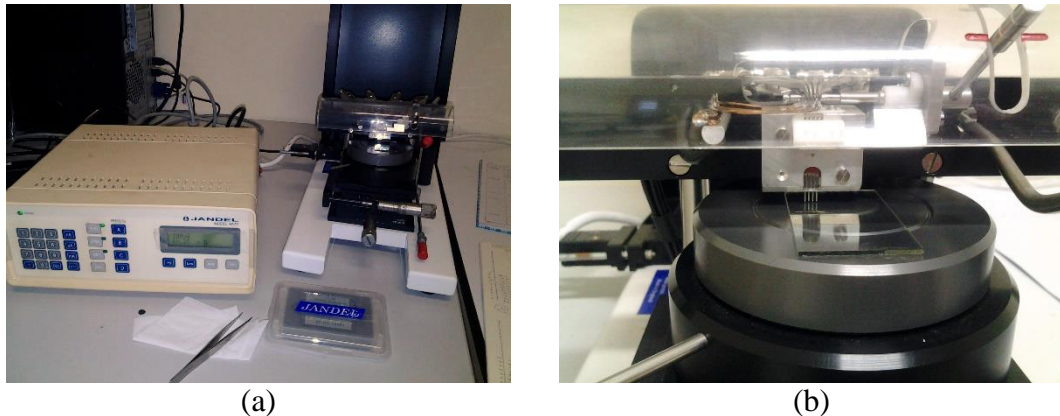
Figure 3.12 (a) Four-point probe (RM3, Jandel) at OEC laboratory, NECTEC and (b) four-probe contact on the sample.

3.5.2 Hall-Effect measurement

The electrical properties of AZO thin films on glass substrates of 1×1 cm^2 in area were measured at room temperature by Hall-effect measurements (Ecopia HMS-300) at OEC laboratory, NECTEC. The Hall-effect system was used for measuring resistivity, mobility, and carrier concentration, as shown in Figure 3.13. The SPCB-1 (Spring clipboard) is the sample holder for usage with the 0.55 Tesla magnet kit and it has spring-loaded clips to make contact on the sample. It was applied to Magnetic flux density input and constant current source supply system. The system is possible to test various sizes of samples ranging from 5×5 mm^2 to 30×30 mm^2, and the maximum thickness sample of 5.5 mm. The HMS-3000 includes software with I-V curve capability for checking the ohmic integrity of the sample contacts. The systems can be used to characterize samples such as thickness and input value for measurement on the computer display monitor. Then the system automatically applies and switches the input current, measures the voltages, and moves the magnets 0.55 Tesla by the user. The magnetic flux density is from a permanent magnet. The measurements were carried

out at room temperature. The software shows the I-V Curve and I-R Curve. The graphical data show the characteristics of current versus voltage and current versus resistance between each terminal by the 4-point probe test method. Various data can be calculated automatically at once, e.g. bulk carrier concentration, mobility, resistivity, conductivity.

(a)   (b)
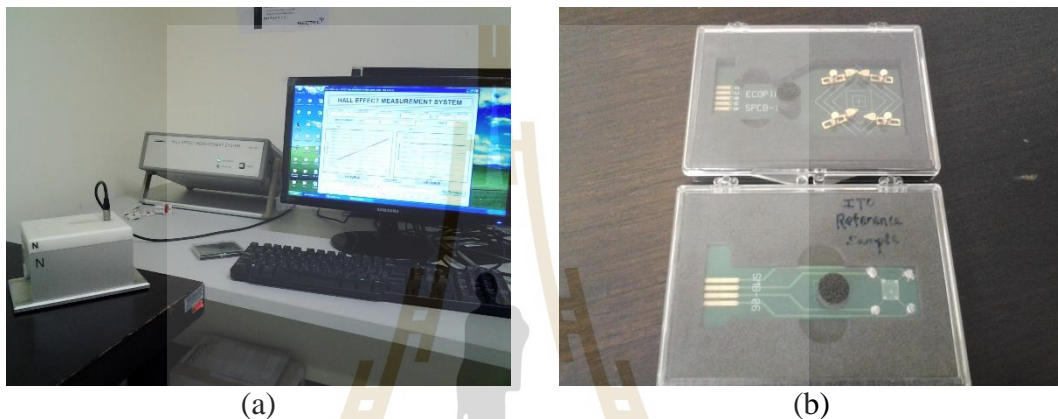
Figure 3.13 (a) Hall-Effect (Ecopia HMS-300) at OEC laboratory, NECTEC and (b) sample calibration and holder.

3.6 BL3.2Ua: Photoemission Spectroscopy (PES)

The work function of the AZO thin films on silicon substrate was measured by using ultraviolet photoelectron spectroscopy (UPS). The chemical bonding states of AZO thin films were identified from XPS spectra. Both UPS and XPS measurements were performed at the BL3.2Ua: PES (Photoelectron Emission Spectroscopy) beamline of the Synchrotron Light Research Institute of Thailand, as show in Figure 3.14(a). The electrons are produced by a thermionic electron gun then accelerated by 2,856 MHz high power microwave in the linear accelerator (LINAC). The LINAC is used to generate an electron accelerator of a 40 MeV electron and transported to the booster synchrotron and accelerated to 1.2 GeV. The Synchrotron source electron beam energy

is 1.2 GeV, and the electron current injected for each operation cycle is 150 mA. The

beam emittance is 41 nm-rad, and the beam lifetime is approximately 12 hours at 100 mA.

| (a) | (b) |
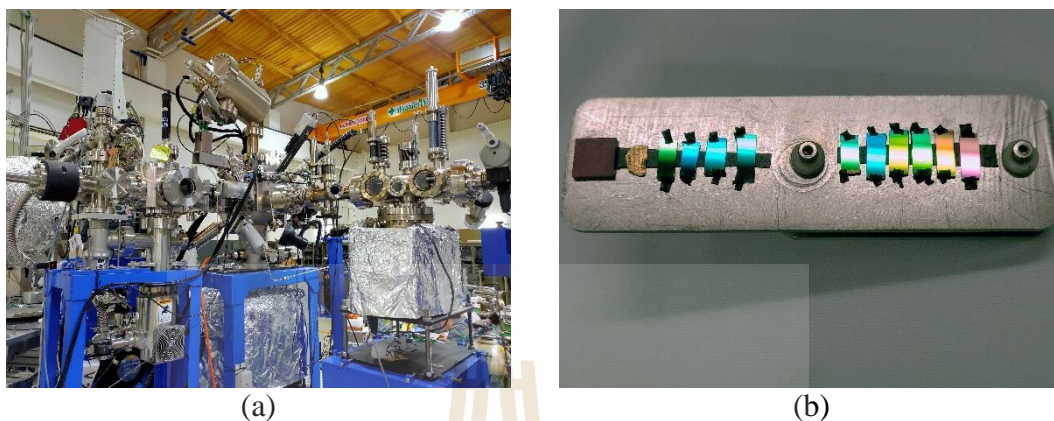
Figure 3.14 (a) UPS and XPS measurements at BL3.2Ua: PES beamline and (b)

fluorescent, gold, and thin-film sample on the sample holder.

The AZO thin film was prepared on the substrate holder and the sample scale

area must be more than 5×5 mm^2 when compare to beam size. Figure 3.14(b) shows

the schematic of sample placement on the substrate holder for measurement.

Fluorescent and gold samples on the substrate holder are used for checking the beam

position and for reference, respectively. Part of the top of the sample is covered with

stripes of conducting carbon tape in order to prevent the electric charging of the AZO

thin films.

The procedures for PES measurements are summarized as the followings. First,

the position of the excitation beam on samples was checked with the zero-order light

incident on the sample area. One could observe by bare eyes. Photon energy was chosen

by a monochromator equipped with three gratings, i.e. Grating#1 with 600 lines/mm

for 40-160 eV, Grating#2 with 1200 lines/mm for 220-520 eV and Grating#3 with 2400

lines/mm for 440-1040 eV. Grating#1 is used to select the excitation photon energy at

39.5 eV for the measurements of the cut-off energy and the valence band maximum of AZO thin film. Grating#2 used to select the excitation energy of 650 eV for XPS measurements covering the Zn3d, O2s, and Al2p XPS spectra. Before taking data, parameters for data acquisition were defined in the data acquisition software. The spectra of photoelectron were shown on the display of the data acquisition system. Data analysis to obtain the work function and elemental composition was carried out using commercial software.
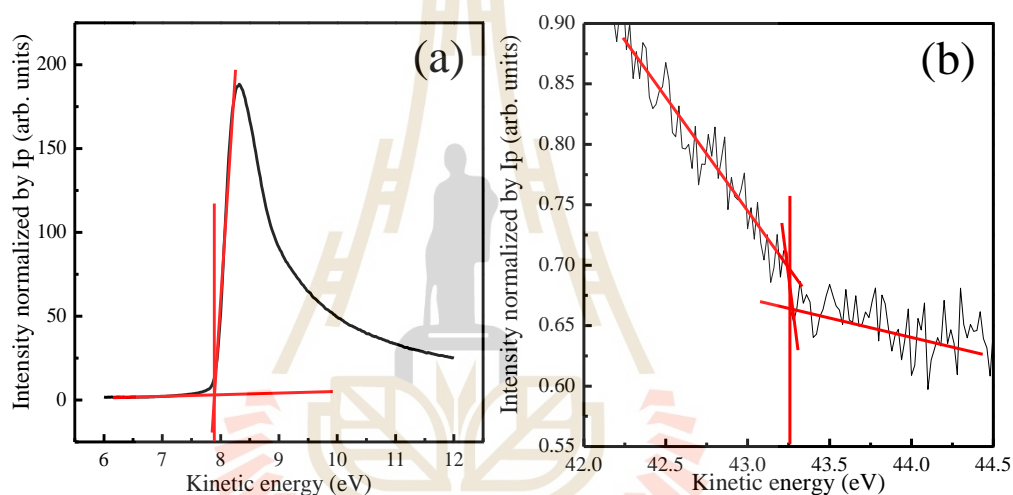
Figure 3.15 (a) The low kinetic energy cut-offs and (b) the Fermi level measured by UPS.

It is noted that the samples were negatively biased for the work function measurements. The determination of the position of inelastic cutoff was unambiguous for all samples (Figure 3.15(a)) while the Fermi edge did not readily show up for some samples. However, this did not pose a problem because the Fermi edge is the reference point of energy scale in photoelectron spectroscopy and should not change from sample to sample as long as they were grounded. Thus, the Fermi edge could be checked the position by using Au sample (Figure 3.15(b)) electrically connected and positioned next to the AZO film sample.

3.7 Annealing system

The electrical properties of AZO thin film were improved by post-annealing. In this work, different annealing conditions/processes were carried. Post-deposition annealing was carried out in a quartz tube furnace at the temperature of 200, 300 and 400°C for 3 hours under three different environments, i.e. in air, low vacuum (1×10^{-3} mbar) and high vacuum (5×10^{-6} mbar). The ramping rate of the temperature was kept at 4°C/min. After each post-annealing time, the sample required cooling-down time in a quartz tube. The samples were kept in the desiccator before measurements.
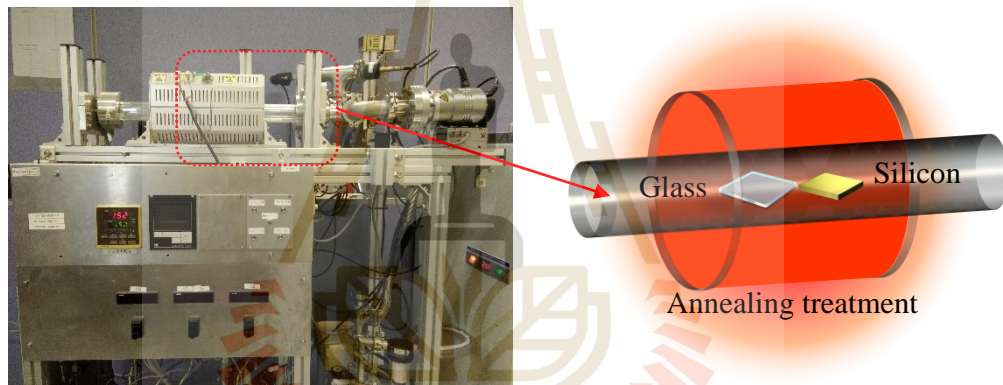
Figure 3.16 The post-annealing treatment equipment using the tube furnace with quartz-tube.

CHAPTER IV

RESULTS AND DISCUSSIONS

This chapter presents experimental results obtained during the course of this thesis work. The main tasks focused on finding the optimum conditions for AZO film deposition to provide the best possible TCO materials properties. The main parameters studied include oxygen gas flow rates, deposition angle, argon gas flow rates, sputtering power and annealing treatment. The last sections of this chapter covers the investigation and discussion on the formation of AZO films.

4.1 Effect of oxygen

Properties of AZO thin films depend on the sputtering condition, especially on the oxygen flow rate. The oxygen atom reacting with AZO atoms in the chamber has significant influence on the structure of AZO thin film. Oxygen flow rate may influence the carrier concentration in AZO thin films and the transparency in the visible range (Takashi et al., 2000). Therefore, this study aims to assess the effects of oxygen flow rates on the optical transmission and electrical properties of the AZO thin films. In this task, AZO thin film were fabricated by pulsed DC magnetron sputtering on Si and glass slide substrates with different oxygen flow rates from 0 to 40 sccm. The samples were investigated by FE-SEM, spectrophotometer and 4-point probe measurements. The flow rate of argon (Ar) was used as a sputtering gas and kept constant at 80 sccm, which was controlled by a mass flow controller (MKS). The deposition was carried out for

30 minutes at operating pressure of 4.2×10^{-3} mbar with varying oxygen flow rate from 0 to 40 sccm. The physical morphologies were observed by FE-SEM. The electrical properties of the AZO thin films were examined using a 4-point probe measurement system at room temperature. Lastly, the optical characteristics of the AZO thin films were further analyzed from optical transmission spectra as measured by UV-VIS-NIR spectrophotometry.

The SEM cross-section images of AZO films are shown in Figures 4.1(a)-(e). While the corresponding planar SEM images are shown in figures 4.1(f)-(j). The grain size as observed from the planar images decreases with increasing the oxygen flow rate. The thickness of thin films decreases from 309.9 nm to 193.8 nm with the oxygen flow rate increases from 0 to 40 sccm. Because the numbers of oxygen atom have an effect on decrease argon ions to bombard the target. Thus, the deposition rate was decreased with increasing oxygen flow rate (Figures 4.2).

Figure 4.2 shows the relationship between deposition rate and resistivity as a function of oxygen flow rate, varying from 0 sccm to 40 sccm. The deposition rate of AZO thin film at oxygen flow rate 0 sccm is 10.33 nm/min then dropped slightly to 6.46 nm/min at oxygen flow rate 40 sccm. These results were due to the operating pressure increase when the oxygen flow rate increase. The increase numbers of atom oxygen have affected to decrease energy per atom and mean free path of the target atom. Thus, the deposition rate of AZO thin film was decreased.
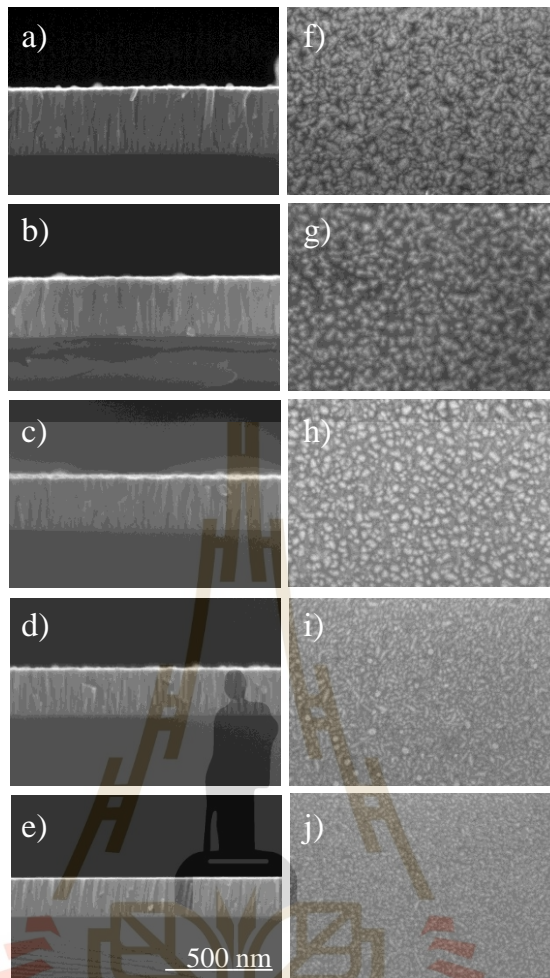
Figure 4.1 FE-SEM cross-section and planar images of AZO thin films deposited on Si substrates with oxygen flow rates of (a, f) 0 sccm, (b, g) 5 sccm, (c, h) 10 sccm, (d, i) 20 sccm and (e, j) 40 sccm.

The sheet resistance of AZO film prepared at oxygen flow rate of 0 sccm was about 90 $\Omega/\square$, which much less than that prepared at oxygen flow rate of 10 sccm (1,420 $\Omega/\square$.) After that, the sheet resistance of the oxygen flow rate more than 10 sccm was out of range for measurement with the 4-point probe. This increase of the resistance may be related to the variation of oxygen vacancies and a possibility of incorporation of oxygen atoms into the growing AZO thin films.
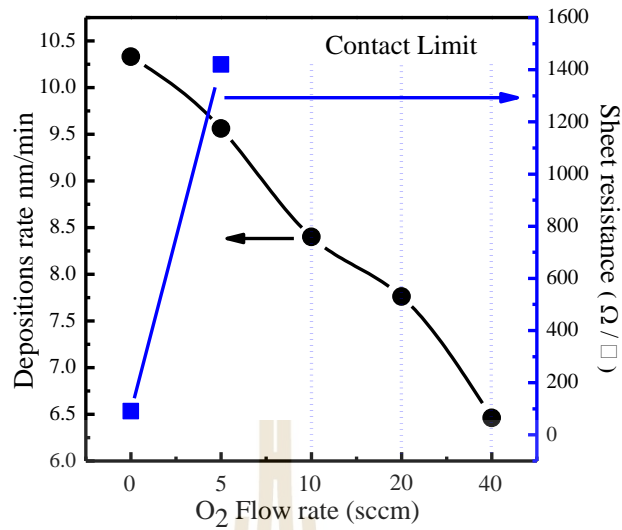
Figure 4.2 Effect of oxygen flow rate on deposition rate and sheet resistance of AZO thin films.

Figure 4.3(a) shows the optical transmittance of AZO thin films grown on glass substrates measured with light with wavelength from 200 nm to 2,000 nm. Five AZO samples prepared at five different oxygen flow rates (0-40 sccm) were studied. The transmittance oscillates in the visible region for all samples. These oscillations correspond to the constructive and destructive interference between multiple bounce beams. In the infrared region, the transmittance of AZO thin film at an oxygen flow rate at 0.00 sccm drops quicker than other samples. In this sample, there might be a strong interaction between free electrons and the incident radiation since there is a high number of free electrons in the film, which can be related to the electrical properties. The data of transmittance in the visible region were calculated for luminous transmittance and shown in figure 4.3(b).
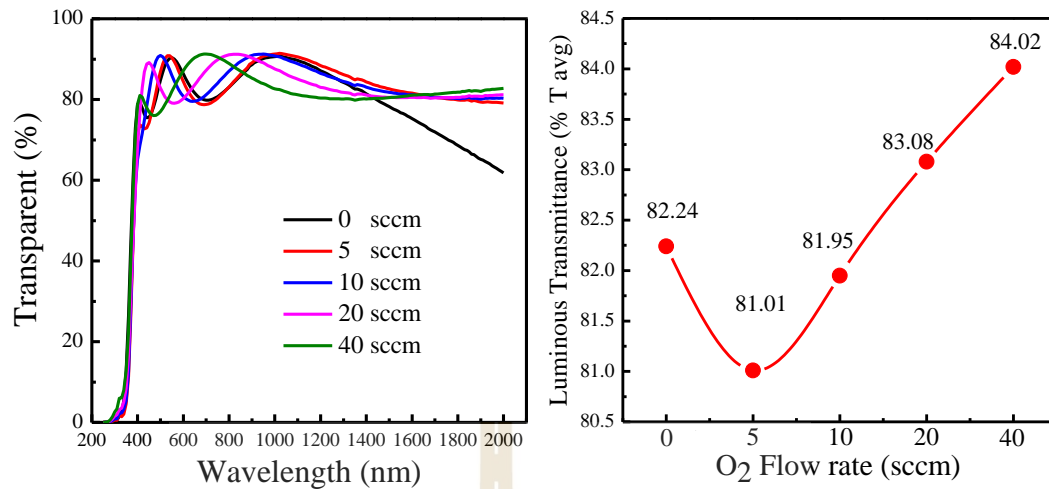
Figure 4.3 The optical properties of AZO thin films at different oxygen flow rates:
(a) transmittance spectra, and (b) average transmittance.

The AZO thin films fabricated with different oxygen flow rates exhibit differnt electrical and optical properties. The increase in oxygen improves optical properties, while deteriorates the electrical conductivity. The AZO thin film fabricated with an oxygen flow rate at 0 sccm was high conductivity and a moderate range of transmittance. Thus, it was selected as an optimum condition to prepare AZO thin film with adjusting other parameters in next steps.

4.2 Influence of deposition angle

Films of nano-texture, nano-rod and nanowire are the main interest as there is an advantage in anti-reflection property which produces a gradient-refractive index profile between material and air interface. Magnetron sputtering with glancing angle deposition (GLAD) is a technique widely used for preparation of nanostructured metal and metal oxide. It employs an oblique angle deposition (OAD) and a substrate rotation to fabricate nanostructured thin-film materials with controllable porosity and shape based on self-shadowing effect and surface diffusion during the deposition process (Horprathum M. et al., 2013, 2014). The GLAD technique can create the nanostructure by proper selection of substrate temperature, substrate rotation speed and deposition angle. However, the investigation of the nanostructured AZO fabricated from GLAD has been only few reports (Hernández M. A. et al., 2011). In this work, AZO thin films were fabricated by pulsed dc magnetron sputtering with GLAD technique. In order to control the morphologies, the film crystallinity, the optical properties, and electrical property, the deposition angle for depositing AZO films was systematically investigated.

The AZO thin films were deposited on Si (100) and glass substrates by pulsed DC magnetron sputtering with GLAD technique and with different deposition angles varied from 45° to 85°. The deposition angle is angle between measured from the substrate normal. All samples were deposited with a substrate rotation speed of 10 revolutions per minute (rpm). The deposition chamber was evacuated to a base pressure of 5×10^{-6} mbar. The working gas argon flow was fixed at 4.2×10^{-3} mbar during deposition. The pulsed DC magnetron sputtering of the AZO thin films was carried out at 100 W with a constant pulsed DC power. The AZO thin films thickness of all samples

was controlled to be about 320 nm for comparisons. This thickness is typically used for transparent electrode devices. The crystal structures of the AZO thin films were investigated with XRD, the scattered intensity being scanned in the 30-70° (2θ) range. The physical morphologies of the sample were observed by FE-SEM. The optical transmission was measured by a UV-Vis-NIR spectrophotometer. The angle of incident light beam at a normal angle on the samples for direct transmission measurements in the wavelength range from 200 nm to 2,000 nm. The electrical properties of AZO thin films on glass substrates were characterized using the van der Pauw method by hall-effect measurements at room temperature.

Figures 4.4 shows the planar and cross-section FE-SEM images of AZO thin films. The surface morphology shows that the spaces between grains exhibiting a gradual change with increasing the deposition angle. The cross-section images indicate that the structure changes from the closed pack columnar and dense structure to the vertical columnar structure when increasing the deposition angles because of the shadowing effect. Figures 4.5 shows the thickness and deposition rate as a function of deposition angles. The results show that the deposition rates continuously decreased from 28.31 to 9.07 nm/min with increased deposition angle due to the incident flux accepted by the substrate decreased at high deposition angle. Thus, the AZO thin film prepared at high deposition angle can provide the self-annealing treatment because of the longer deposition time.
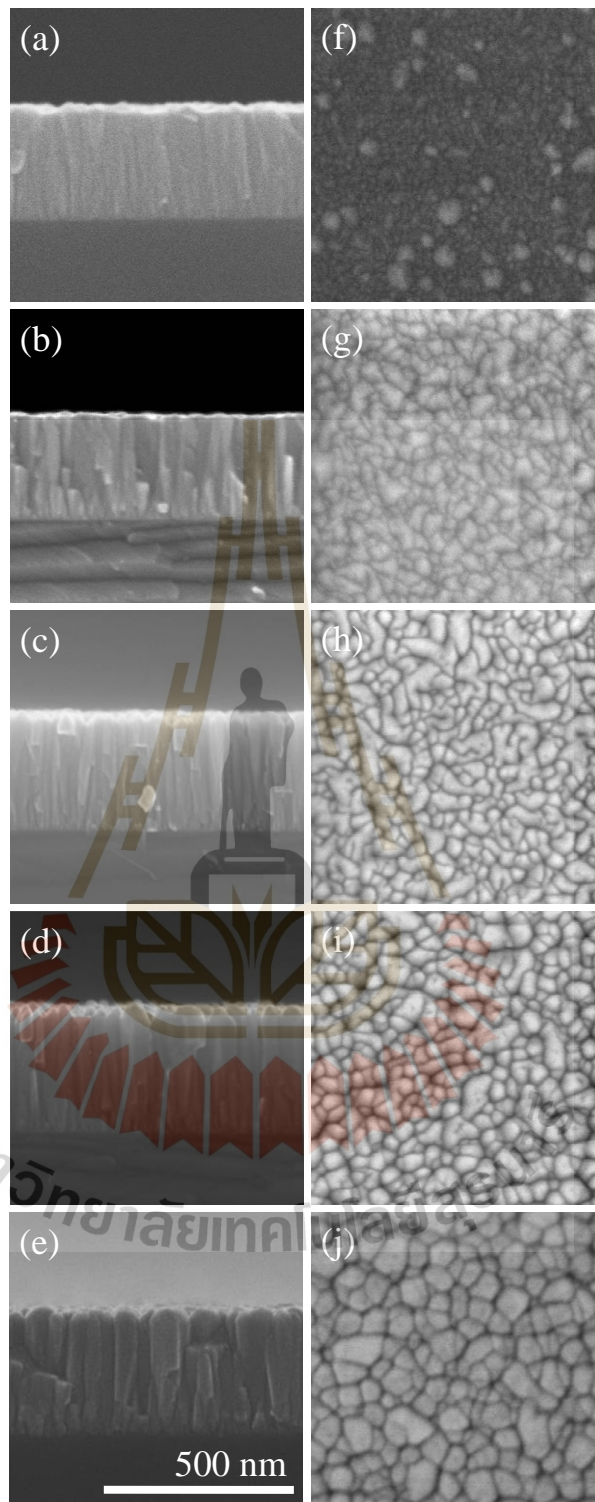
Figure 4.4 The FE-SEM cross-section and planar images FE-SEM of AZO thin films prepared with deposition angles of (a, f) 45°, (b, g) 60°, (c, h) 75°, (d, i) 80° and (e, j) 85°.
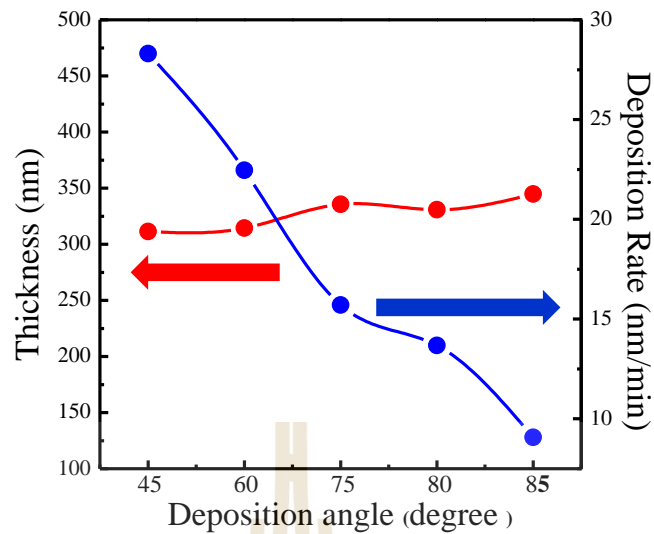
Figure 4.5 Thickness and deposition rate of AZO thin films as a function of
deposition angles.

The XRD patterns of the AZO thin films prepared with different deposition
angles are shown in figures 4.6. The AZO diffraction peaks, which were determined to
be crystalline with a hexagonal wurtzite structure associated with zinc oxide (JCPDS
no. 36-1451) (Noureddine B. H. T. et al., 2008) and its dominant orientation along the
c-axis perpendicular to the substrate surface. The results of XRD analysis show that
only two main peaks observed which could be assigned to (002) and (103) planes were
recorded in the -theta range between 30° and 70°. No diffraction peaks from Al_2O_3 were
observed, probably due to the small quantity of Al dopant. At low deposition angles,
the (002) peak is more prominent followed by the (103) peak. At high deposition angles,
the (103) peak is more prominent followed by the (002) peak, the increase in deposition
angle led to the intensity of (103) peak become higher and sharper as caused by the
self-annealing effect come from the longer deposition time would introduce the
localized heating treatment on substrate surface during film growth (Matthew et al.,
2014).
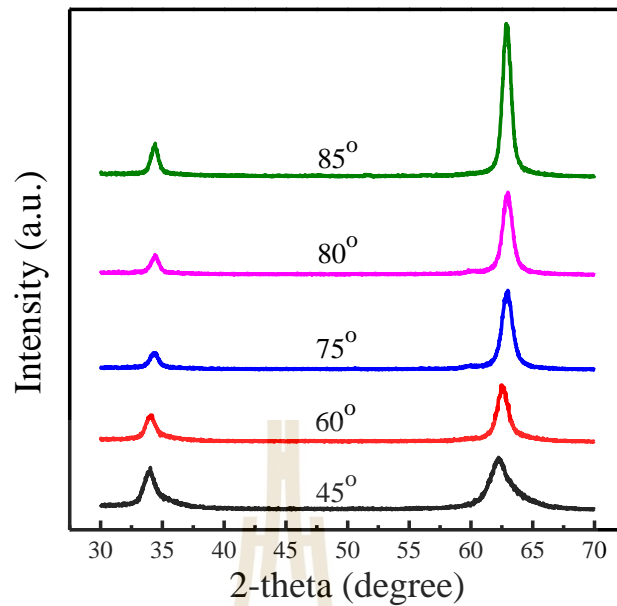
Figure 4.6 XRD patterns of the AZO thin films prepared with different deposition angles.

The UV-visible light transmittance of the AZO thin films on glass substrate are shown in Figures 4.7(a). The transmittance falls at the band edge, which is an indication of high-quality crystallinity of the films. The transmittance in the visible region shows the effects of interference, which could be due to its structure or multiple reflections at the surface of the thin films. The transmittance in IR region of the films deposited with higher deposition angles drop faster than those with lower deposition angles, which can be related to the smaller resistivity. This can be explained by the Drude theory. Figure 4.7(b) shows that the average normalized transmittance increased from 83.15% at deposition angle of 45° to 85.13% at deposition angle of 85° within the visible region of wavelengths from 380 to 780 nm. At higher deposition angles, no noticeable changes in the average transmittance were observed. The trend in the average transmittance may result from two competing factors of layer porosity and crystal quality. The AZO thin films with high crystal quality would be expected to have higher transmittance due to a

wide band gap expected for AZO. Thus, improving crystal quality with increase layer

porosity and decrease strain can enhance the transmittance of AZO thin films.
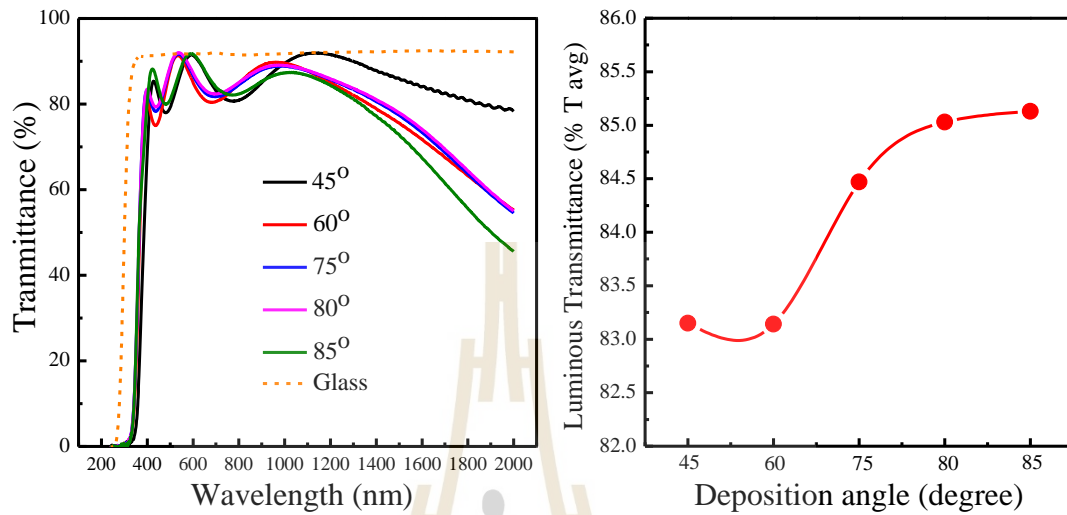
Figure 4.7 (a) UV-visible light transmittance and (b) luminous transmittance of the AZO thin films prepared with various deposition angles.

Resistivity, carrier concentration and mobility of AZO thin films were improved with the increase of the deposition angles as show in Figures 4.8. The resistivity increased as the deposition angle increased from $60°$ to $80°$ and resistivity decreased as increased the deposition angles at $85°$. The low resistivity at $85°$ deposition angles can be attributed to the vertical columnar structure surface of AZO thin films and increase grain boundary scattering. The carrier concentration and mobility show similar trends, their values increase with the deposition angles.
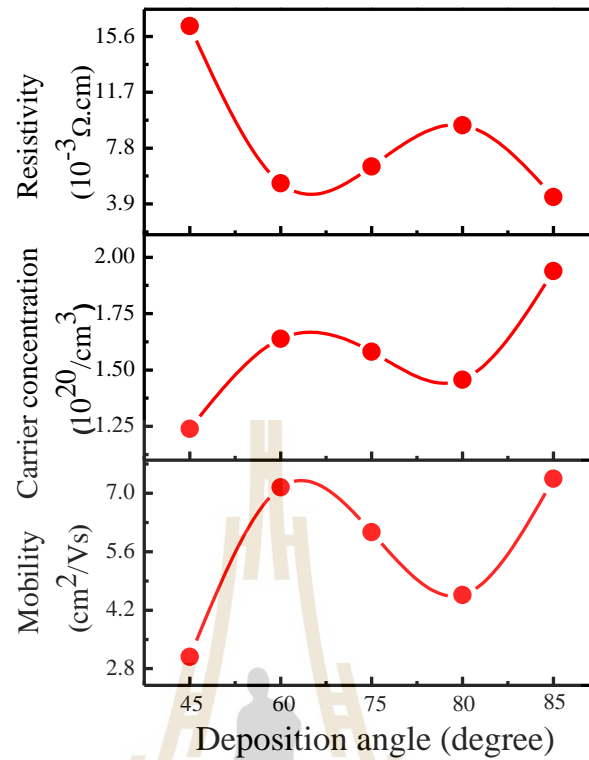
Figure 4.8 Resistivity, carrier concentration and mobility of AZO thin films
obtained from hall-effect measurements.

The AZO thin films were deposited by a pulsed DC magnetron with GLAD
technique on Si and glass substrates at different deposition angles. The influence of
deposition angle on the morphologies, optical properties and electrical properties were
investigated. It was found that the deposition rate was opposite to the deposition angle
as the results from shadowing effect. The increase in the deposition angle caused the
increased in the film grain diameter and film crystallinity due to the self-annealing
treatment on the film surface. The transmission of the prepared AZO thin film samples
was into a range of 84 - 86%. The variation of electrical property was reflected by the
film morphology and crystallinity. The present study provides a method to
enhancement of the TCO property due to the controlled of films morphology and
crystallinity by GLAD technique.

4.3 Influence of argon flow rate

In this section, fabrication and characterization of nanostructured AZO films prepared by pulsed dc magnetron sputtering with GLAD technique with variation of argon flow rates are reported. It is well-known that argon gas flow rate is one of crucial sputtering parameters contributing to the bombardment effect on the target which governs the film deposition rate (Seung and Hong, 2016).

Deposition of AZO films was carried out with high pure argon (99.999%) supplied through mass-flow controller at different flow rates, between 40 and 120 sccm. Before sputtering, the deposition chamber was evacuated by a combination of a turbomolecular pump and a rotary pump to achieve a base pressure of 5×10^{-6} mbar. The pressure during deposition was 5.2×10^{-3} mbar. The dc sputtering power was kept at 100 watts. The sputtering deposition was positioned at a deposition angle of 85° with the respect to the vapor incident flux. The distance between the substrate holder to the target and the substrate rotation speed were 28 cm and 10 rpm, respectively. The thickness of the nanostructured films was controlled to be 400 nm.

The physical morphologies of the prepared nanostructured AZO film were obtained from the FE-SEM images as shown in Figure 4.9. From the planar FE-SEM images (Figures 4.9(f)-(j)), the increase in argon flow rate led to more dense structure. The average grain size of the nanostructured AZO film was 56.14 nm. The cross-sectional FE-SEM images (Figures 4.9(a)-(e)) revealed the nanostructured AZO films with columnar structures arising from the enhanced shadowing effects when the directed vapor flux incident on substrate at a glancing angle. It should be noted that the nanocolumns are partially connected along part of their wall. By increasing the argon flow rate, the wall connection occurs continually throughout the nanocolumnar AZO

layer. The deposition rate of the nanocolumnar AZO film prepared as a function of argon flow rate is shown in Figure 4.10. The deposition rate is more or less a linear function of argon flow rate. This may be attributed to a higher number of sputtered atoms at high argon flow rate resulting in that the number density of argon ion bombardment was much higher than the ZnO re-evaporation effect.
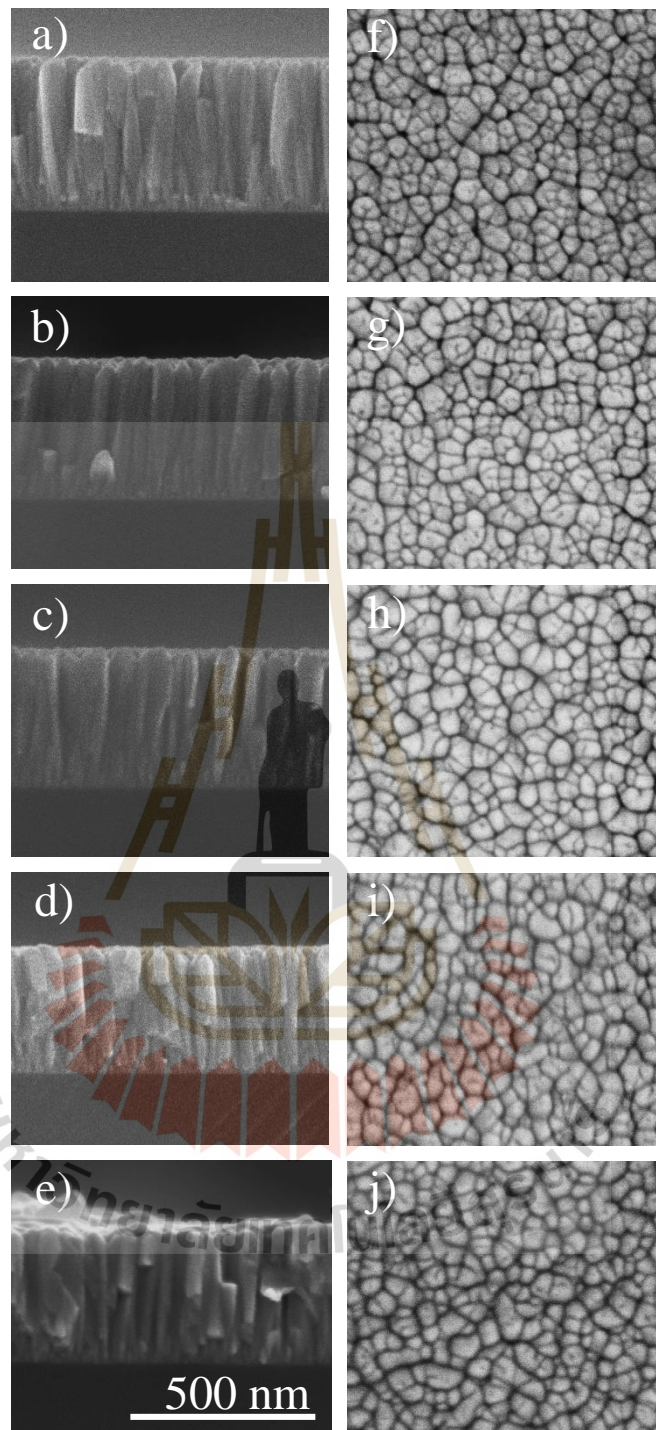
Figure 4.9 Cross-section and planar FE-SEM images of AZO thin films deposition on Si substrate at Ar gas flow rates of (a), (f) 40 sccm, (b), (g) 60 sccm, (c), (h) 80 sccm, (d), (i) 100 sccm and (e), (j) 120 sccm.

The GIXRD measurements were carried out on the nanocolumnar AZO films prepared at different argon flow rates (Figures 4.11). The GIXRD patterns indicate that all the prepared films show the hexagonal wurtzite structure. The obtained diffraction peaks correspond to the (002) and (103) planes (JCPDS on 36-1451).
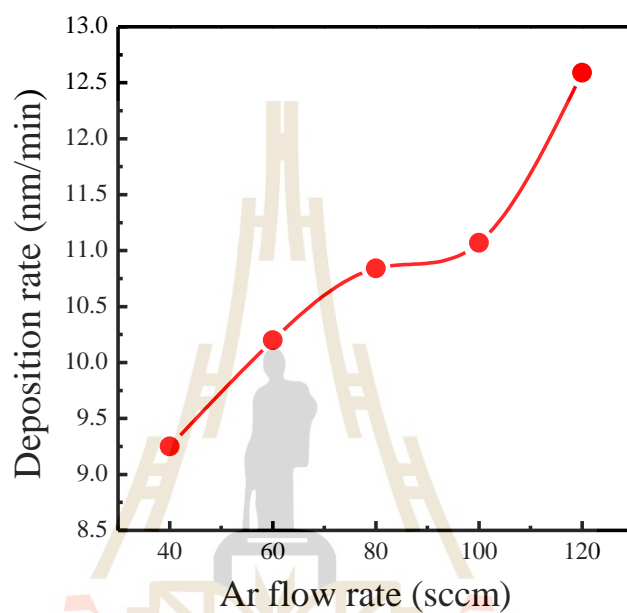
Figure 4.10 Deposition rate of AZO thin films as a function of Ar gas flow rate.
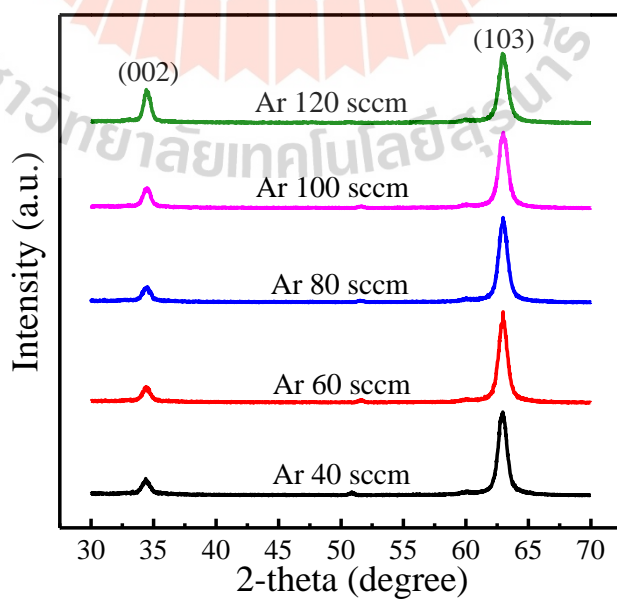
Figure 4.11 XRD patterns of AZO thin films.

Figures 4.12(a) shows the transmission spectra of the nanocolumnar AZO films deposited at different argon flow rates. It was observed that all transmission spectra of the prepared samples have strong absorption in the UV-region between 320 and 380 nm. This is due to the fact that AZO is a wide band gap semiconductor with an energy gap of 3.4 eV (364 nm). Moreover, the transmission spectra in the infrared region was relatively low because of a high reflectance caused by the free electrons (Robert, 2010). The average transmission values of the prepared films in the visible range (380-780 nm) were about 85%, as shown in Figure 4.12(b). The results indicated that the argon flow rate does not have a significantly effect on the transparency of the nanocolumnar films over the visible region range. In addition, all of these transmission values include the absorption and reflectance by the glass slide substrate as well. If the effects from the glass slide substrate were excluded, the transmission of the nanocloumnar films themselves was found to be higher than 90% in the visible region.
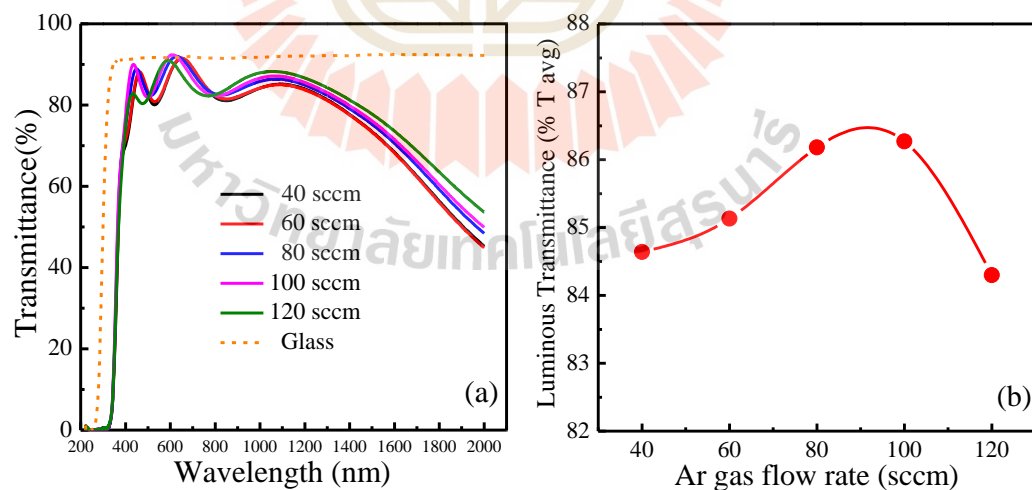
Figure 4.12 (a) UV-visible light transmittance and (b) average transmittance of the AZO thin films prepared with various Ar gas flow rates.

Figures 4.13 shows the variations of the resistivity of the nanocolumnar AZO films deposited at different argon flow rates obtained from Hall-effect measurements. At low argon flow rate, the resistivity decreases when increasing flow rate mainly due to the increase in the packing of the nanocolumnar AZO structures leading to the enhanced surface recombination. The work function of the nanocolumnar AZO films obtained from UPS measurements is shown in Figure 4.14. The work function is about 4.0 eV at low flow rate, and slightly increases with the argon flow rate. This value of work function slightly lower than that of AZO films commonly cited, which is 4.4 eV (Kumar et al., 2016).
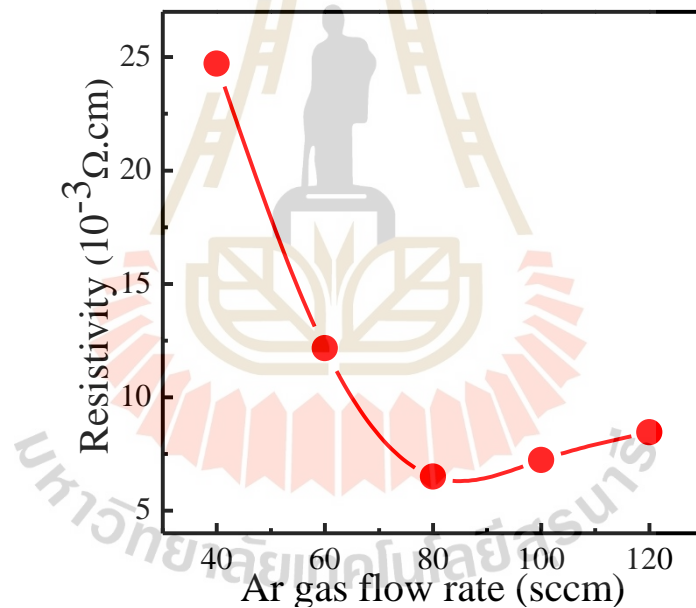
Figure 4.13 Resistivity of the AZO films obtained from hall-effect measurements.
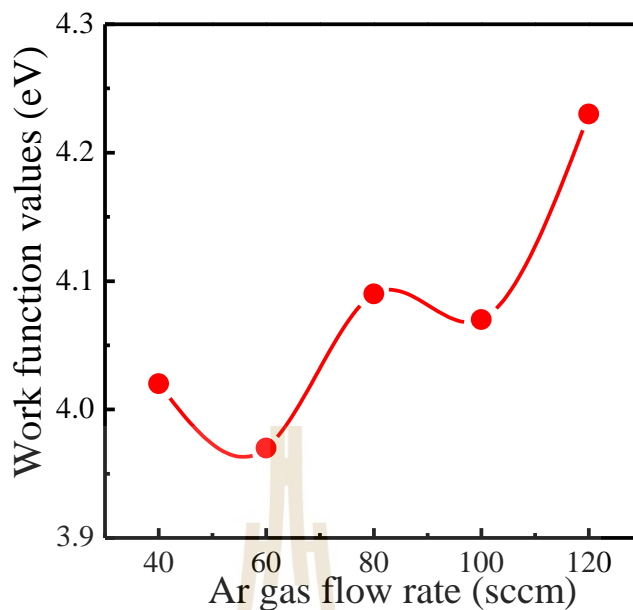
Figure 4.14 The work function of the AZO films taken from UPS spectra.

Figures 4.15(a)-(d) show, respectively, a wide scan, Zn3d, O2s and Al2p XPS spectra taken from the nanocolumnar AZO films deposited at different argon flow rates. The wide scan spectra show expected elements of the materials and typical carbon and oxygen contaminants on the surface of the films. These contaminants are the result from the exposure of the samples to ambient air. Figure 4.15(b) shows the spectral peaks corresponding to the Zn3d electron bounded to the O2p electron. The O1s peak at 531.8 eV is assigned to the O^{2-} ions on the wurtzite structure of hexagonal Zn^{2+} ions. The Al2p peak at binding energy of 73.2 eV is attributed to the Al bonds, which value lies between binding energy of metallic Al and Al_2O_3 at 72.7 and 74.8 eV, respectively.
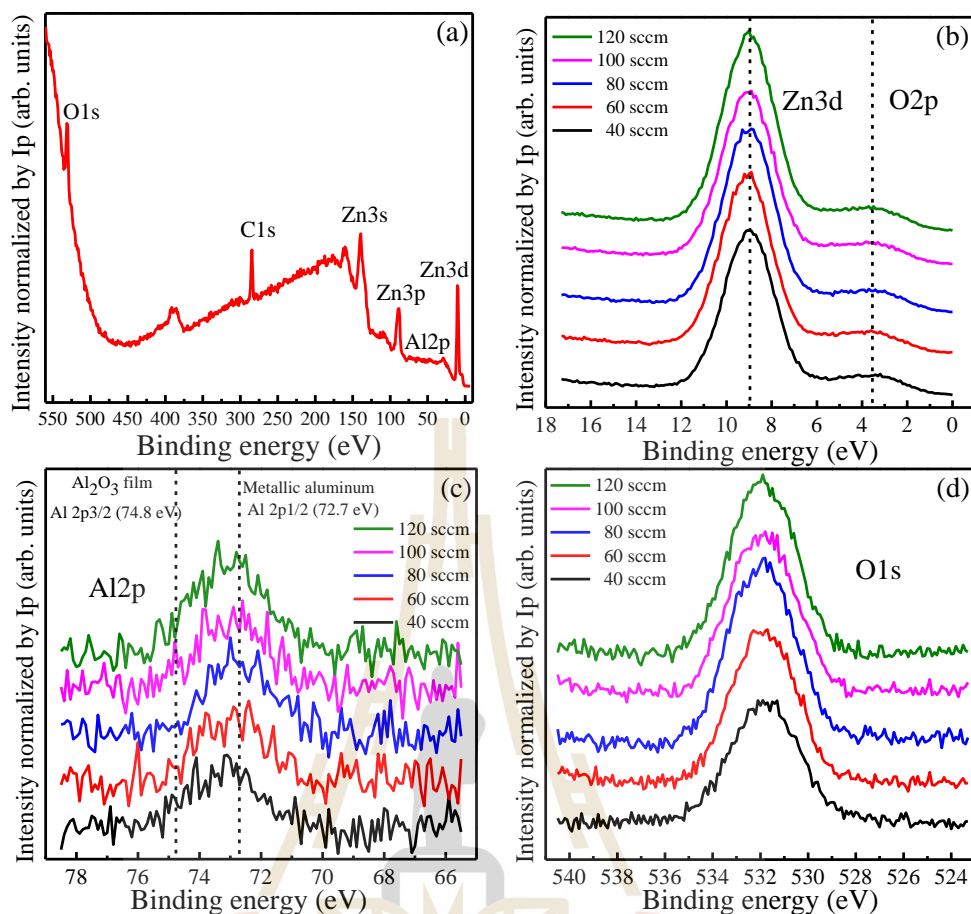
Figure 4.15 (a) A wide-scan, (b) Zn3d, (c) Al2p and (d) O1s XPS spectra of AZO prepared with various Ar gas flow rates.

In summary, the nanocolumnar AZO films were successfully fabricated by pulsed dc magnetron sputtering with GLAD technique. The deposition rate and film packing were simultaneously increased as the argon flow rate increases. The average transmission of nanocolmnar films was found to be higher than 80% over the visible range. The electrical resistivity of the nanocolumnar films exhibits low resistivity (6.51×10^{-3} $\Omega \cdot$cm). These results show that the nanocolumnar AZO films deposited by GLAD is a promising TCO material for solar cell and optoelectronic devices.

4.4 Influence of sputtering power

In this chapter, the nanocolumnar AZO film prepared at different sputtering powers were characterized by x-ray diffractrometry, field emission scanning electron microscope, UV-Vis-NIR spectrophometry with angle dependence technique and hall measurement. XRD measurements revealed that the films were the nanocolumnar structure. The average transmisstance in visible region of the nanocolumnar AZO films ranged from 82% to 87%. In addition, the effect of the sputtering power on the film crystalline, morphological, optical and electrical properties of the nanocolumnar AZO film has been investigated.

The nanocolumnar AZO films were deposited by pulsed DC magnetron sputtering with GLAD technique on glass and silicon (100) substrate. The incident deposition flux angle with respect to the surface normal and the substrate was fixed at 85° with 10 rpm-substrate rotation speed. The deposition chamber was evacuated by a rotary pump and turbo-molecular pump to a based pressure 4.5×10^{-6} mbar. The flow rate of argon (Ar) was used as a sputtering gas and keeps constant at 80 sccm, which was controlled by mass flow controller (MKS). The deposition was carried out for 30 minutes at operated pressure of 4.2×10^{-3} mbar. The DC power were varied from 25 to 150 W. Note that before each sputtering deposition experiment, a 3 inch AZO target was pre-sputtered in the argon plasma for 3 minute in order to remove an excessive oxide surface layer and contamination. The crystalline structure, morphology, optical and electrical properties of nanocolumnar AZO film prepared at different sputtering powers were characterized by x-ray diffractrometry, field emission scanning electron microscope, UV-Vis-NIR spectrophometry with angle dependence technique and hall measurement, respectively.

The XRD pattern of the nanocolumnar AZO film prepared at different sputtering power on Si substrate were shown in Figure 4.16. The XRD pattern exhibits a 2θ peak at 34.41° and 62.86° corresponding to the (002) and (103) respectively. The results indicated that all prepared films show a crystal structure with a hexagonal wurtzite structure associated with ZnO peaks (JCPDS no. 36-1451). The growth has preferred direction along the c-axis perpendicular to the substrate surface. It can be found that the intensity of (002) peak of the AZO films increases with increasing the DC sputtering power up to 50 W and then obviously decreases with further increase of the sputtering power. Note that further increase in the DC power, the intensity of the diffraction peak of (103) increases gradually. The increase in sputtering power was expected to promote highly crystalline due to high energy was available for stimulating ejected atoms form the target with high kinetic energy (Chan and Teo, 2006, 2007). Moreover, the Al_2O_3 were not detected in the XRD pattern due to the small quantity of Al dopant and implies that Al atoms were substituted in the hexagonal lattice of ZnO or segregated to the non-crystalline region in grain boundary (Kar et al., 2010).
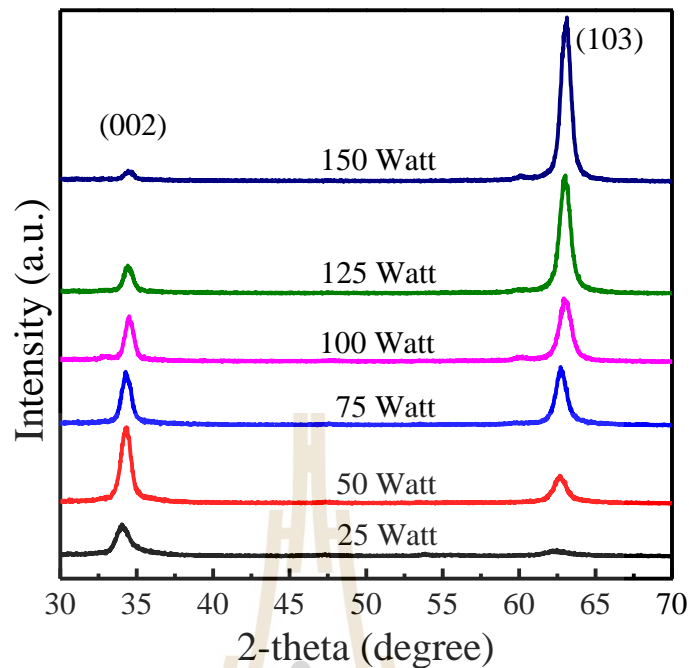
Figure 4.16 X-ray diffraction patterns of nanocolumnar AZO films at different DC sputtering powers.

The cross-section and surface morphology of the nanocolumnar AZO films are shown in Figure 4.17. The cross-sectional morphology of the nanocolumnar AZO film was present in Figures 4.17(d)-(f). From Figures 4.17(g)-(l) shows that the grain size increases with increasing the DC sputtering power. The obtained films were composed of the columnar structure caused by the self-shadowing effect and surface diffusion during the film grown by GLAD technique. The results indicate that the thickness of nanocolumnar AZO film increase with increasing DC sputtering power. The overall phenomenon allowed the improvement of kinetic energy of atom, which make grains size become larger and high deposition rate.
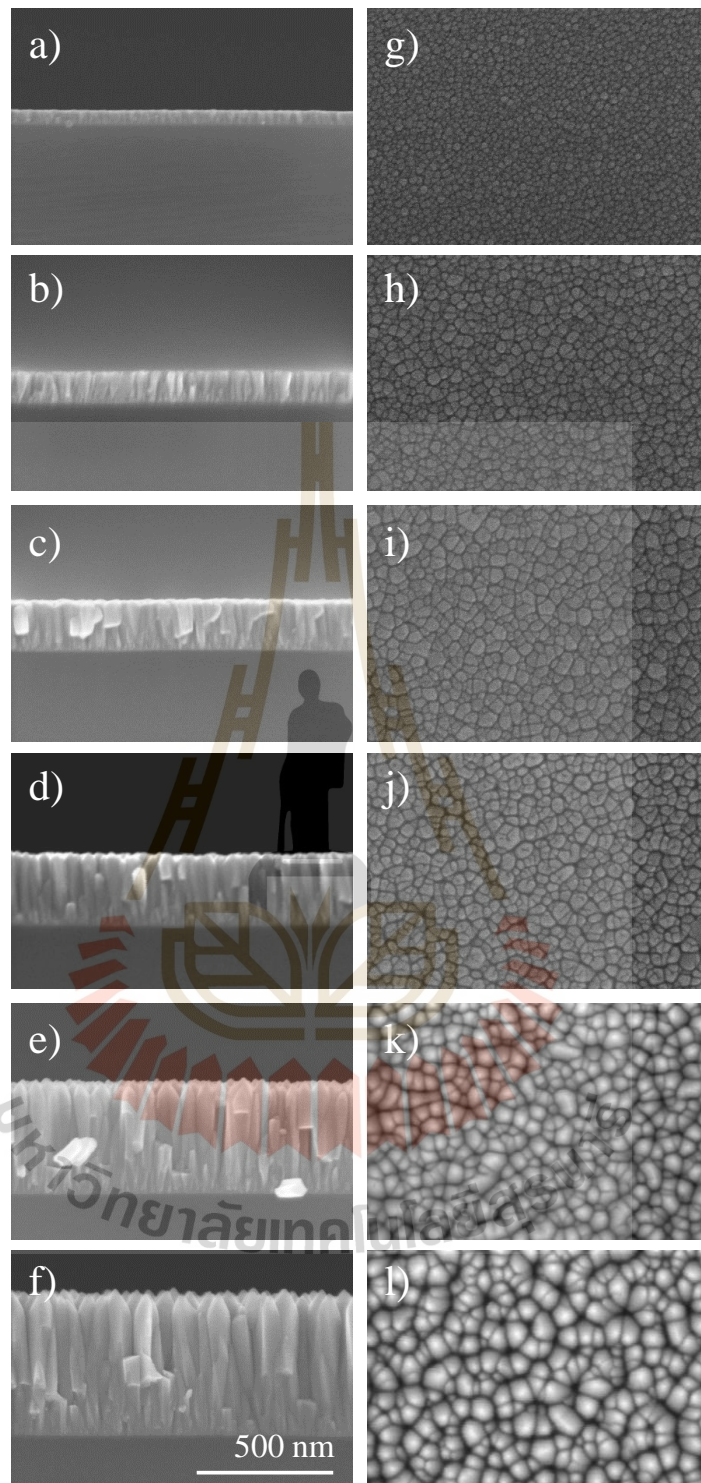
Figure 4.17 FE-SEM cross-section and planar images of nanocolumnar AZO films deposited on Si substrate using the power of (a, g) 25 W, (b, h) 50 W, (c, i) 75 W, (d, j) 100 W, (e, k) 125 W and (f, l) 150 W.

Figures 4.18(a) and (b) show the transmittance spectra of nanocolumnar AZO films and the luminous transmittance over the visible wavelength region, respectively. All obtained films possess high transmittance and exhibit an apparent absorption edge at about 1,200-2,000 nm. The transmittance spectra exhibit interference fringes pattern in the visible region for sample prepared at 50 to 150 W. The decreasing transmittance spectra in NIR and IR region with increasing DC sputtering power was mainly attributed to the film high crystalline and low resistivity (Rueben et al., 2012; Qianqian et al., 2016). The calculated luminous transmittance increased slightly from 82.31% to 85.70% with increasing the DC sputtering power from 25 to 75 W. It is obvious that the nanocolumnar AZO films prepared with 125 W (~87.3%) have the highest average transmittance in the visible light region.
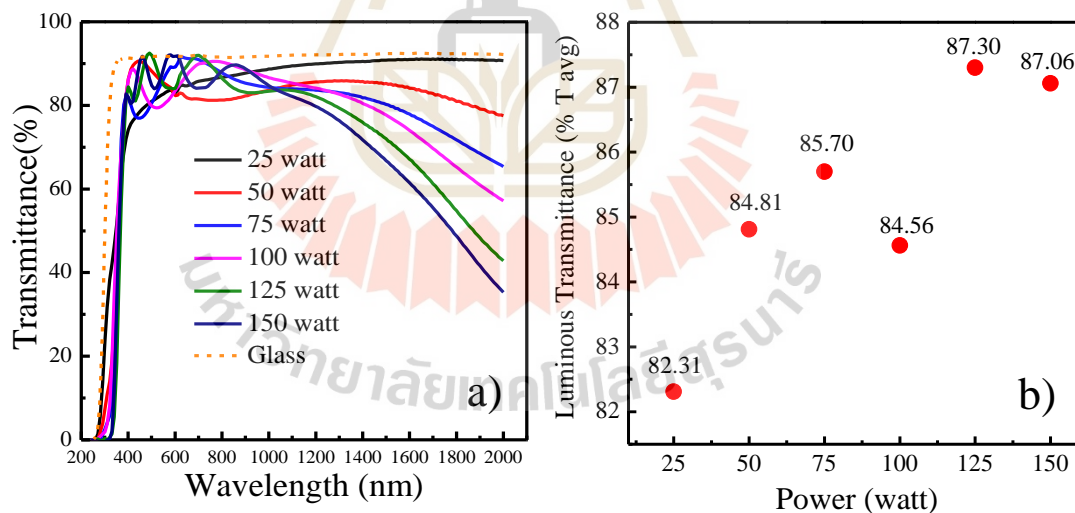
Figure 4.18 (a) Optical transmittances curves and (b) luminous transmittance of nanocolumnar AZO films on glass substrate.

Figure 4.19 illustrates of the omnidirectional characteristic of the nanocolumnar AZO films at 550 nm. The measurements were carried out over a range of angle of incident from -80° to 80° with 10° increment. The results clearly show that all prepared

samples had lower optical transmission than the glass slide substrate reference at all incident angle. The results revealed the performance of the prepared nanocolumnar AZO film as a sensitivity to the angle of incidence. The AZO nanocolumnar deposited at 125 W exhibited good omnidirectional antireflection characteristic at all angles of incidence.
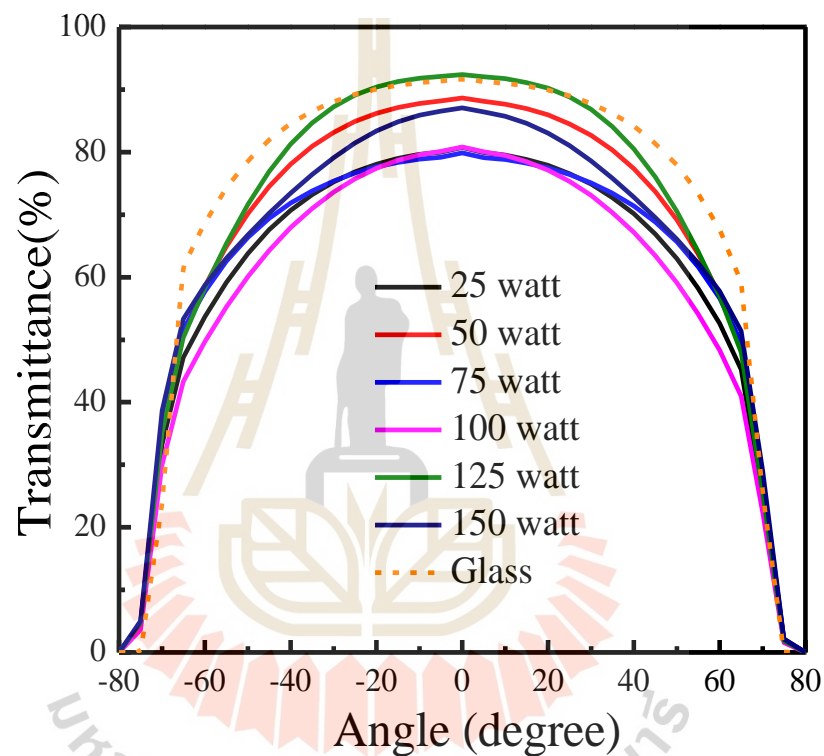
Figure 4.19 Angle-dependent optical transmittance spectra of nanocolumnar AZO films.

As shown in Figure 4.20, the electrical property of the prepared nanocolumnar AZO films on glass substrates were characterized by Hall-effect measurements with the applied magnetic field of 0.55 T. The sample prepared at 25 W was very high resistance (contact limited) due to the lowest film thickness and small grain size. With increasing of DC sputtering power from 50 to 150 W, the mobility and carrier concentration tend to increase from 4.05 cm^2/Vs, 1.60×10^{20}/cm^3 to 6.17 cm^2/Vs, 2.00×10^{20}/cm^3,

respectively. In Figure 4.20, it is obvious that the AZO nanostructured films prepared with the sputtering power of 125 W have high mobility and carrier concentration value (6.32 cm^2/Vs, 2.34×10^{20}/cm^3) and lowest resistivity (4.21×10^{-3} Ω.cm).
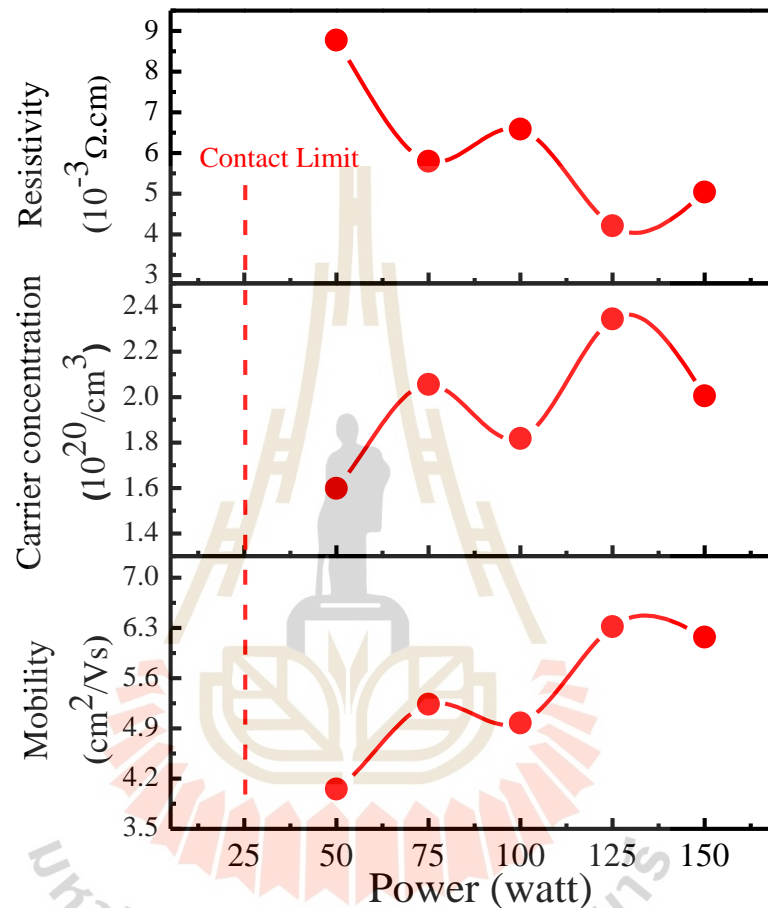
Figure 4.20 Electrical properties fromHall-effect measurements: Carrier concentration, resistivity and mobility of nanocolumnar AZO films as function of the sputtering power.

The high transparent nanocolumnar AZO film was successfully deposited on glass slide and Si substrate via pulsed DC magnetron sputtering with GLAD technique. By changing the DC sputtering power, the crystalline, morphology, optical and electrical property of the nanocolumnar AZO film were changed. Lower in DC sputtering power leads to low crystalline, small grain size while increasing DC power

the film property was enhanced due to the high improvement of kinetic energy of atom. FE-SEM studies revealed that the thickness and deposition rate increase with increasing DC sputtering power. The transparent of the nanocolumnar AZO films varied between 82.48 and 87.30% with resistivity between 8.77×10^{-3} and 4.21×10^{-3} Ω.cm. The optimized power of 125 W was chosen to prepare nanocolumnar AZO film deposited on glass substrate with high transmittance with omnidirectional characteristic. For further study reported in the next section.

4.5 Influence of substrate rotation speed.

The GLAD technique is a very promising for thin films deposition to control the structure and fabricate nanostructured films. The nanostructure of AZO thin film fabricate by GLAD technique was reported by Yildiz A. et al. (Yildiz et al., 2015). The principal of GLAD technique is based on atomic shadowing mechanism in high angle deposition geometry, leading to preferential growth of existing nuclei growth and island to self-assemble into nanostructures at the substrate surface. The substrate rotation speed, change of φ angle with respect to time, very likely affects the time for the vapour flux to be captured on the substrate surface and, thus, have an influence on the nanostructure shape (microstructural properties). The continuous rotation with high speed assists the structures to grow in the vertical direction more than lateral directions and, thus, induces the formation of a vertical nanostructure. On the other hand, the impact of continuous rotation with slow speed, the growth direction smoothly rotates in both lateral and vertical directions leading to the formation of columns shaped into helical morphology. Thus, the growth of difference both directions can affect the thin films structure such as surface roughness, grain size and the strain in the structures. Furthermore, the electrical and optical properties of the nanostructure vary due to void formation and the light-trapping mechanisms which produce a gradient-refractive index profile of the nanostructures in different shapes. Therefore, this section investigates the effects of the substrate rotation speed on the formation of AZO nanostructures and physical morphologies, crystallinity, optical, electrical characteristics and chemical composition.

4.5.1 Structure and crystalline properties

Figure 4.21 show FE-SEM cross-section and planar image of the AZO thin films were deposited on Si (100) and glass substrates by pulsed DC magnetron sputtering with the GLAD technique with sputtering power of 125 W, 85° deposition angle and different substrate rotation speeds of 0.02, 0.04, 0.08, 0.16 and 10 rotation per minute (rpm).

The structure growth into helically twisted structure could be observed by deposition with slow substrate rotation at 0.02 rpm. The structure change to helical, spiral, screw-like columnar, vertical structure are generated by substrate motion with increasing rotation speed at 0.04, 0.08, 0.16 and 10.00 rpm, respectively. Figure 4.21 shows the surface and cross section images of AZO nanostructures (Figures 4.21(a)-(e)) fabricate by GLAD technique with different substrate rotation speeds, comparing to AZO thin film (Figures 4.21(f)).
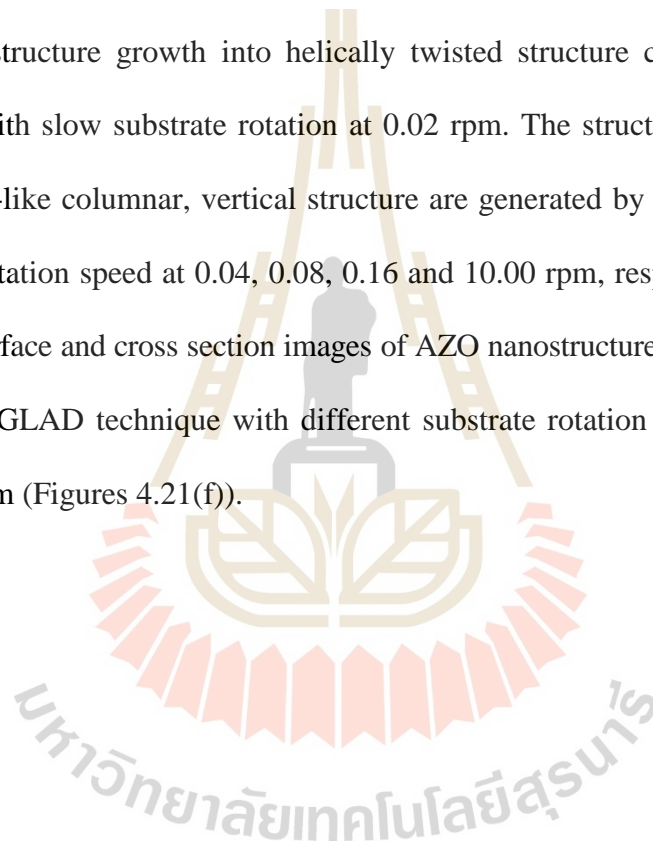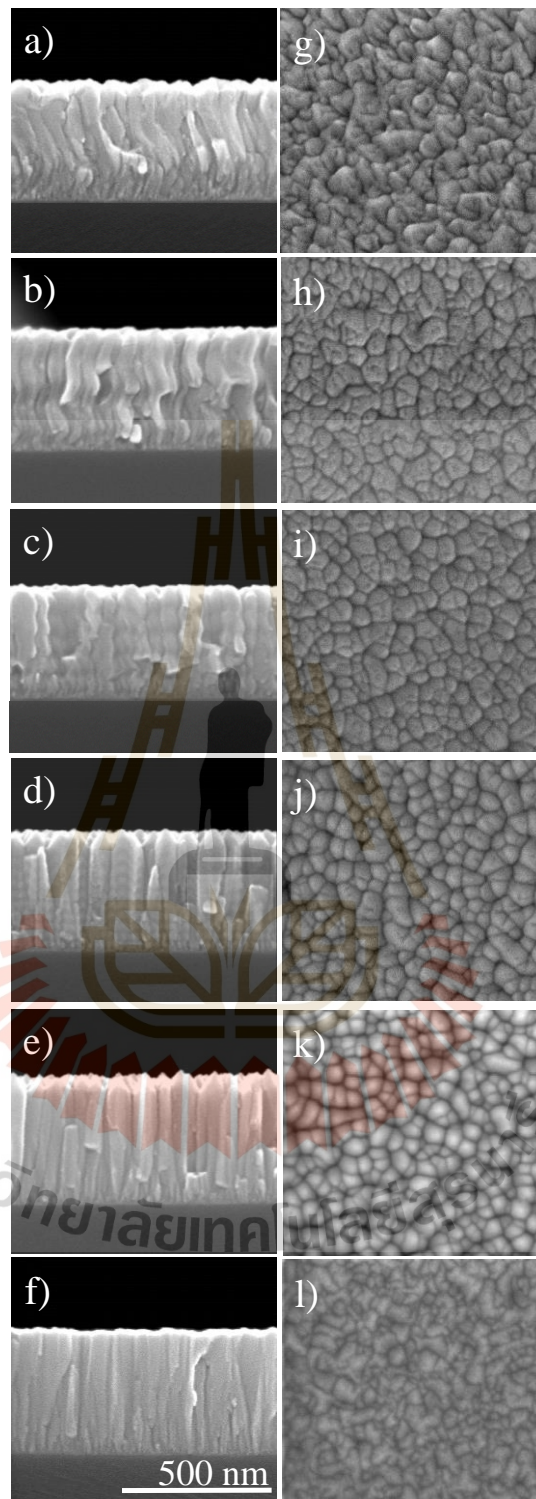
Figure 4.21 Cross-sectional and planar images of nanostructure AZO films deposition

on Si substrate at rotation speed of (a), (g) 0.02 rpm, (b), (h) 0.04 rpm, (c), (i) 0.08 rpm,

(d), (j) 0.16, (e), (k) 10.00 rpm, and (f), (l) AZO thin film at 10.00 rpm.

The substrate rotation speed defines the deposition time of vapor flux particles to be capture on the position of the top surface of the structure. The slow substrate rotation allows vapor flux particles to be captured on the structure for a long time, and after that the shape of structure turns into a helically twisted structure. On the other hand, the fast substrate rotation allows vapor flux particles to be captured on the top surface and rotating around the substrate axis in a short time. Thus, the incident vapor effectively arrives at the column apex from all sides simultaneously, resulting in a direction of structure grow into vertical columns. Therefore, the nanostructure of AZO films changes from helically twisted to vertical structure with increasing rotation speed from 0.02 rpm to 10.00 rpm.

The GLAD technique provides possibility to control the nanostructure by shadowing mechanism. Two important factors to be considered are the deposition angle of substrate and substrate rotation speed, which lead to vapor source trajectory under limited adatom mobility above the top surface of AZO structure. The effect of substrate rotation speed determines the pitch P of the helix and the helical radius of curvature (Figure 4.22). The pitch P define as the deposited film thickness per complete substrate revolution. A rapid rotation speed reduces the pitch P values and produces a more tightly wound helix with reduced structure pith and radius of curvature. The AZO films prepared with the deposited angle of 85° and different substrate rotation speeds show different nanostructures. The changes in the nanostructure may be deduced from the pitch P and the column width w ($\sim$74 nm). The AZO helical nanostructure is gradually lost as the helical pitch approaches the column width w and value P $\sim$ w regime, the distinct helical morphology transitions into a screw-like columnar microstructure, as shown in Figures 4.21(d) (P = 83 nm). When P < w, the helical structure degenerates

completely and the film morphology fully transitions into vertical structure (P = 1.3 nm) and P >> w, the film morphology transitions into helically twisted structure with the substrate rotation speed is very slow (P = 667 nm).
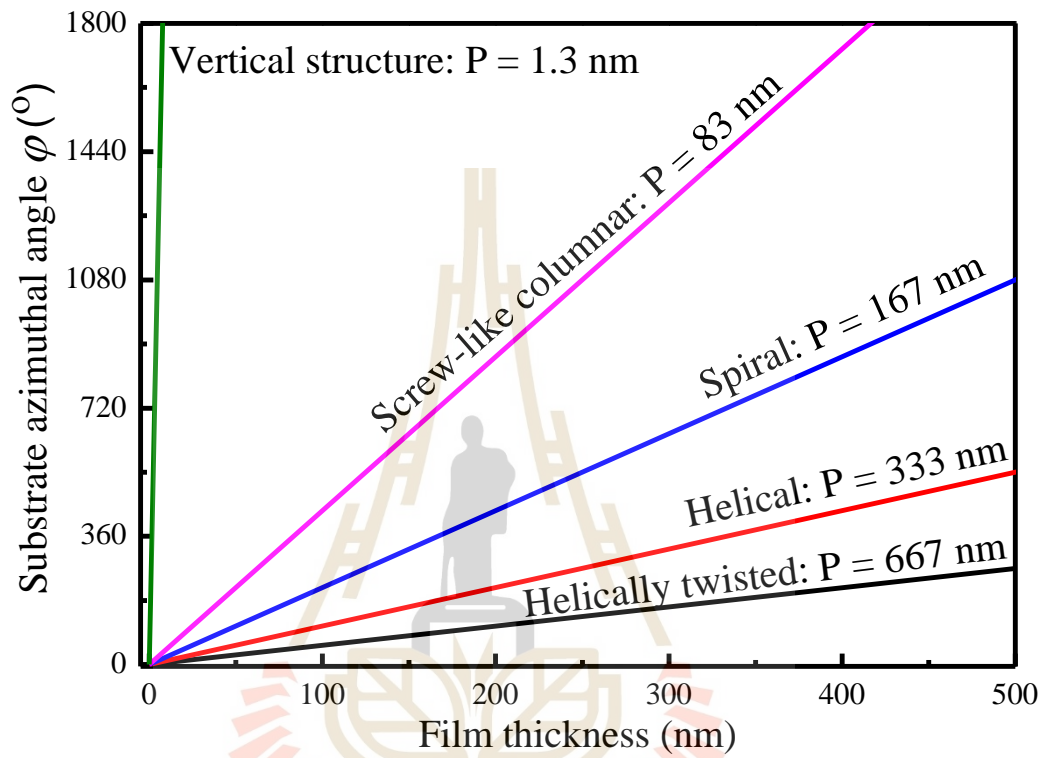
Figure 4.22 Substrate motion algorithms for continuous φ rotations at different speeds. The rotation speed is controlled by setting the pitch P, as it has a direct impact on the resulting thin film structure.
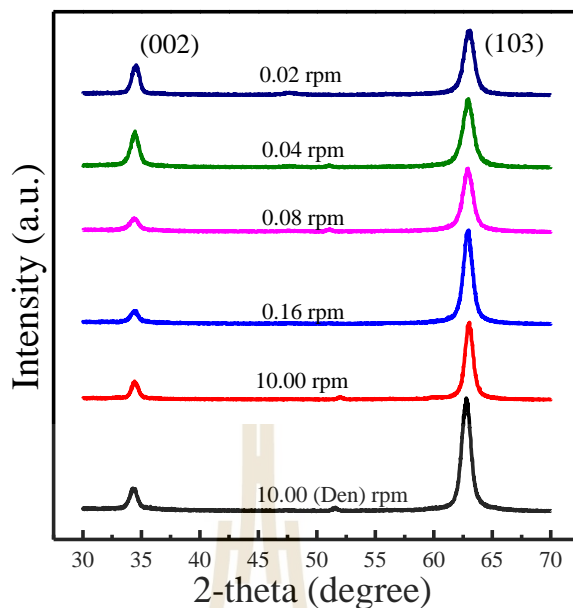
Figure 4.23 XRD patterns of the nanostructured AZO films deposited with different substrate rotation speeds.

Figure 4.23 shows XRD patterns of nanostructured AZO films deposited with different substrate rotation speeds. The AZO films are identified as crystalline with preferred orientation along (002) diffraction peak at about 34.43° and (103) diffraction peak at about 62.88°. The AZO films have a hexagonal wurtzite crystal structure of zinc oxide (JCPDS no. 36-1451).

Figure 4.24 shows the cross-section bright-field TEM images and TEM diffraction patterns of three different AZO structures; helically twisted structure (a-b), vertical structure (c-d), and thin film (e-f). The TEM samples were prepared by a focus ion beam (FEI Versa3D), and a Pt layer was deposited as a protection layer. Figure 4.24(e) shows the AZO thin film structure consisting of columns with relatively strong c-axis preferred orientation. The direction of structure grows around a central axis with rotated slowly that are put together to form a helically twisted structure. The multi-grains in Figure 4.24(c) showed a very complicated arrangement for orientations of helically

twisted shape. Figure 4.24(c) shows the structures that are grown in vertical shape in the direction normal to the substrate surface. The diameter of the vertical structure increases steadily with thickness, which may be a consequence of the adatom diffusion distance increases with the growing structure at high temperatures for extended deposition time (Vick et al., 1999; Wei et al., 1999). TEM diffraction patterns of all samples, shown in Figure 4.24 provide the interplanar spacing of crystal planes of AZO films similar to that obtained from XRD measurements.
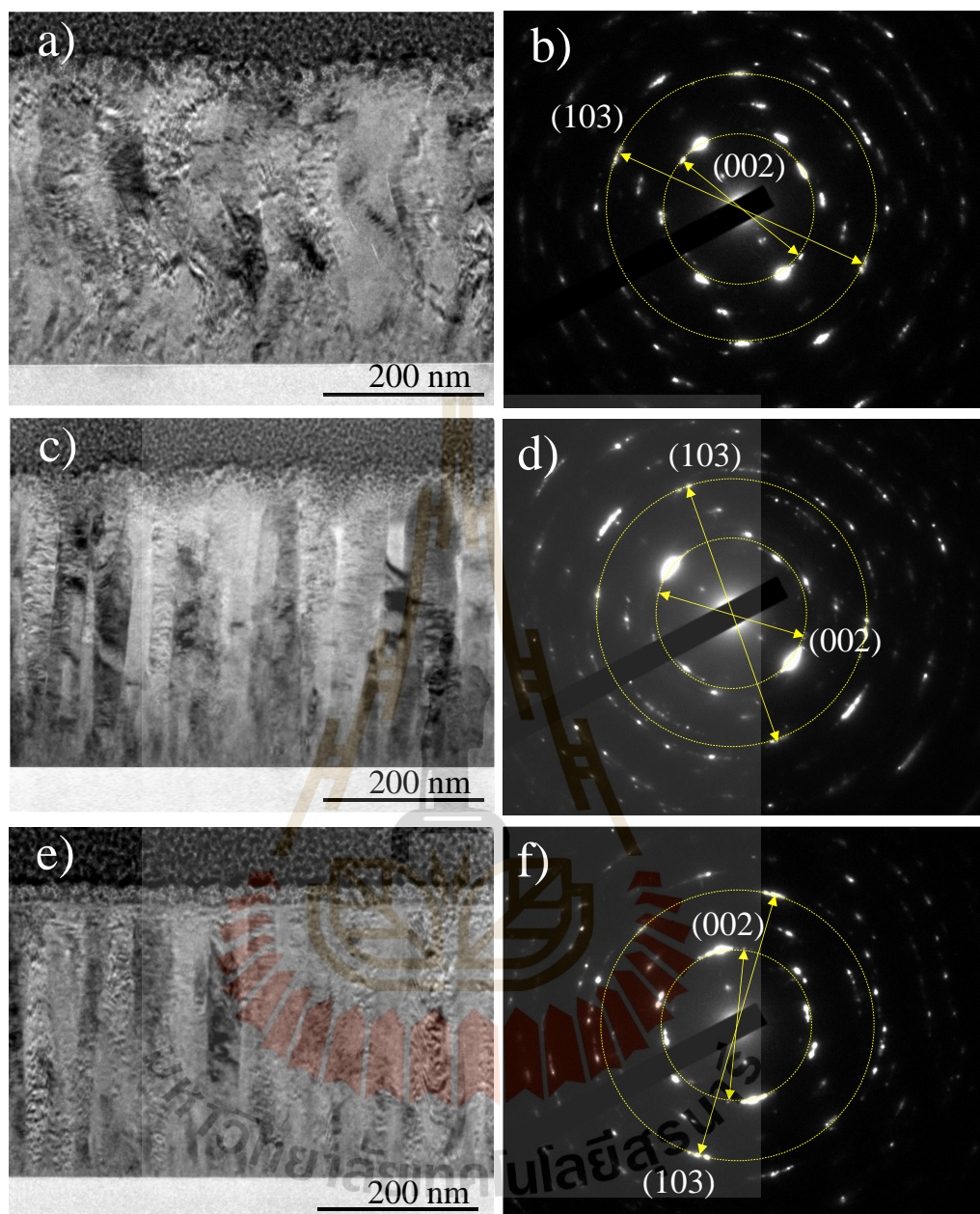
Figure 4.24 Cross-section bright-field TEM images and the selected area diffraction patterns obtained from the AZO films of (a), (b) helically twisted structure (0.02rpm), (c), (d) vertical structure (10.00 rpm), and (e), (f) thin film (10.00 rpm).

4.5.2 Chemical composition and valence band
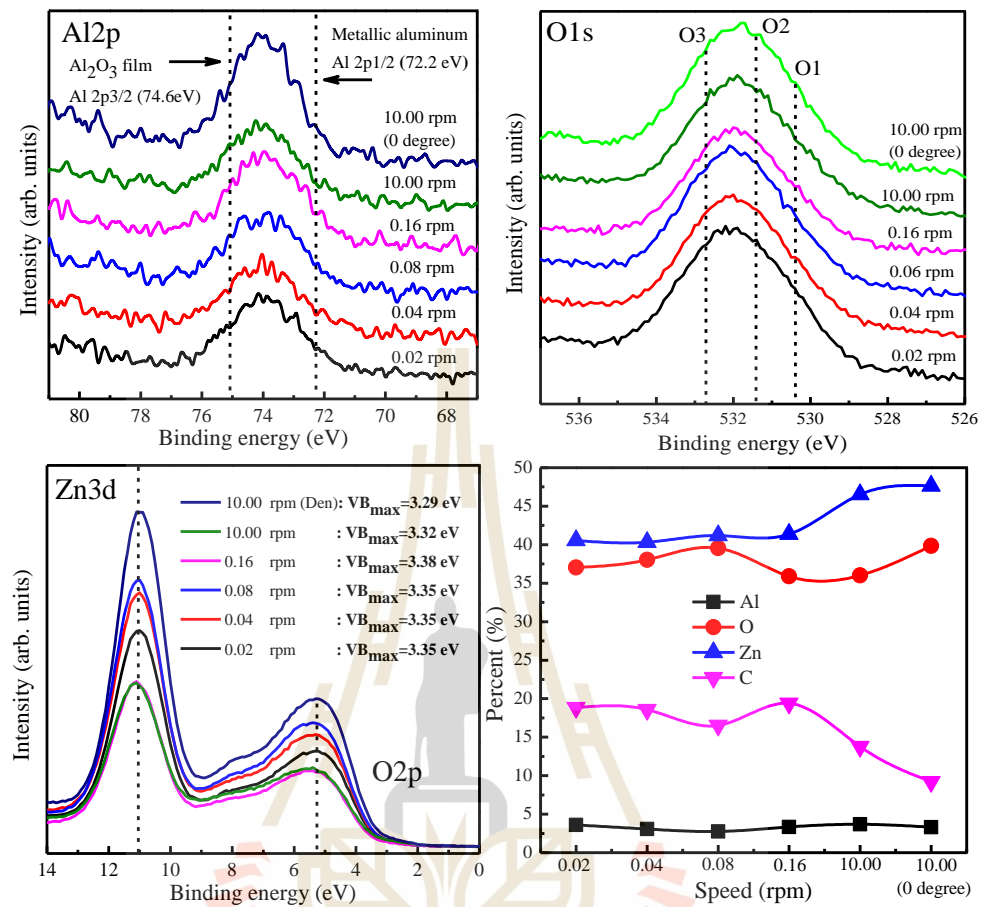
Figure 4.25 (a) Al2p, (b) O1s, (c) valence band spectra and (d) percent of chemical composition of nanostructured AZO films and dense.

Figure 4.25(a) shows the Al2p XPS spectra of taken from the AZO films deposited with difference rotation speeds. The peak profiles of all samples show no observable difference. The binding energy of Al2p for all samples is located at 74.0$\pm$0.1 eV, which is attributed to the Al-O bonds. It is noted that the binding energies for Al-O in Al_2O_3 and Al-Al in metallic Al are 74.6$\pm$0.1 eV and 72.2$\pm$0.1 eV, respectively. Thus, Al atoms in the nanostructured AZO films substitute into Zn atoms in AZO crystals (Fang-H. and Tung-H., 2015).

The O1s peak can be deconvoluted to obtaind three composing peaks, as shown in Figure 4.25(b). The percentages of the O1, O2 and O3 were found to be the same for all samples, which are 31.82%, 48.59% and 19.58%, respectively. The low binding energy peak (denoted as O1) centered at 530.4 ± 0.2 eV is assigned to the lattice oxygen component, attributed to the Zn-O bond (Chen et al., 2000). The medium binding energy peak (denoted as O2) centered at $531.4 + 0.2$ eV is attributed to O^{2-} ions on the wurtzite structure of hexagonal Zn^{2+} ions and Al^{3+} ions array, and oxygen species in coordination with carbon contamination. (Song et al., 2001; Weiyan et al., 2011). The high binding energy component (denoted as O3) at $532.7 + 0.2$ eV is associated with chemisorbed or dissociated oxygen on the surface (Fang et al., 2011).
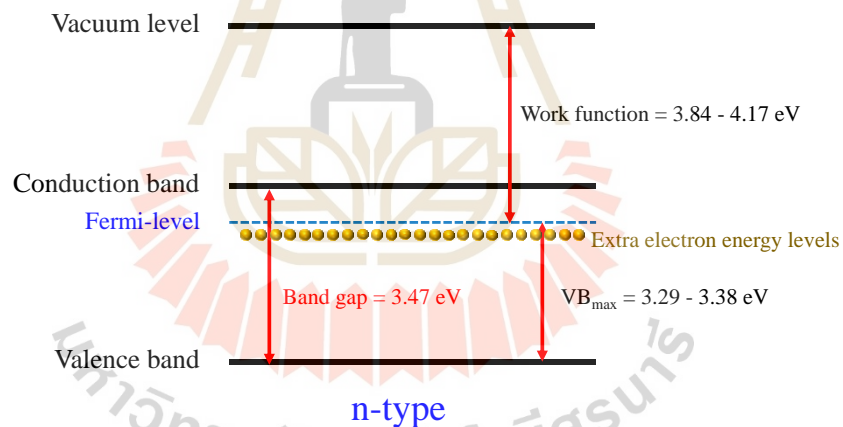
Figure 4.26 Schematic energy diagram of nanostructured AZO films.

Figure 4.25(c) shows the Zn3d and O2p XPS spectra of nanostructured and dense AZO films measured with the excitation of hv=50 eV. They are include the valence band of AZO films, from which the valence band maximum (VBM) could be determined. The position of the VBM was determined from the linear extrapolation of the lowest BE features of the nonbonding O2p states (Chul-H. et al., 2010). The BE of the VBM edge for AZO thin film was lower than that for nanostructured AZO films.

The position of the VBM was 3.27±0.05 eV for dense AZO thin film and 3.35±0.05 eV for the nanostructured AZO film. It is noted that these values are relative to the Fermi level.

The relationship between the percentage of surface chemical composition and rotation speed is shows in Figure 4.25(d). The peak area of the Al2p, O1s, Zn3d, and C1s were used for calculating the atomic fraction of each element in the compound. The ratio of peak area and the relative sensitivities were calculated with 4 main elements and then taken to average for the elemental percentage (Monika et al., 2018). The percent of the Aluminum, Oxygen, Zinc, and Carbon was found to be the same in all samples i.e. 3.20%, 37.97%, 42.92% and 16.05%, respectively. The detected carbon is from to the carbon contamination of absorbance on the surface during the exposure of the films to the ambient atmosphere.

4.5.3 Surface roughness and Electrical properties

Figure 4.27 shows the AFM images of AZO nanostructured and dense AZO thin film (Figures 4.27(f)). The surface roughness as denoted using root-mean-square (RMS) values were 1.80 nm, 1.18 nm, 1.32 nm, 1.03 nm, 3.43 nm and 0.66 nm with the respective, as shown in Figures 4.27(a)-(f). The surface roughness values fluctuate with type of AZO structure films. The vertical structure has high RMS values, but the thin film has low RMS values compared to the other structures. The vertical structure was composed of columns separated due to the effect of ballistic shadowing at an angle incidence, but the thin film structure was coalescence and formation of a continuous film. Thus, the vertical structure has high surface roughness values than the thin film structure. The roughness has an effect on work function (WF), as shown in Figure 4.28(a).

a) 0.02 rpm

RMS = 1.80 nm

b) 0.04 rpm

RMS = 1.18 nm

c) 0.08 rpm

RMS = 1.32 nm

d) 0.16 rpm

RMS = 1.03 nm

e) 10.00 rpm

RMS = 3.20 nm

f) 10.0 rpm Dense

RMS = 1.03 nm
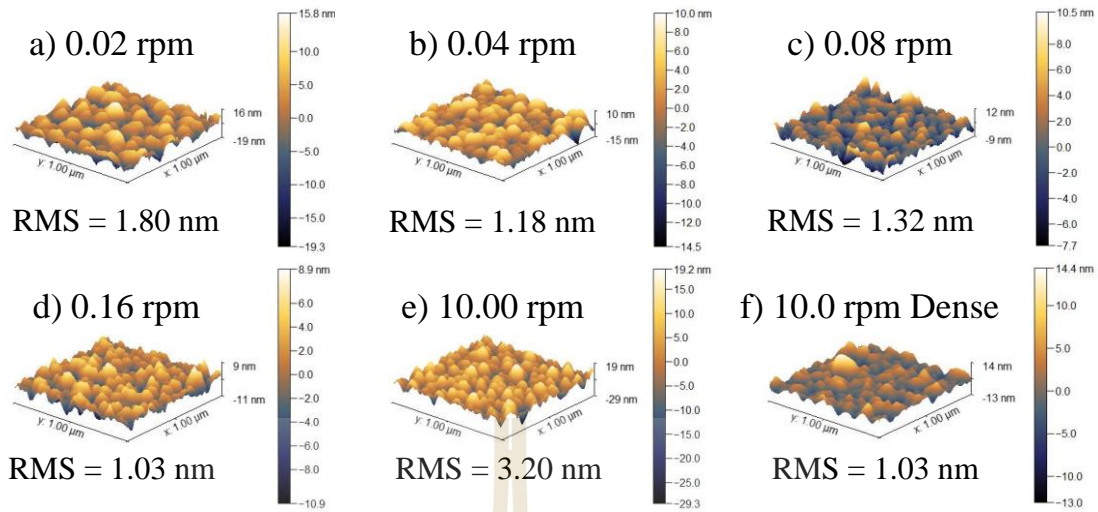
Figure 4.27 AFM images of the surface of nanostructure AZO films (a-e) and AZO thin film (f).

Figure 4.28(a) shows the surface WF value of AZO films for different RMS values. There appears to be a correlation between WF and RMS. The WF values of nanostructures AZO film at speed 0.16 rpm has the lowest to 3.8±0.1eV toward RMS 1.06 nm and at speed 10 rpm has the maximum to 4.2±0.1 eV toward RMS 3.20 nm. The WF was sensitive to surface roughness and some existing results showed that the increase of surface roughness increases WF values (Mingshan et al., 2017). The WF value of AZO thin film was affected by surface roughness, which may be related to the electrostatic action of the patch field that depends on surface morphology. The electrostatic interaction between the electrostatic field and free electron on the surface morphology of nanostructures AZO films were cogitating that movement of the free electron mostly limited at the surface roughness. Thus, the stronger electrostatic interaction has restraint on the escape of free electrons from the Fermi level, cause in increasing the WF of AZO film structure (Mingshan et al., 2016; Li and Li D., 2005).
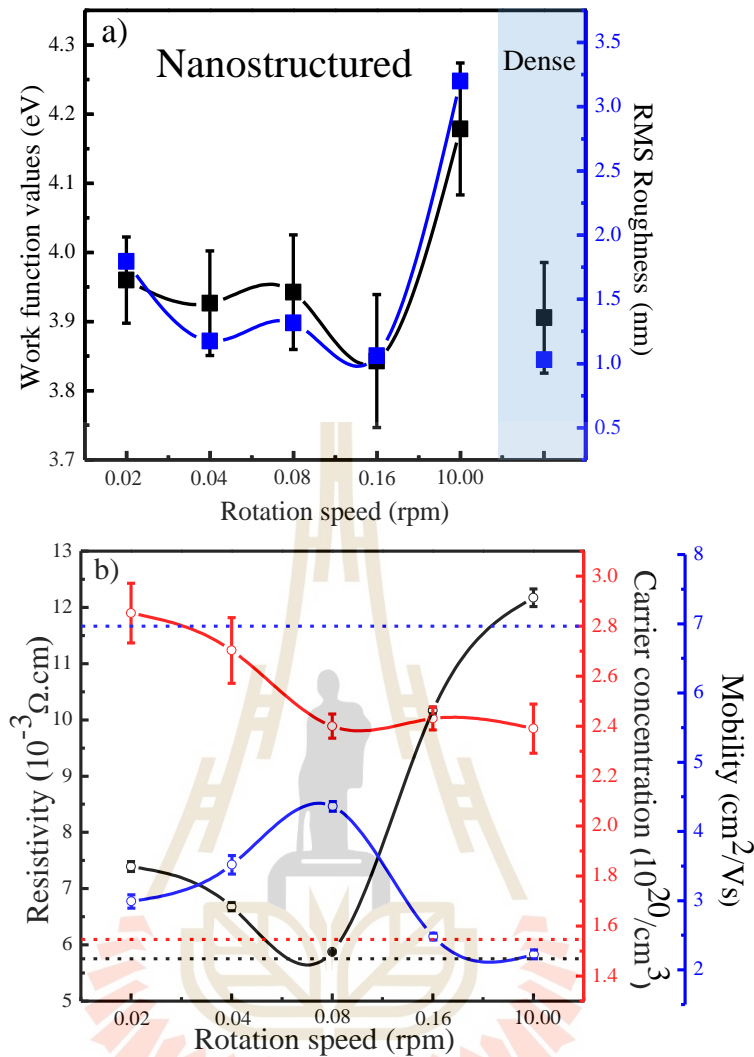
Figure 4.28 (a) The relationship between work function and surface roughness, and (b) results from Hall-Effect masurement of nanostructure AZO films.

Figure 4.28(b) shows the resistivity, mobility, and carrier concentrations for AZO films with the different substrate rotation speeds, as determined from Hall Effect measurements. The values for dense AZO thin film (a dotted line) are also shown in the figure for comparison. The resistivity of AZO nanostructure decreases from 7.39×10^{-3} Ω.cm to 5.87×10^{-3} Ω.cm for the rotation speed from 0.02 to 0.08 rpm and the resistivity was a rise sharply to 12.17×10^{-3} Ω.cm with a rotation speed of 10.0 rpm, where the resistivity was governed by the continuity of the AZO structure films.

The nanostructured AZO films prepared with GLAD technic with difference substrate rotation speed can be observed as a highly disordered mixture between film material and void region. Depositing at a high substrate deposition speed increases the void fraction, reducing the number of percolation of electron paths through the nanostructured AZO films and, thus, the conductivity. For the same reason, the mobility increases from 2.99 cm^2/Vs to 4.36 cm^2/Vs for the samples prepared with rotation speed from 0.02 to 0.08 rpm. At higher speeds, the mobility reduces and is mining at 2.22 cm^2/Vs at the rotation speed of 10.0 rpm.

The carrier concentration of nanostructured AZO films prepared with GLAD technique was found to be between 2.39×10^{20} cm^{-3} to 2.85×10^{20} cm^{-3}. For the dense AZO film the carrier concentration was 1.57×10^{20} cm^{-3}. This shows that the carrier concentration of nanostructured AZO films is slightly higher than that of the dense AZO thin film. Due to the nanostructured AZO films have high surface roughness that free electron is not easy to move and mostly limited on the top of surface. When the system applies to the magnet, the electrostatic field was interaction with free electron at the top of nanostructure, which may be a potential cause of increase electron density to the increases carrier concentration of nanostructured AZO films.

4.5.5 Optical transmission

Figure 4.29(a) shows the optical transmission spectra for all AZO films exhibiting high optical transmittance with the interference fringes. The optical transmittance in the visible region shows the effects of interference, which could be due to its multiple reflection at the surface of the thin films. There is strong absorption in the infrared region. Thus, a fast drop in the infrared region is obvious. It may be

anticipated that the free-carrier absorption mechanism would lead to increasing carrier

concentration and decreases the refractive index (Chao et al., 2016).
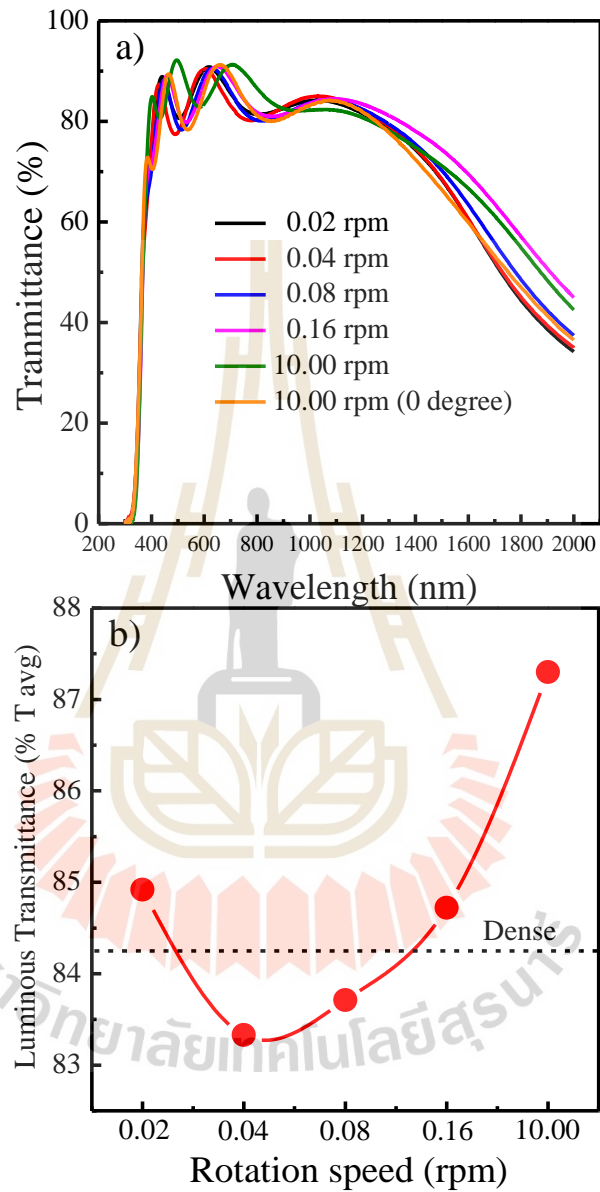
Figure 4.29 (a) UV-visible light transmittance and (b) luminous transmittance of the

nanostructured AZO films with different structures.

Figure 4.29(b) shows average transmittance in the visible region (wavelength

between 380-780 nm) for nanostructured AZO and dense AZO films. It is obvious that

the nanostructured AZO films deposited with rotation speed at 10.00 rpm with GLAD

technic have high average transmittance value (~87.3%).
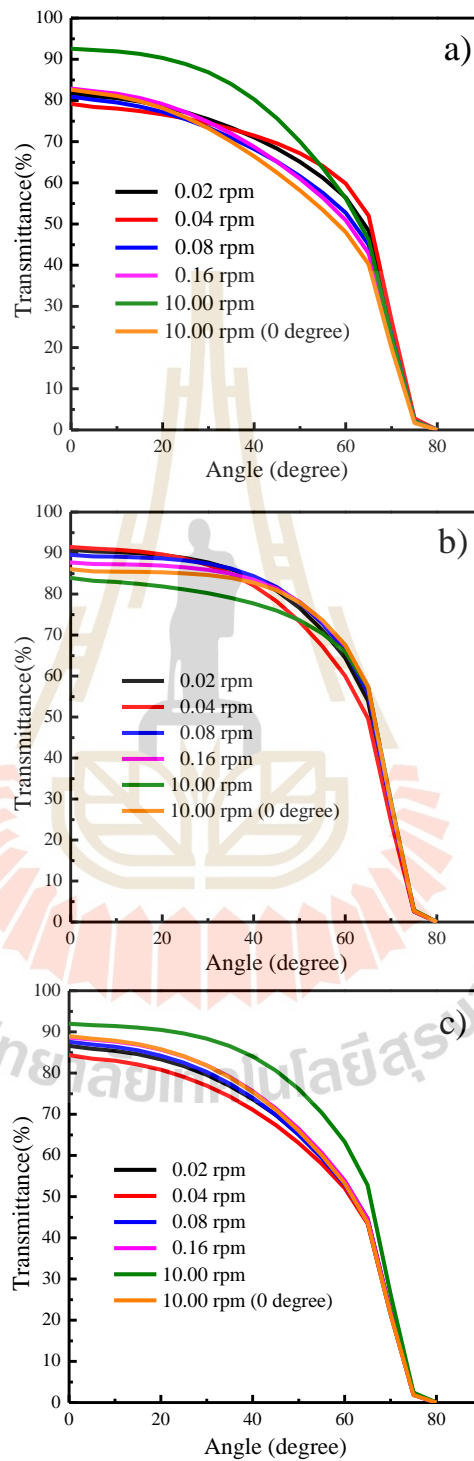
Figure 4.30 The omnidirectional characteristics of all samples at a specific wavelength

of (a) 500 nm, (b) 600 nm, and (c) 700 nm.

Figures 4.30(a)-(c) show the omnidirectional antireflection characteristics at a specific wavelength of 500, 600 and 700 nm measured by using a UV-Vis spectrophotometer with varying the incident angle from -80° to 80°. It is interesting to point out that the sample with a rotation speed of 10.00 rpm shows the maximum light transmission at a wavelength of 500 and 700 nm. The results indicate that the AZO nanocolumnar improves the omnidirectional antireflection due to the fact that the refractive index is gradually increased from the top surface to nanostructure material and the transmittance is not rapidly reduced when increasing the incidence angle due to Fresnel reflection from the rear sides.
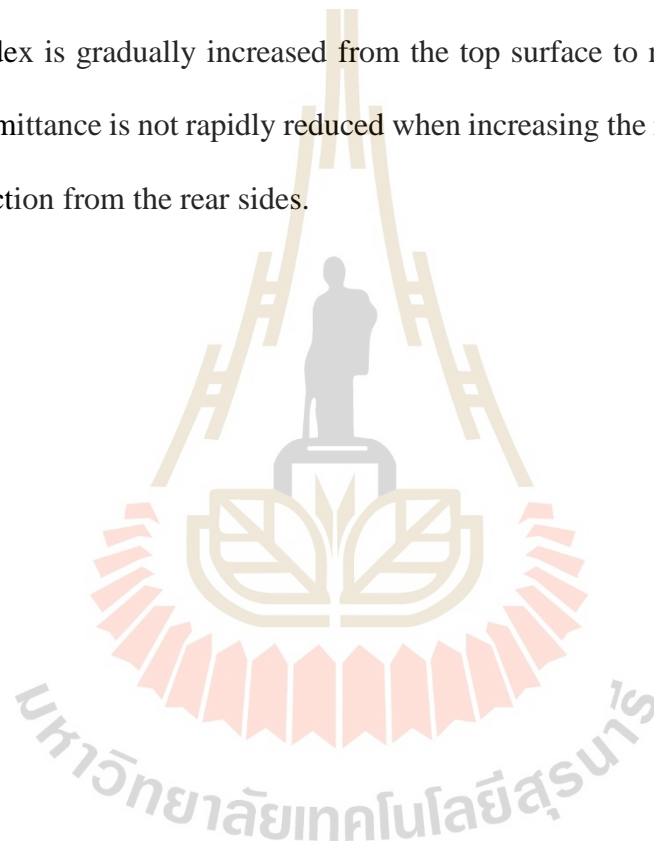
4.6 Influence of post-annealing

The AZO thin films quality is influenced by various parameters in the film preparation process such as substrate temperature, pressure, Al concentration in target material and gas species and flow rate. The pressure and oxygen flow have a considerable effect on the structural and electrical properties. Proper pressure and oxygen flow rate are required to prevent the bonding between Zn/Al and oxygen atom to form the oxide with the Zn/Al atom in the interstitial sites, and such the oxide could not contribute the electrons to the conductivity (Li L. et al., 2012). It is well-known that the conductivity of AZO films can be enhanced by thermal annealing to remove the intrinsic defects and thus improve the crystal quality (Ng Z. et al., 2012; Zhang et al., 2016). In this section, thus, the effects of post annealing treatment of nanocolumnar AZO films in air, low and high vacuum on the physical structure, morphology, optical and electrical property are investigated.

To obtain nanocolumnar AZO thin films, the deposition was performed with an incident deposition flux angle of 85 degrees with respect to the surface normal of the substrate and with 10 rpm substrate rotation speed. The deposition was operated with 125-Watt DC power and with Ar gas flow rate of 80 sccm for 30 minutes. Post-deposition annealing was carried out in a quartz tube furnace at the temperature of 200, 300 and 400°C for 3 hours under three different environments, i.e. in air, low vacuum (1×10^{-3} mbar) and high vacuum (5×10^{-6} mbar). The ramping rate of the temperature was kept at 4°C/s.

4.6.1 Physical morphologies and crystal structures

The cross-section FE-SEM images of the prepared sample deposited on silicon wafer examined are shown in Figure 4.31. As-deposited samples depicts the vertically aligned nanocolumnar AZO film, as shown in Figure 4.31(a). The formations of the vertically aligned nanocolumnar occurred from the self-shadowing effect and the limited adatom diffusion. Figures 4.31(b)-(d) show the FE-SEM images of the nanocolumnar AZO films annealed at 200, 300 and 400°C in different ambient conditions. The result indicates that the nanocolumnar AZO film annealed in air and low vacuum condition remained nearly unchanged within the range of the present annealing temperature. In the case of annealed in high vacuum condition, most of the prepared samples were densely packed.

(a) As-deposited

(b) Annealed in air ambient

(c) Annealed in low vacuum

(d) Annealed in high vacuum
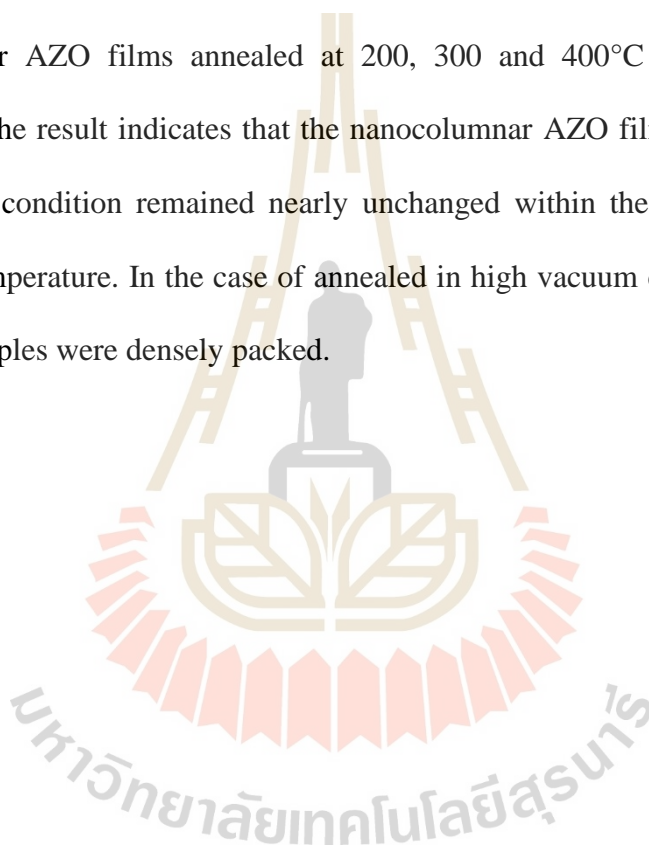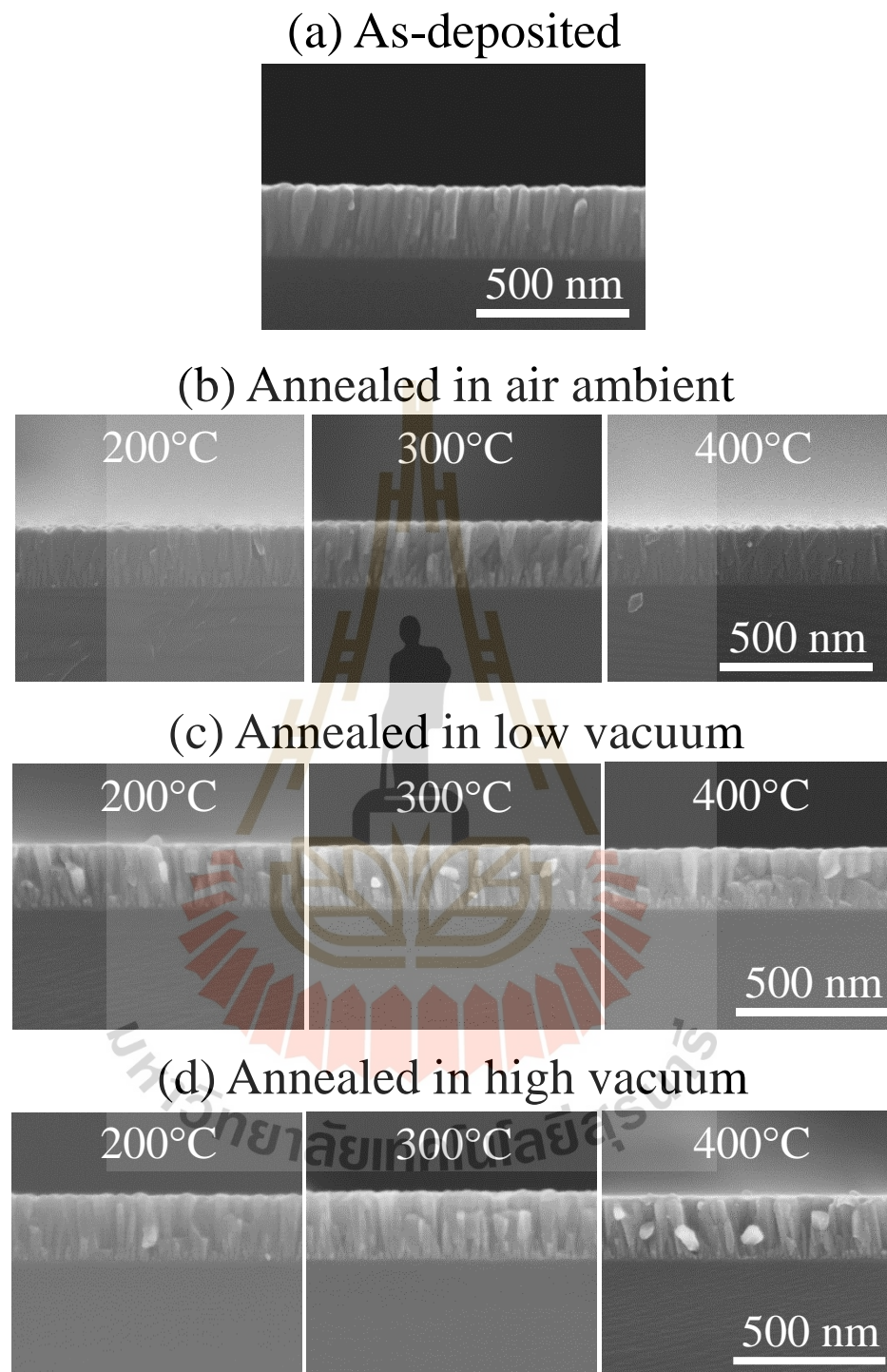
Figure 4.31 Cross-section FE-SEM images of the deposited AZO films before and after annealing at 200, 300 and 400°C in air, low vacuum and high vacuum.

A GIXRD technique was used to characterize the crystal structures of the AZO films before and after annealing at 200, 300 and 400°C in air, low vacuum and high vacuum. The GIXRD pattern indicates that all films have the ZnO hexagonal wurtzite structure with the c-axis preferentially perpendicular to the substrate surface, as shown in Figure 4.32. For the as-deposited film, two diffraction peaks assigned to (002) and (103) planes are observed at diffraction angles of 34.34° and 62.66°, respectively. It is interesting to point out that these two diffraction peaks shift slightly towards higher diffraction angles when increasing the annealing temperature, irrespective of annealing ambient. This is clearly shown in Figure 4.32 for the (002) and (103) peaks, respectively. The increase of the diffraction angles indicates the decrease in the interplanar spacing of the AZO films. The shift of the (002) and (103) peaks, respectively, from 34.34° to 34.66° and 62.67° to 63.09° (shown in Figure 4.32) corresponding to the reduction of the (002) interplanar spacing from 2.609 Å to 2.586 Å after annealing at 400°C in air for 3 hours, as shown in Figure 4.33(a). Comparing to the as-depsited film, the slightly smaller interplanar spacing by 0.87% is observed for the sample annealing in low and high vacuum. The reduction in the interplanar spacing is mainly due to the smaller ionic radius of Al^{+3} comparing to that of Zn^{+2}. In addition, the width of the two diffraction peaks becomes narrower when the annealing temperature increases, as shown in Figure 4.33(b) for the case of the the (002) peak. The reduction of width of the diffraction peaks suggests some changes occurring in the crystallite size in the annealed nanocolumnar AZO films. It is noted that no diffraction peaks of Al_2O_3 were observed.
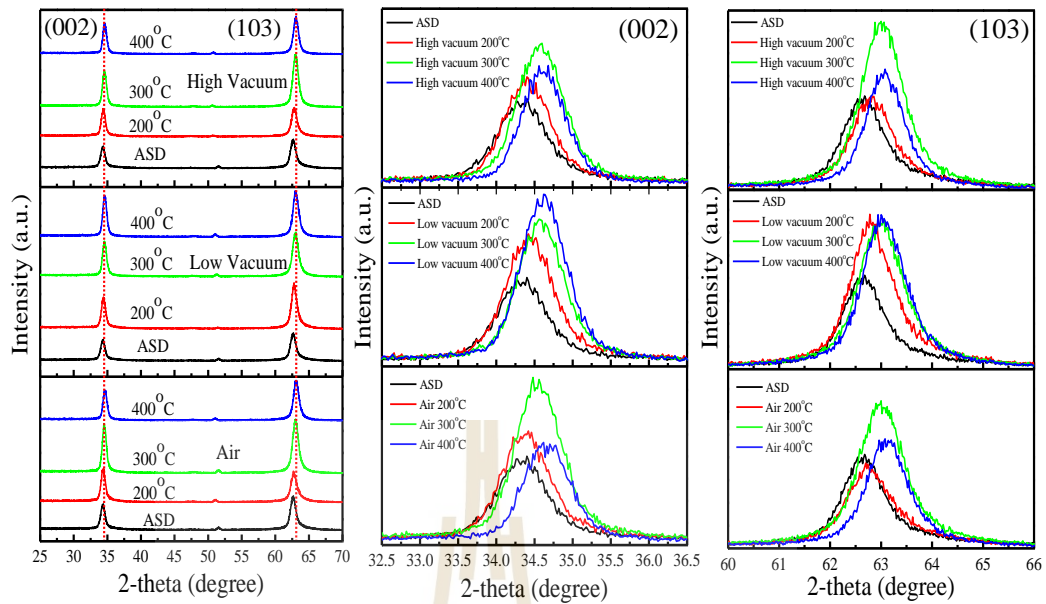
Figure 4.32 GIXRD patterns of nanocolumnar AZO thin films on Si wafer before and after annealing at 200, 300, and 400°C in air, low vacuum, and high vacuum.

Due to the shift and broadening of diffraction peaks, a significant change occurs in crystallite size (Park et al., 1997) and d-spacing of nanocolumnar AZO thin films. The d-spacing between the crystalline planes of (002) could be extrapolated calculate by Bragg equation as shown in Figure 4.33(a). The d-spacing were decreased from 2.609 Å without substrate heating to 2.586 Å at annealing temperature 400°C in air. Because the Al atoms are substituted into the Zn sites in the crystal and the ionic radius of Al^{+3} (53 pm) is much smaller than that of Zn^{+2} (72 pm), so the length of c-axis lattice parameter is expected to be smaller. No diffraction peaks of Al_2O_3 were observed, which implies that Al atoms substitute Zn in the hexagonal lattice and Al ions may occupy the interstitial sites of ZnO or probably Al segregates to the noncrystalline region in grain boundaries and forms Al-O bonds. Figure 4.33(b) shows the relationship between FWHM of the (002) diffraction peak taken from the AZO films before and after annealing at 200, 300 and 400°C in air, low vacuum and high vacuum. FWHM of

the (002) peak decreases with increasing annealing temperature. It is well-known that thermal annealing causes small crystallites to coalesce together to form larger crystallites with improved crystal quality.
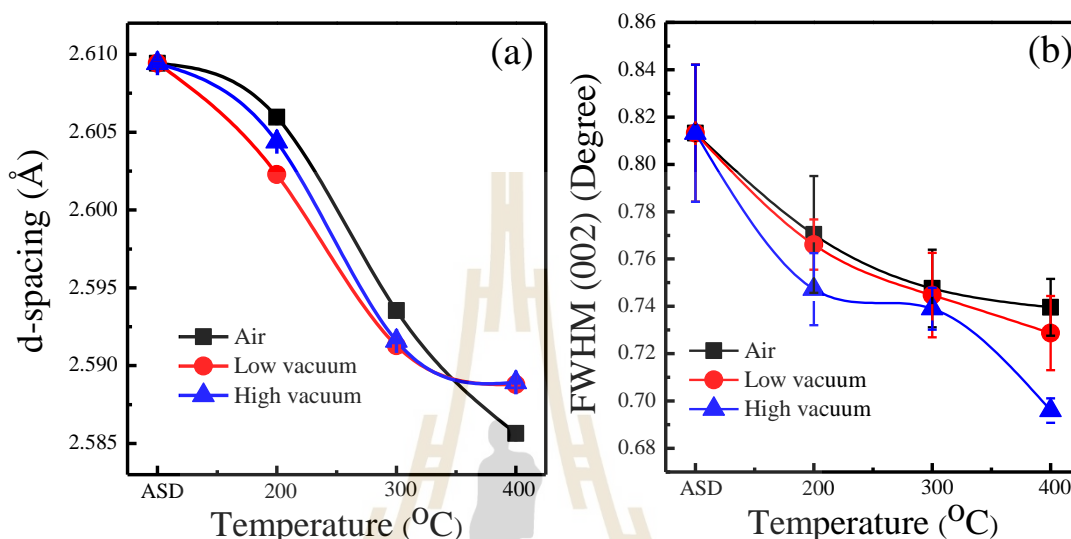
Figure 4.33 The (002) interplanar spacing (a) and FWHM of the (002) diffraction peak (b) of the AZO films before and after annealing at 200, 300 and 400°C in air, low vacuum and high vacuum.

Further microstructural characterization of the nanocolumnar AZO films was performed by high resolution transmission electron microscope (HRTEM). The TEM samples were prepared by scraping the nanocolumnar by a diamond cutter. The scraped flakes were dispersed in ethanol and dropped onto a standard TEM grid. Figure 4.34 depicts a bright field TEM images for the (a) as-deposited AZO nanocolumnars and for those annealed in (b) low vacuum and (c) high vacuum. It was observed that the prepared sample were vertical nanocolumnart structure with diameter and length of 45 and 210 nm, respectively. The HRTEM images (Figure 4.34(e)-(f)) sheds more details on the structure of nanocolumnar. The columns was (002) oriented. The calculated

interplanar distances of 0.261 nm for as-deposited and 0.259 nm for annealed
nanocolumnar AZO samples with agreement with the GIXRD results. The selected area
scanning electron diffraction (SAD) pattern provides diffraction rings in Figures
4.34(g)-(i), clearly display the polycrystalline nature structure of the partially oriented
nanocolumnar AZO samples.
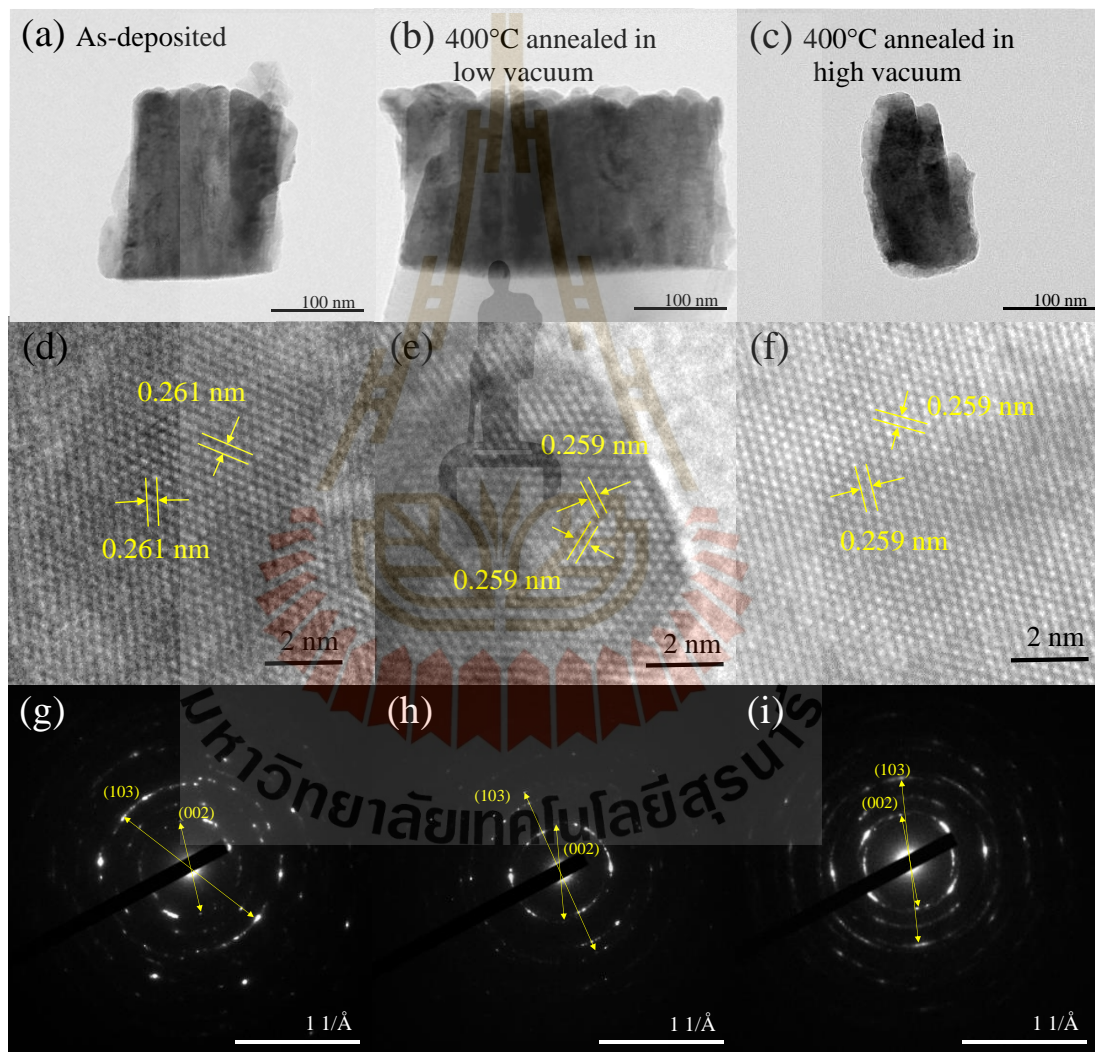
Figure 4.34 (a)-(c) Low resolution TEM images, (d)-(f) high resolution TEM images
and (g)-(i) SAD patterns of the as-deposited, in-low-vacuum annealed and in-high-
vacuum annealed at 400°C AZO films, respectively.

4.6.2 Optical transmission

In the visible light region, all AZO films before and after annealed at different temperatures in different ambient exhibits high optical transmittance with the interference fringes, as shown in Figure 4.35(a). The maximum transmittance occurs at the 650 nm-wavelength, corresponding to the interference effects from the film with the thickness of 230 nm (Ýlker et al., 2001; Ahmed et al., 2009). It is noted that all AZO films annealed in air do not absorb infrared as much as the AZO films annealed in low and high vacuum. This maybe a result of free-carrier absorption mechanism, which increases as the carrier concentration increases. Figure 4.35(b) shows average transmittance in the visible light region (350–780 nm). After annealing, the average the transmittance increases except for the films annealed in air. It is obvious that the AZO films annealed in high vacuum (~86.5%) have the highest average transmittance in the visible light region irrespective of annealing temperature. To evaluate the potential application of omnidirectional anti-reflection characteristics, the angle dependence of transmission at 600 nm-wavelength were carried out over a range of incident angle from -80° to 80° as shown in Figure 4.35(c). The transmittance of a glass slide is also shown for comparison. It is worth noting that, for all samples, the maximum transmittance is obtained at normal incidence and the transmittance is not rapidly reduced when increasing the incidence angle due to Fresnel reflection from the rear sides, providing an opportunity for the solar cell devices.
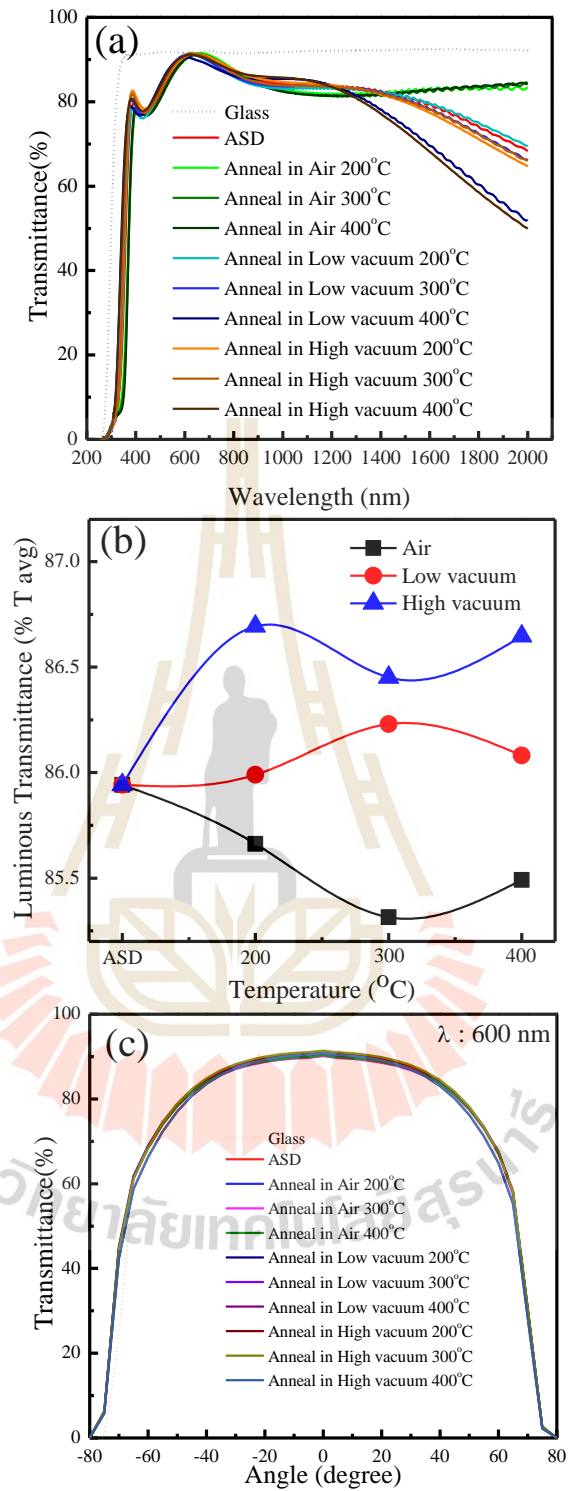
Figure 4.35 The optical transmittance of all AZO films on a glass slide (a) the transmittance integrated over the wavelength between 200 and 2,000 nm, (b) the average transmittance in the visible light region and (c) omnidirectional anti-reflection characteristics.

4.6.3 Electrical properties

The electrical properties of the AZO films were investigated by Hall Effect measurements. The resistivity of the AZO films annealed in low and high vacuum decreases with increasing annealing temperature, as shown in Figure 4.36(a). It is noted that all AZO films annealed in air suffer the problem with the contact for Hall Effect measurements. This may be due to a formation of a high resistive surface layer occurring by the reaction of the AZO film with air molecules, most lightly with chemisorbed oxygen atoms (Jani et al., 2018). The abundant oxygen supply in air would decrease the oxygen vacancy concentration resulting in the conductivity reduction (Feng et al., 2018; Tabassum et al., 2014). The resistivity significantly decreases with the increase in annealing treatment from 200°C to 400°C in low vacuum and high vacuum. Both carrier concentration and mobility increased as annealed temperature increased (Figures 4.36(b) and (c)). The improved electrical property may be attribute to the higher crystalline orientation because shortens carrier path length in a c-axis and the reduction in the scattering of the carrier at the grain boundaries (Raghu et al., 2017).
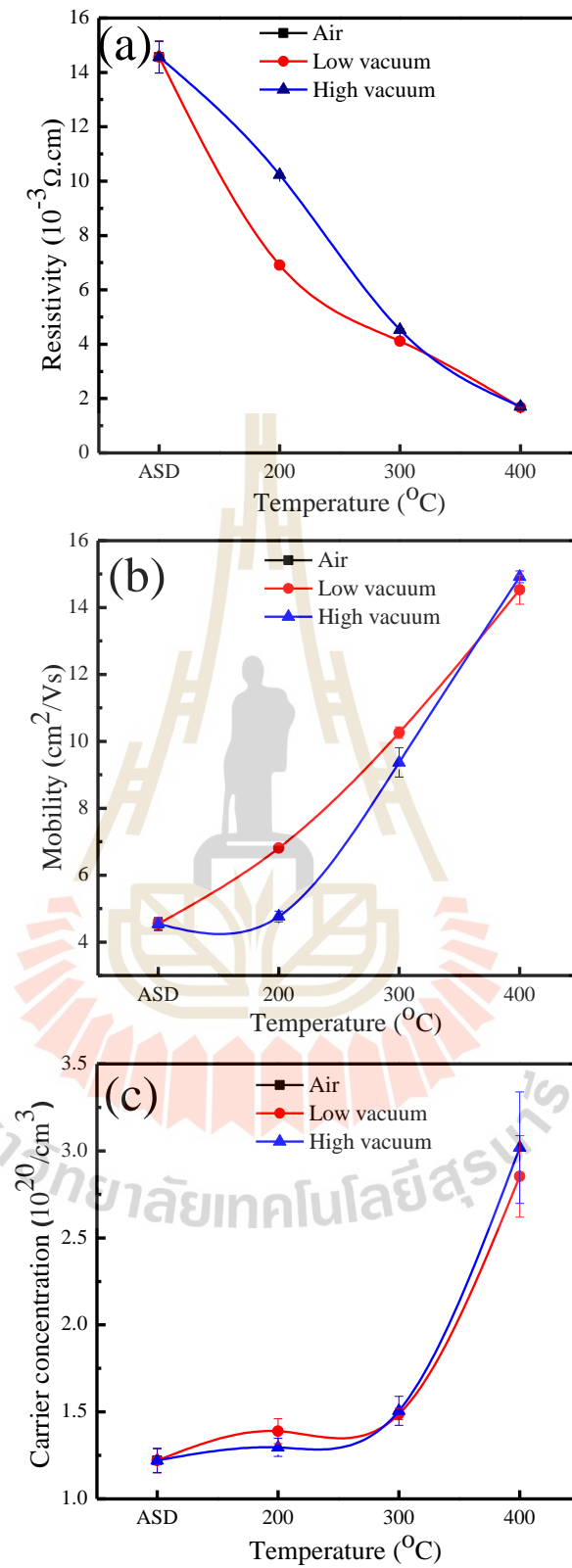
Figure 4.36 The resistivity (a), hall mobility (b), and carrier concentration (c) of AZO

thin films before and after annealing at 200, 300 and 400°C in low and high vacuum.

In summary, post annealing treatment was proposed to archive TCO performance of nanocolumnar AZO film. The effect of annealed ambient on the morphology, crystalline, optical and electrical property has been investigated. The morphology from FE-SEM and HRTEM demonstrates that the as-deposited and annealed samples composed of vertical align nanocolumnar. The result indicates that post annealing treatment process showed little change on the morphology. The crystal structure analysis revealed that all of prepared samples were crystalline with wurtzite structure with preferentially oriented in (200) and (103) direction. The optical transmsission and electrical property results reveal that the annealed ambient affect the transmission in IR region and resistivity due to the higher crystalline orientation. It was found that he high vacuum annealed at 400°C showed high average transmission in visible region of 86.64% with omnidirectional AR property and the resistivity of 1.708×10^{-3} Ω.cm. The post annealing treatment in vacuum process was expected to effectively apply to improved performance of nanocolumnar AZO film.

4.7 Crystal structure of nanostructure AZO films

This section emphasize the study of crystal structure of nanostructured AZO films. As reported from the previous sections, the parameters for deposition processes have been optimized to obtain nanostructured AZO films with good properties as TCO materials. From XRD measurements, there are only two diffraction peaks were observed, as shown in Figure 4.37. The crystals structure of AZO films shows a wurtzite hexagonal structure, as shown in Figure 4.37(a). The observed peaks correspond to the diffraction from the (002) and (103) planes of AZO with the 2-theta angles agreeing with the standard JCPDS (no. 36-1451). The sputtering system for deposition facilitate crystal structure growth with non-random on c-axis oriented direction. Detailed investigations of the crystal structure were carried out further by using TEM in a SAD mode, providing additional evidence confirming the XRD results. SAD observations provide additional information reported below.
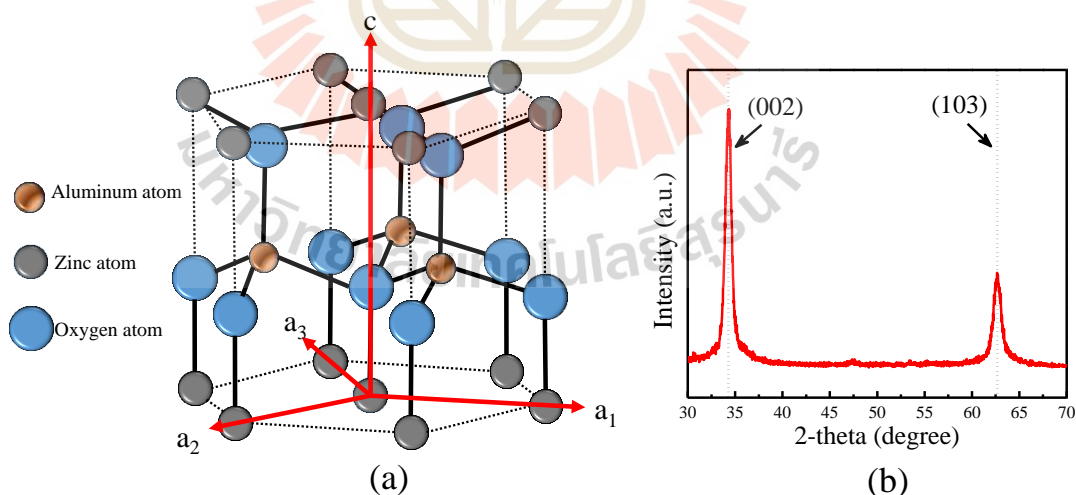
Figure 4.37 (a) AZO with wurtzite structure showing a hexagonal unit cell with lattice parameters a-axis and c-axis and (b) XRD pattern taken from AZO films showing the (002) and (103) peaks.

Figure 4.38(a) shows the cross-section image of TEM. From the TEM image, the thickness of the nanostructure AZO film was determined to about 400 nm. The selected area electron diffraction (SAED) image is shown in Figure 4.38(b). The presence of diffraction spots confirms that AZO exhibits the hexagonal wurtzite structure. Diffused spots or steaks were observed indicating none single crystal. The diffraction spots in Figure 4.38(b) were identified to be from the reflections corresponding to (100), (002), (101), (102), (110), (103), and (201) crystalline planes, with d-spacings of 0.28 nm, 0.26 nm, 0.24 nm, 0.19 nm, 0.16 nm, 0.14 nm, and 0.13 nm, respectively. This is consistent with the XRD (JCPDS, 36-1451) observations that confirmed the hexagonal wurtzite structure. The absence of a complete (002) ring in the SAD of the AZO film indicates that the c-axis growth is preferentially oriented parallel to the film surface. There has been a report that doped Al atoms in ZnO enhance the growth in parallel orientation (c-axis parallel to the film surface) and, thus, increase the intensity of the spots associated with the parallel orientation. For a favorable amount of doped Al atoms, the normal orientation (c-axis normal to the film surface) disappears and the parallel orientation remains (Kiyotaka et al., 2012). Figure 4.38(c) shows a high-resolution TEM (HRTEM) image taken from the nanostructured AZO film, showing the inter-spacing of the (002) planes of 0.26 nm. The elemental compositions of the nanostructured AZO film were determined from EDX spectrum, shown in Figure 4.38(d). It was found that the zinc, oxygen and doping concentrations of Al are 55.2, 42.4 and 2.4 wt. %, respectively.
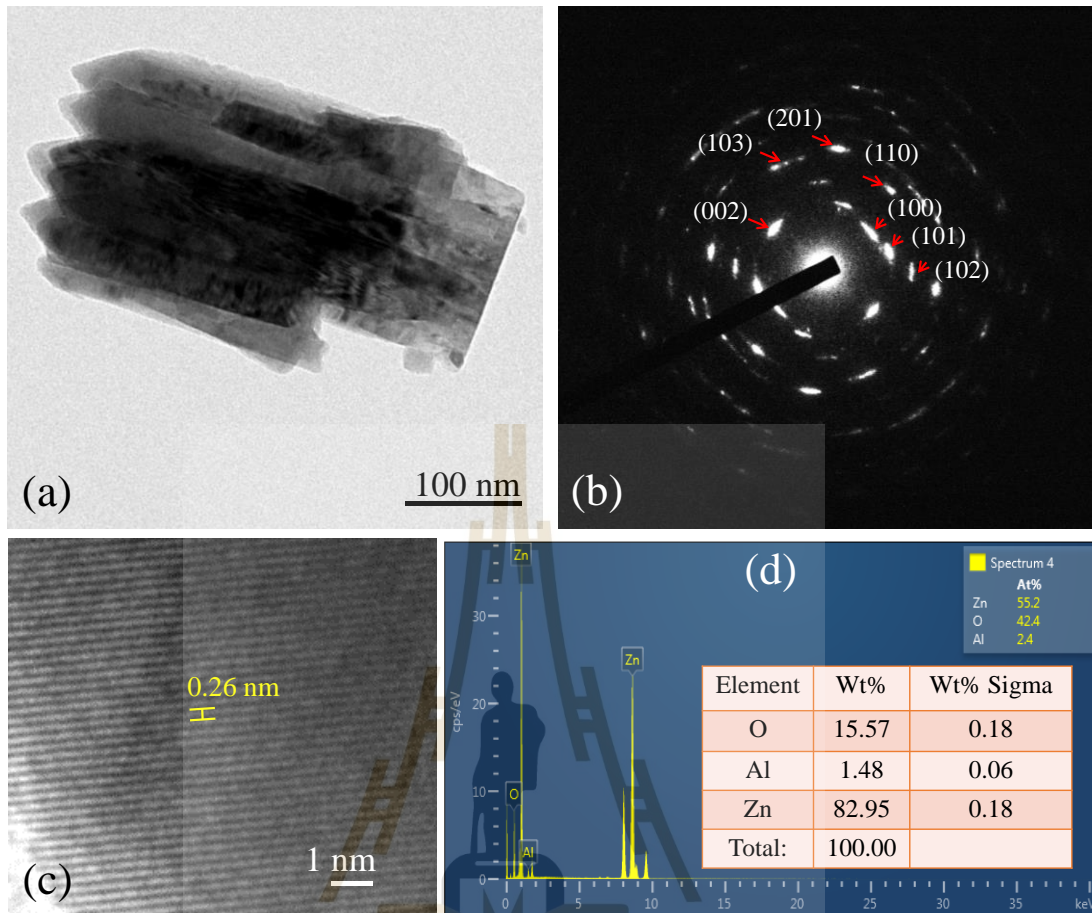
Figure 4.38 (a) Bright-field TEM image, (b) the selected area diffraction pattern (SADP), (c) high-resolution image, and (d) EDX spectrum.

Figure 4.39(a) shows a TEM image of a nanostructured AZO film viewed the c-axis, top view of the film. The top-view TEM image provides the information of the separation and sizes of the grains/nanocolumns. The corresponding SAD pattern is shown in Figure 4.39(b). The diffraction pattern consists of spots and rings, indicating incomplete polycrystallinity, corresponding to the (100), (101), (110), (200), (201), (210), and (300) crystalline planes, with inter-spacings of 0.28 nm, 0.24 nm, 0.16 nm, 0.14 nm, 0.13 nm, 0.10 nm, and 0.09 nm, respectively.
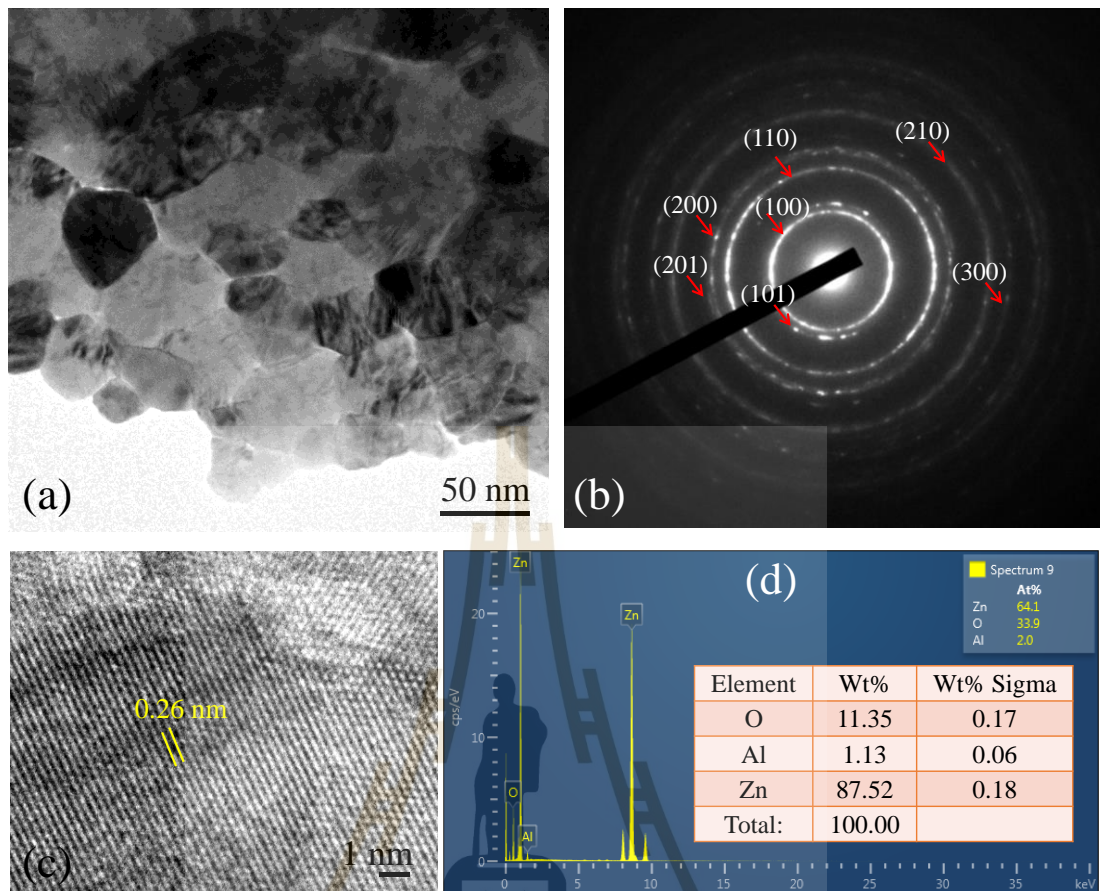
Figure 4.39 (a) Top-view TEM images, (b) SAD pattern, (c) high-resolution images, and (d) EDX spectrum taken from a nanostructured film.

There are obvious differences between SAD patterns taken from AZO film along the direction perpendicular and parallel to the film surface. This is a clear evidence that the film was grown with the c-axis preferentially in the direction normal to the substrate surface. The angular width of the diffraction spot of the (002) planes maybe considered to the angular straggling/deviation of c-axis of AZO. Diffraction rings are more obvious in the SAD pattern taken along the c-axis, in Figure 4.39(b). This indicates that there are rotations of the planes perpendicular to the substrate surface.

Due to, the atom of nanostructured AZO films was non-random or texture (Junichi et al., 2017), which points in the reciprocal lattice was not the sphere, but reciprocal lattice was a layer of difference rings radius in Figure 4.40 (Vera, 2006; Tang et al., 2007). In reciprocal lattice, the Ewald sphere is to determine which lattice planes will result in a reflection spot for the wavelength of an incident beam and show diffraction patterns. HRTEM image observation shows that the distances planes at 0.26 nm of (002) plane in Figure 4.39(c). The EDX in Figure 4.39(d) revealed the presence of Zn, O, and Al elements, and the estimated doping percentage of Al was 2%.
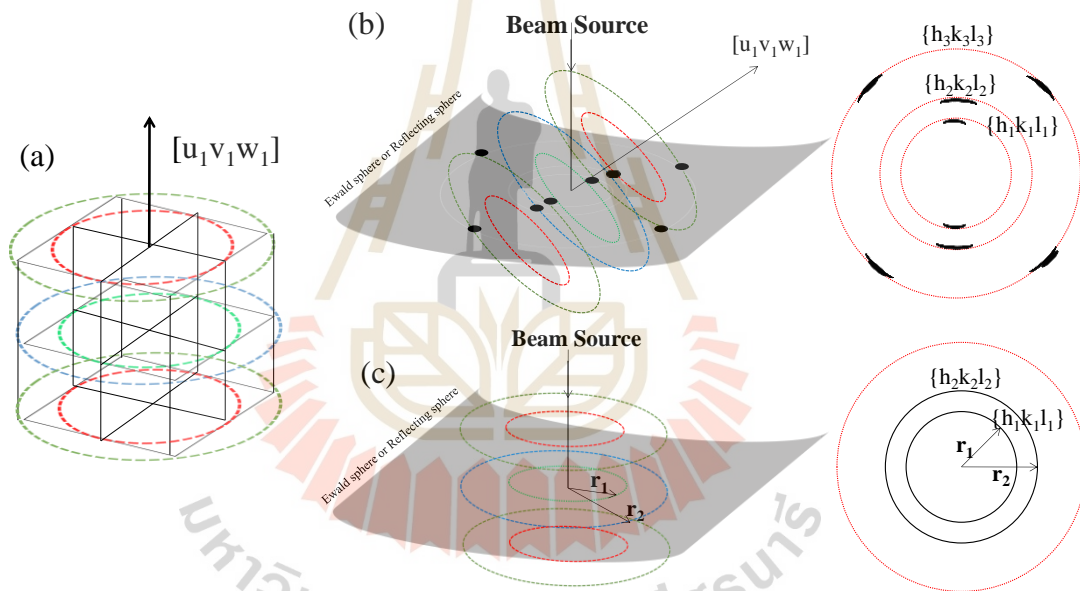
Figure 4.40 (a) The reciprocal lattice of the ring layer, and reciprocal lattice cross the Ewald sphere tilted in [$u_1v_1w_1$] directions (b), and in [$u_1v_1w_1$] directions (c) (Modified from Torranin C., 2012).

In addition to XRD and TEM techniques, grazing incidence X-ray diffraction (GIXRD) technique using synchrotron light was employed to investigate the nanostructured AZO films at the BL7.2W: MX beamline of SLRI. Figure 4.41(a) shows GIXRD data taken from nanostructure AZO films by using synchrotron X-ray with a

wavelength of 1.291Å (9,600eV). Incomplete rings of diffraction were observed as in TEM SAED patterns. Hence, this nanostructured AZO film was not single-crystal and none polycrystalline. The GIXRD image of nanostructured AZO film was converted to a one-dimensional pattern by SAXIT program. Figure 4.41(b) illustrates a one-dimensional diffraction pattern. The crystal structure observed at the beamline results from the (100), (002), (110), (102), (110), (103) and (112) planes whereas the XRD technique was observed two only the diffraction planes of (002) and (103) planes. This is due to the fact that the BL7.2W: MX beamline is equipped with a 2-dimensional detector, similar to observable plane of TEM. GIXRD with a 2D detector has an advantage over TEM in such a way that no special sample preparation is required prior to the measurements.

(a)   (b)
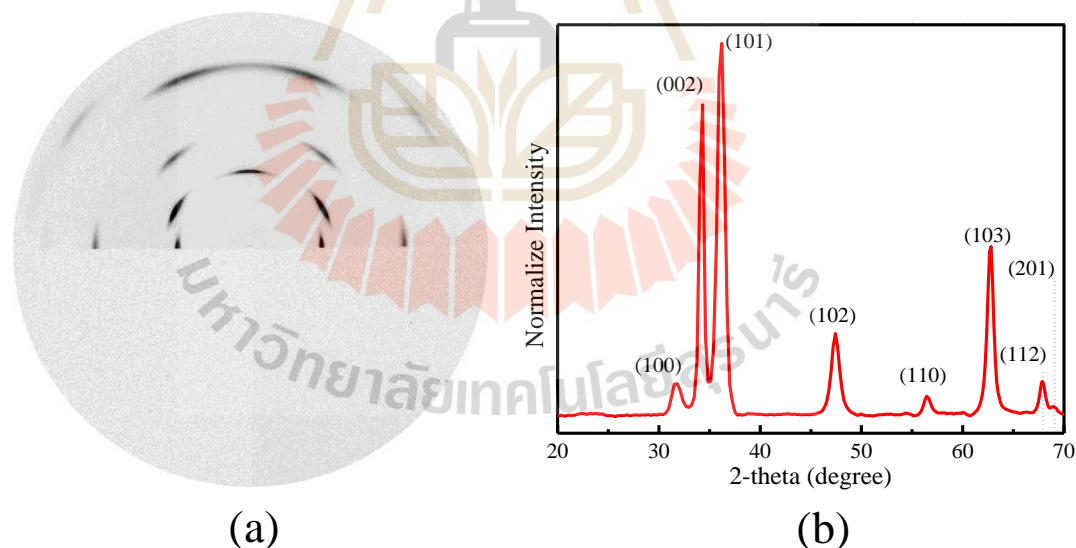
Figure 4.41 (a) 2-diemensional and (b) 1-dimensional GIXRD image of nanostructureds AZO film.

CHAPTER V

CONCLUSIONS

This thesis work focused on fabrication and characterization of nanostructured AZO films with improved electrical and optical properties. The technique employed for the AZO film deposition was a pulsed DC magnetron sputtering with GLAD technique. The deposition processes were optimized with different parameters and conditions, such as argon and oxygen gas flow rates, deposition angle, sputtering power, substrate rotation speed, post-annealing temperature and environments. Electrical, optical and structural properties were investigated during the optimization. The crystals structure of nanostructured AZO films shows a wurtzite hexagonal structure and the diffraction planes at (100), (002), (101), (102), (110), (103), and (121) crystalline planes. The nanostructured AZO films were not single crystal and polycrystalline. The growth of the film exhibits preferential direction, with the c-axis preferable to the normal of the substrate surface.

The increase in oxygen flow rate has a negative effect on the electrical properties, resulting in an increase of the resistivity. Because increasing of oxygen leads to an increase in the number of oxygen vacancies with decreasing free electrons in the crystal structure (Shan et al., 2007). It was found that the best electrical property was obtained when oxygen gas was not used, i.e. with the zero oxygen flow rate.

Changing in the deposition angle introduces the change in shadowing effect. It was found that the shadowing mechanism is enhanced at high deposition angle geometry inducing the condensing vapour to self-assemble and limiting adatoms into oriented nanostructured AZO films. In this work, the optimum deposition angle was chosen to be 85°.

Increasing argon gas flow rate gives rise to higher density of argon ions and, in turn, the sputtering rate of target materials. Thus, the deposition rate increase with the flow rate up to the limit at which caused by self-collision among sputtered atoms. The self-collision phenomenon induces energy dissipation of the sputtered target atoms, preventing them to reach the substrate. The optimum argon gas flow rate was found to be about 80 sccm.

The power supplied to the sputtering magnetron plays also a crucial role for the degree of crystallinity. Too low DC sputtering power yield AZO film with low crystalline quality with small grain size. Increasing the supplied power gives rise to higher kinetic energy of the sputtered atoms and, in turn, yield higher crystalline quality of the AZO film. However, if the sputtering power is too high, there will be an increase in the substrate temperature inhibiting the formation of nanostructures. In this work, a proper power supplied to the magnetron was 125 W.

The last, but not least, parameter to be optimized was the substrate rotation speed. The rotation speed is the main parameter for defining or engineering the structures formed during the growth process. It was demonstrated that different substrate rotation speeds results in different nanostructures. In order to obtain vertical nanostructures with high transmission, the rotation speed was optimized at 10 rpm.

This work also demonstrated that proper post-annealing could also improve the TCO properties of the nanostructured AZO films. Annealing at 400°C in high vacuum yield improved electrical properties, resulting in lower resistivity.

The optimum parameters found for depositing nanostructured AZO films for TCO applications may be summarized as the followings. The deposition shall be carried out with the deposition angle of 85°, sputtering power of 125 W, substrate rotation speed of 10 rpm and argon flow rate of 80 sccm. Oxygen gas flow was not required. After post-annealing at 400°C in high vacuum, the resistivity and average transmittance in visible region were found to be 4.9×10^{-3} Ω.cm and 87%, respectively.

Figures 5(a)-(e) are the comparison charts of various parameters of the AZO film prepared in this work and reported by other research groups. The charts include resistivity, work function, carrier concentration, mobility, and average transmission.

It is worth mentioning that the AZO films prepared in this work exhibits the highest luminous transmittance.
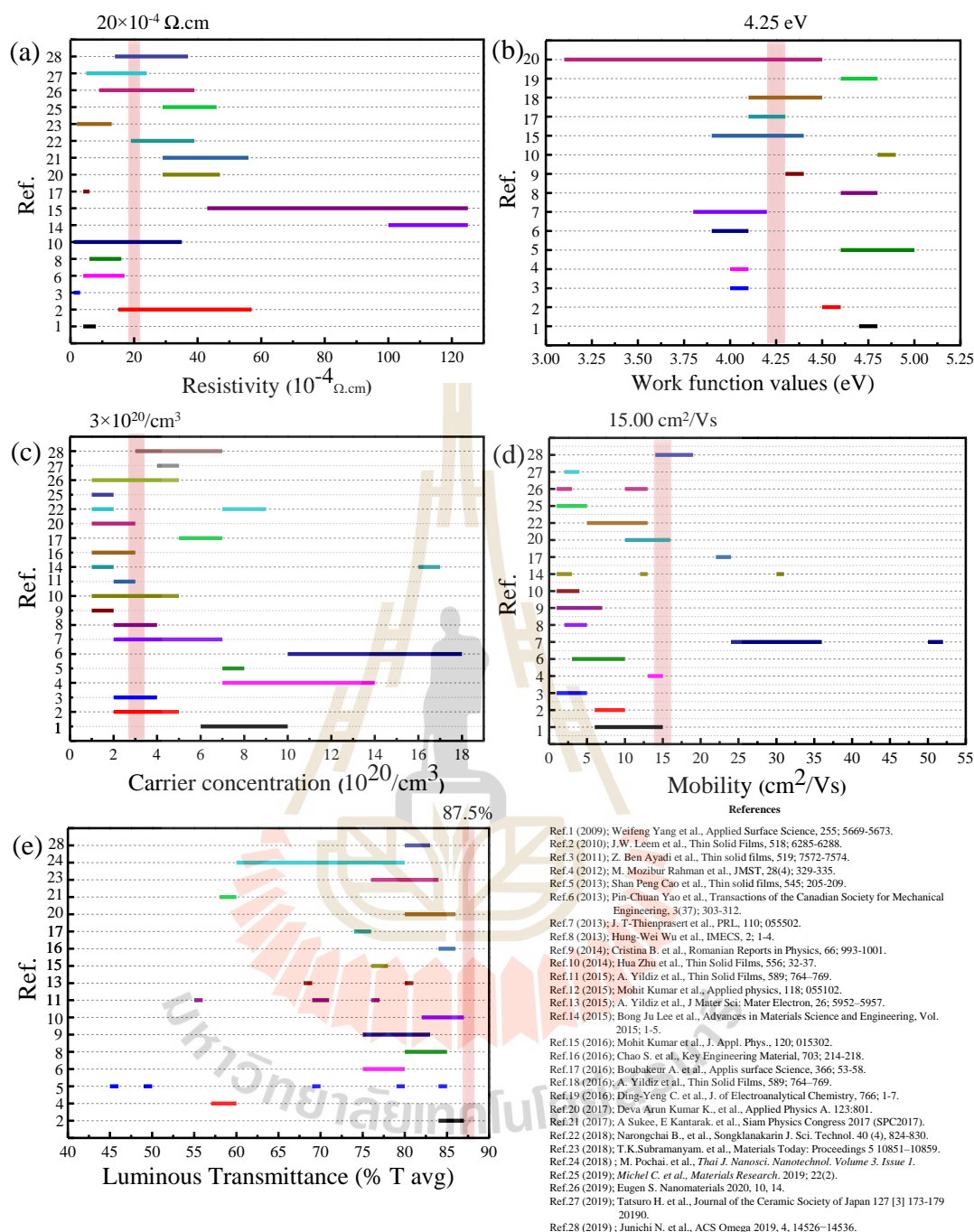
Figure 5 The summary of properties of nanostructure AZO films to compare previous AZO films research on (a) resistivity, (b) work function, (c) carrier concentration, (d) mobility, and (e) average transmission.

REFERENCES
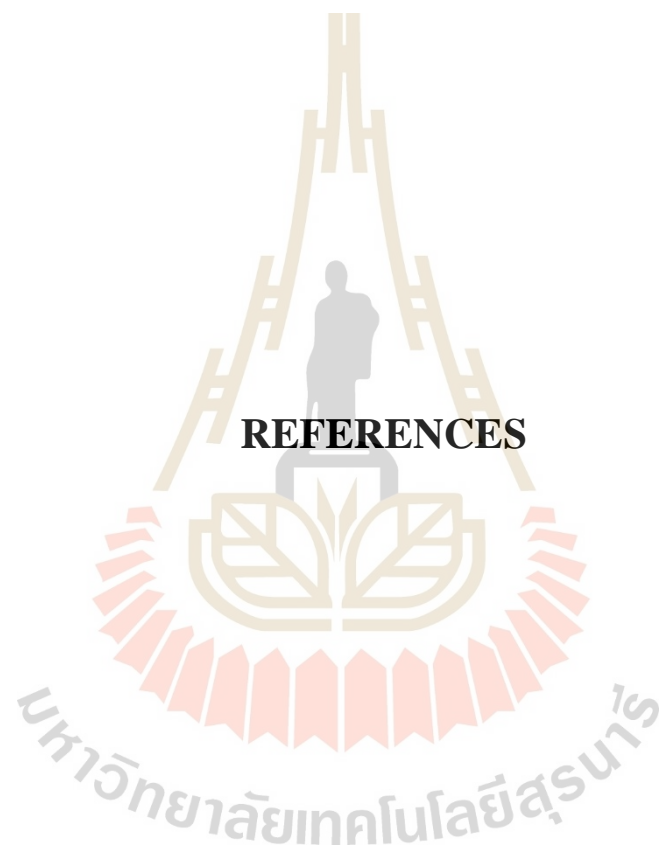
REFERENCES

ธรณินทร์ ไชยเรื่องศรี. (2555). **จุลทรรศนศาสตร์อิเล็กตรอนแบบส่องผ่านพื้นฐานสำหรับโลหะวิทยา และวัสดุศาสตร์.** พิมพ์ครั้งที่ 1. กรุงเทพมหานคร: สำนักพิมพ์แห่งจุฬาลงกรณ์มหาวิทยาลัย.

Ahmed, N. M., Sauli, Z., Hashim, U., and Al-Douri, Y. (2009). Investigation of the absorption coefficient, refractive index, energy band gap, and film thickness for $Al_{0.11} Ga_{0.89} N$, $Al_{0.03} Ga0_{.97} N$, and GaN by optical transmission method. **Int. J. Nanoele. Mat.** 2: 189-195.

Aicha, El., Aicha, E., and Fred, D. B. (1998). **Thin Film Technology Handbook.** United States of America: McGraw Hill Professional.

Alouach, H., and Mankey, G. J. (2004). Texture orientation of glancing angle deposited copper nanowire arrays. **Journal of Vacuum Science and Technology A.** 22: 1379-1382.

Andres, K. (2013). **An Introduction to Electron Microscopy Instrumentation, Imaging and Preparation**. Center for Microscopy and Image Analysis: University of Zurich.

Angel, B., Ana, B., Agustin, R. G., and Alberto, P. (2016). Perspectives on oblique angle deposition of thin films: From fundamentals to devices. **Prog. Mater. Sci.** 76: 59-153.

Ayadi, Z. B., Mri, L. El, Djessas, K., and Alaya, S. (2011). Effect of substrate temperature on the properties of Al-doped ZnO film sputterd from aerogel nanopowders for solar cell applictions. **Thin Solid Films.** 519: 7572-7574.

Ben, A. Z., El, M. L., Djessas, K., and Alaya, S. (2011). Effect of substrate temperature on the properties of Al-doped ZnO films sputtered from aerogel nanopowders for solar cells applications. **Thin Solid Films.** 519: 7572-7574.

Bob, K. (2017). **Atomic Force Microscopy.** Finland: African Institute for Mathematical Sciences (AIMS).

Bradley, A. G. (2007). **Hall Effect Experiment.** Tennessee: The University of Tennessee.

Chaiyan, O., Mati, H., Anurat, W., Thanat, S., Benjarong, S., Saksorn, L., Pitak, E., Ditsayut, P., Noppadon, N., Chanunthorn, C., Viyapol, P., Annop, K., Jakrapong, K., Adisorn, T., and Pongpan, C. (2016). Ultra-sensitive NO_2 sensor based on vertically aligned SnO_2 nanorods deposited by DC reactive magnetron sputtering with glancing angle deposition technique. **Sens. Actuator B-Chem.** 223: 936-945.

Chan, K.-Y., and Teo, B.-S. (2006). Atomic force microscopy (AFM) and X-ray diffraction (XRD) investigations of copper thin films prepared by dc magnetron sputtering technique. **Microelectron. J.** 37: 1064-1071.

Chan, K.-Y., and Teo, B.-S. (2007). Investigation into the influence of direct current (DC) power in the magnetron sputtering process on the copper crystallite size. **Microelectron. J.** 38: 60-62.

Chang, J. F., Wang, H. L., and Hon, M. H. J. (2000). Studying of transparent conductive ZnO: Al thin films by RF reactive magnetron sputtering. **Cryst. Growth**. 211: 93-97.

Chao, P. L., Yishu, F., Kamruzzaman, M., Chun, Y. H., Zapien, J. A., Wei, Z., and Li, Y. J. (2016). Effects of Free Carriers on the Optical Properties of Doped CdO for Full-Spectrum Photovoltaics. **Physical Review A.** 6: 064018.

Chapman, B. (1980). **Glow Discharge Processes.** New York: Wiley.

Chen, M., Wang, X., Yu, Y. H., Pei, Z. L., Bai, X. D., Sun, C., Huang, R. F., and Wen, L. S. (2000). X-ray photoelectron spectroscopy and auger electron spectroscopy studies of Al-doped ZnO films. **Appl Surf Sci.** 158: 134-140.

Chierchia, R., Salza, E., and Mittiga, A. (2014). Effect of Hydrogen Gas Dilution on Sputtered Al:ZnO Film. **Energy Procedia.** 60: 135-142.

Chul, H. M., Suyeon, C., Seung, H. L., Deok, Y. C., Won, G. P., Jae, G. C., Eunha, L., Jae, C L., Benayad, A., Jae, H L., Cheol, S. H., and Se, J. O. (2010). Effect of oxygen partial pressure on the Fermi level of ZnO1−x films fabricated by pulsed laser deposition. **Appl. Phys. Lett.** 96: 201907.

David, B. (2016). **AFM Atomic Force Microscopy.** Canada: University of Toronto.

David, D., and Farinaz, H. (2014). **Quality control of beam splitters and quarterwave-mirrors using the Agilent Cary 7000 Universal Measurement Spectrophotometer (UMS).** Australia: Agilent Technologies.

Daza, L. G., Castro, R. R., and Iribarren, A. (2019). AZO nanocolumns grown by GLAD: adjustment of optical and structural properties. **Mater. Res. Express**. 6-1050b9: 1-14.

Donald, M. M. (2010). **Handbook of Physical Vapor Deposition (PVD).** United States of America: William Andrew.

Dr. Rudy, S. (2007). **Tutorial on Work Function** [On-line]. Available: https://mmrc.caltech.edu/XPS%20Info/TutorialsWorkFunction%20Schlaf.pdf.

Fang, H. W., and Tung, H. Y. (2015). Effect of hydrogen doping on the properties of Al and F co-doped ZnO films for thin film silicon solar cell applications. **Thin Solid Films.** 1-9.

Fang, H. W., Hung, P. C., Chih, C. T., and Chia, C. H. (2011). Effects of H2 plasma treatment on properties of ZnO:Al thin films prepared by RF magnetron sputtering. **Surf Coat Tech.** 205: 5269-5277.

Feng, Z., Huang, L., Feng, Q., Li, X., Zhang, H., Tang, W., Zhang, J., and Hao, Y. (2018). Influence of annealing atmosphere on the performance of a β-Ga$_2$O$_3$ thin film and photodetector. **Opt. Mater. Express.** 8: 2229-2237.

Floro, J., Michael, J., Brewer, L., and Hsu, J. (2011). Preferred heteroepitaxial orientations of ZnO nanorods on Ag. **J. Mater. Res.** 25: 1352-1361.

Gao, W., and Li, Z. W. (2008). Photoluminescence properties of ZnO films grown by wet oxidation: effect of processing. **J. Alloys Compd.** 449: 202-206.

Ginley, D. S., Hosono, H., and Paine, D. C. (2010). **Handbook of Transparent Conductors**. London: Springer.

Hadis, M., and Ümit, Ö. (2009). **Zinc Oxide: Fundamentals, Materials and Device Technology.** United States of America: WILEY-VCH.

Hawkeye, M. M., Taschuk, M. T., and Brett, M. J. (2014). **Glancing Angle Deposition of Thin Films.** First ed. John Wiley & Sons, Ltd, United Kingdom: Introduction: Glancing Angle Deposition Technology.

Hernández, M. A. , Álvaro, R. , Serrano, S. , and Krämer, J. L. C. (2011). Catalytic growth of ZnO nanostructures by rf. magnetron sputtering. **Nanoscale Res Lett.** 437: 1-6.

Hidetoshi, F. A., Hiromichi, E., and Yasushi, W. (1969). Theory of Hall Effect. I. **Progress of Theoretical Physics.** 42: 494-511.

Horprathum, M., Limwichean, K., Wisitsoraat, A., Eiamchai, P., Aiempanakit, K., Limnonthakul, P., Nuntawong, N., Patthanasettakul, V., Tuantranont, A., and Chindaudom, P. (2013). NO_2-sensing properties of WO_3 nanorods prepared by glancing angle DC magnetron sputtering. **Sens. Actuators B Chem.** 176: 685-691.

Horprathum, M., Srichaiyaperk, T., Samransuksamer, B., Wisitsoraat, A., Eiamchai, P., Limwichean, S., Chananonnawathron, C., Aiempanakit, K., Nuntawong, N., Patthanasettakul, V., Oros, C., Porntheeraphat, S., Songsiriritthigul, P., Nakajima, H., Tuantranont, A., and Chindaudom, P. (2014). Ultrasensitive Hydrogen Sensor Based on Pt-Decorated WO_3 Nanorods Prepared by Glancing-Angle dc Magnetron Sputtering. **ACS Appl. Mater. Interfaces**. 6: 22051-22060.

Hung, W. W., Ru, Y. Y., Chin, M. H., and Chien, H. C. (2013). Characterization of aluminum-doped zinc oxide thin films by RF magnetron sputtering at different substrate temperature and sputtering power. **J Mater Sci: Mater Electron 24:** 166-171.

Hwa, M. K., Kang, B., and Sunyoung, S. (2011). Electronic and Optical Properties of Indium Zinc Oxide Thin Films Prepared by Using Nanopowder Target. **Jpn. J. Appl. Phys.** 50: 1-5.

Ik, H. S., and Bae, K. H. (2016). A Study on Properties of RF-sputtered Al-doped ZnO Thin Films Prepared with Different Ar Gas Flow Rates. **Appl. Sci. Converg. Technol.** 25: 145-148.

Ilker, A., and Hüseyýn, T. (2001). Optical Transmission Measurements on Glow-Discharge Amorphous Silicon Nitride Films. **Turk. J. Phy.** 25: 215-222.

István, Z. J. (2012). **Scanning electron microscopy (SEM) analysis of tribolms enhanced by fullerene-like nanoparticles.** Thesis for the degree of Licentiate in Physics Department of Physics, Stockholm University.

James, M. P. (1995). **Handbook of Optics: Devices, Measurements, and Properties, Volume II, Second Edition: Chapter 25 (2th ed.).** New York: McGRAW-HILL, INC.

Jani, M., Raval, D., Pati, R. K., Mukhopadhyay, I., and Ray, A. (2018). Effect of annealing atmosphere on microstructure, optical and electronic properties of spray-pyrolysed In-doped $Zn(O,S)$ thin films. **Bull. Mater. Sci.** 41: 22.

Jeung, H. P., Yong, C. C., Jong, M. S., Su, Y. C., Chae, R. C., Hye, S. K., Su, J. Y., Se-Young, J. Sang, E. P., and Ae-Ran, L. (2007). A Study of Transparent Conductive Aluminum-Doped Zinc Oxide Fabricated on a Flexible Polyethersulphone (PES) Substrate **J. Korean Phys. Soc.** 51: 1968-1972.

Jiang, X., Wong, F. L., Fung, M. K., and Lee, S. T. (2003). Aluminum-doped zinc oxide films as transparent conductive electrode for organic light-emitting devices. **Appl. Phys.** 83: 1875.

Jimenez, G. A. E., Jose, A., and Suarez, P. R. (1998). Optical and electrical characteristics of aluminum-doped ZnO thin films prepared by solgel technique. **J. Cryst. Growth.** 192: 430-438.

John, A. (1987). Thornton Structure-Zone Models of Thin Films. **Modeling of Optical Thin Films.** 821: 95-103.

John, F. W., and John, W. (2003). **An Introduction to Surface Analysis by XPS and AES.** England: John Wiley & Sons, Ltd.

Junichi, N., Katsuhiko, I., Shintaro, K., Takeshi, W., Hisao, M., and Tetsuya, Y. (2017). Characteristics of carrier transport and crystallographic orientation distribution of transparent conductive Al-doped ZnO polycrystalline films deposited by radio-frequency, direct-current, and radio-frequency-superimposed direct-current magnetron sputtering. **Materials.** 10-916: 1-18.

Junqing, Z., Shijie, X., Shenghao, H., Zhiwei, Y., Lina, Y., and Tianlin, Y. (2000). Organic light-emitting diodes with AZO films as electrodes. **Synth. Met.** 114: 251-254.

Kalsoom, A., Shahid, A. K., Sher, B. K., and Abdullah, M. A. (2018). **Handbook of Materials Characterization.** Switzerland: Springer International Publishing AG.

Kar, J. P., Kim, S., Shin, B., Park, K. I., Ahn, K. J., Lee, W., Cho, J. H., and Myoung, J. M. (2010). Influence of sputtering pressure on morphological, mechanical and electrical properties of Al-doped ZnO films. **Solid-State Electronics.** 54: 1447-1450.

Kiyotaka, W., Isaku, K., and Hidetoshi, K. (2012). **Handbook of Sputter Deposition Technology.** 2nd Edition. New York; William Andrew Book**.**

Klaus, E., Andreas, K., and Bernd, R. (2008). **Transparent Conductive Zinc Oxide Basics and Applications in Thin Film Solar Cells.** United States of America: Springer.

Ko, H. J., Chen, Y. F., Hong, S. K., Wenisch, H., Yao, T., and Look, D. C. (2000). Ga-doped ZnO films grown on GaN templates by plasma-assisted molecular-beam Epitaxy. **Appl. Phys. Lett.** 77: 3761.

Krishna, S. (2002). **Handbook of Thin-film Deposition Processes and Techniques.** United States of America: Noyes Publications.

Kumar, M., Singh, R., Nandy, S., Ghosh, A., Rath, S., and Som, T. (2016). Tunable optoelectronic properties of pulsed dc sputter-deposited ZnO:Al thin films: Role of growth angle. **J. Appl. Phys.** 120: 015302.

Laya, D. S., Mohammad, E., Heydar, H. N., Hossein, E., Shahram, S., and Atefeh, G. (2015). Structural and optical characterization of ZnO and AZO thin films: the influence of post-annealing. **J Mater Sci: Mater Electron.** 27: 1-12.

Leem, J. W., and Yu, J. S. (2010). Structural, optical, and electrical properties of AZO films by tilted angle sputtering method. **Thin Solid Films.** 518: 6285-6282.

Li, L. N., Zhao, Y., Chen, X. L., Sun, J., and Zhang, X. D. (2012). Effects of oxygen flux on the aluminum doped zinc oxide thin films by direct current magnetron sputtering. **Physics Procedia.** 32: 687-695.

Li, W., and Li, D. Y. (2005). On the correlation between surface roughness and work function in copper. **J. Chem. Phys**. 122: 064708.

Lin, Y. C., Chen, T. Y., Wang, L. C., and Lien, S. Y. (2012). Comparison of AZO, GZO, and AGZO Thin Films TCOs Applied for a-Si Solar Cells. **J. Electrochem. Soc.** 159: H599-H604.

Liu, H., Avrutin, V., Izyumskaya, N., Özgur, Ü., and Morkoç, H. (2010). Transparent conducting oxides for electrode applications in light emitting and absorbing devices. **Superlattice Microst.** 48: 458-484.

Lu, Y. F., Ni, H. Q., Mai, Z. H., and Ren, Z. M. (2000). Interaction of P$_b$ defects at the (111)vSi/SiO$_2$ interface with molecular hydrogen: Simultaneous action of passivation and dissociation. **J. Appl. Phys.** 88: 498.

Matthew, M. H., Michael, T. T., and Michael, J. B. (2014). **Glancing Angle Deposition of Thin Films.** United Kingdom: John Wiley & Sons, Ltd.

Messier, R., Giri, A. P., and Roy, R. A. (1984). Revised structure zone model for thin film physical structure. **J. Vac. Sci. Technol. A.** 2: 500-503.

Meyer, B. K., Sann, J., Hofmann, D. M., Neumann, C., and Zeuner, A. (2005). Shallow donors and acceptors in ZnO. **Semicond. Sci. Technol.** 20: S62.

Michihiro, S., Kazuhiro, M., Hiroyuki, K., and Takafumi, Y. (2004). Role of hydrogen in molecular beam epitaxy of ZnO. **J. Appl. Phys.** 95: 5527-5531.

Milton, O. (200). **Materials Science of Thin Films 2nd Edition.** United Kingdom: Academic Press.

Mingshan, X., Sibo, P., Fajun, W., Junfei, O., Changquan, L., and Wen, L. (2016). Linear relation between surface roughness and work function of light alloys. **J. Alloys Compd.** 692: 903-907.

Mingshan, X., Yao, Y., Junfei, O., Fajun, W., Yao, Q., and Wen, L. (2017). Effect of surface roughness on electron work function of AZ31 Mg alloy and their Correlation. **J. Alloys Compd.** 731: 44-48.

Miskawan, S. (2018). **Development of grazing incidence x-ray diffraction technique using synchrotron light.** Master of Science in Physics, Suranaree University of Technology.

Monika, K., Barbara, L.-S., Anna, K., Monika, M., Michal, A. B., Eliana, K., and Jacek, S. (2018). Surface Properties of Nanostructured, Porous ZnO Thin Films

Prepared by Direct Current Reactive Magnetron Sputtering. **Materials.** 131: 1-11.

Mukherjee, S., and Gall, D. (2012). Structure zone model for extreme shadowing conditions. **Thin Solid Films.** 2012: 1-6.

Nakajima, H., Chaichuay, S., Sudmuang, P., Rattanasuporn, S., Jenpiyapong, W., Supruangnet, R., Chanlek, N., and Songsiriritthigul, P. (2016). Commissioning of the soft x-ray undulator beamline at the Siam Photon Laboratory. **AIP Conf. Proc.** 7141: 020040.

Naser, M. A., Zaliman, S., Uda, H., and Yarub, Al-D. (2009). Investigation of the absorption coefficient, refractive index, energy band gap, and film thickness for Al0.11Ga0.89N, Al0.03Ga0.97N, and GaN by optical transmission method. **Int. J. Nanoelectronics and Materials**, 2: 189-195.

Nathaporn, P., Pitoon, N., Peerasil, C., Rawiwan, C., Supanit, P., Bunpot, S., Tanapoj, C., Benjarong, S., Peerapong, N., Chanunthorn, C., Saksorn, L., Mati H., Pitak, E., and Viyapol, P. (2019). Study of Annealing Influence on Basic Properties of Indium Tin Oxide Nanorod Films Deposited Using Glancing Angle Ion-Assisted Electron Beam Evaporation. **J. Nanosci. Nanotechnol.** 19: 1432-1438.

Ng, Z.-N., Chan, K.-Y., and Tohsophon, T. (2012). Effects of annealing temperature on ZnO and AZO films prepared by sol–gel technique. **Appl. Sure. Sci.** 258: 9604-9609.

Nicodemus, E. W. (2016). Introduction to Advanced X-ray Diffraction Techniques for Polymeric Thin Films. **Coatings.** 54: 1-7.

Noureddine, B. H. T., Radhouane, B. H. T., Ben, S. A., and Andre, S. (2008). Effects of Individual Layer Thickness on the Microstructure and Optoelectronic

Properties of Sol–Gel-Derived Zinc Oxide Thin Films. **J. Am. Ceram. Soc.** 91: 846-851.

Nuchuaya, P., Chaikeereea, T., Horprathum, M., Mungkung, N., Kasayapanand, N., Oros, C., Limwichean, S., Nuntawong, N., Chananonnawathorn, C., Patthanasettakul, V., Muthitamongkol, P., Samransuksamer, B., Denchitcharoen, S., Klamchuen, A., Thanachayanont, C., and Eiamchai, P. (2017). Engineered omnidirectional antireflection ITO nanorod films with super hydrophobic surface via glancing angle ion-assisted electron-beam evaporation deposition. **Curr. Appl. Phys.** 17: 222-229.

Park, K. C., Ma, D. Y., and Kim, K. H. (1997). The physical properties of Al-doped zinc oxide films prepared by RF magnetron sputtering. **Thin Solid Films.** 305: 201-209.

Park, Y., Choong, V., Gao Y., Hsieh, B. R., and Tang, C. W. (1996). Work function of indium tin oxide transparent conductor measured by photoelectron spectroscopy. **Appl. Phys. Lett.** 68: 2699-2071.

Peter, G. (2011). **Aberration-Corrected Analytical Transmission Electron Microscopy, First Edition.** United Kingdom: John Wiley & Sons, Ltd.

Proost, J., Henry, F., Tuyaerts, R., and Michotte, S. (2016). Effect of internal stress on the electro-optical behaviour of Al-doped ZnO transparent conductive thin films. **J. Appl. Phys.** 120: 075308.

Qianqian, D., Wenjun, W., Shuhong, L., Dong, Z., and Wanquan, Z. (2016). Effects of substrate temperature on the structural, optical and resistive switching properties of HfO_2 films. **Thin Solid Films.** 608: 21-25.

Raghu, P., Srinatha, N., Naveen, C. S., Mahesh, H. M., and Angadi, B. (2017). Investigation on the effect of Al concentration on the structural, optical and electrical properties of spin coated Al:ZnO thin films. **J. Alloy. Compd.** 694: 68-75.

Raizer, Y. P. (1991). **Gas Discharge Physics.** Berlin Heidelberg New York: Springer.

Richard, J. D. T. (2006). **Crystals and crystal structures.** United Stared: john wiley & sons ltd.

Robert, A. W., and Heather, A. B. (2006). **Basic Theory Atomic Force Microscopy (AFM).** Kentucky: Northern Kentucky University.

Robert, W. M. (2011). **Application of Transparent Conducting Thin Films.** London: University College London. 76-85.

Roth, A. P., and Williams, D. F. (1981). Properties of zinc oxide films prepared by the oxidation of diethyl zinc. **J. Appl. Phys.** 52: 6685.

Rueben, J. M., Guillermo, G., and Delia, J. Mi. (2012). Extracting reliable electronic properties from transmission spectra of indium tin oxide thin films and nanocrystal films by careful application of the Drude theory. **Appl. Phys.** 111: 063515.

Sang-Moo, P., Tomoaki, I., Kenji, E., and Paik-Kyun, S. (2006). Structure and properties of transparent conductive doped ZnO films by pulsed laser deposition. **Appl. Surf. Sci.** 253: 1522-1527.

Schlaf, R., Murata, H., and Kafafi, Z. H. (2001). Work function measurements on indium tin oxide films. **J Electron Spect Rel Phen. ens.** 120: 149-154.

Seung, Ik H., and Hong, Bae K. (2016). A study on properties of RF-sputtered Al-doped ZnO thin hilms prepared with different Ar gas flow rates, **Appl. Sci. Converg. Technol**. 25: 145-148.

Severin, P. J. (1971). Four-point-probe resistivity measurements on silicon heterotype epitaxial layers with altered probe orper. **Philips Res. Repts.** 26: 279-297.

Shan, F. K., Liu, G. X., Lee, W. J., and Shin, B. C. (2007). The role of oxygen vacancies in epitaxial-deposited ZnO thin films. **J. Appl. Phys.** 101: 053106.

Shanting, Z. (2017). **Study of fluorine-doped tin oxide (FTO) thin films for photovoltaics applications.** English: Université Grenoble Alpes; Technische Universität (Darmstadt, Allemagne).

Silva, R., Maria, E., and Zani, Q. (2004). Aluminum-doped zinc oxide films prepared by an inorganic sol.gel route. **Thin Solid Films.** 449: 86-93.

Song, C., Lin, Z., Zhang, Y., Wang, X., Guo, Y., Song, J., and Huang, R. (2016). Investigation of structure, optical an electrical characterization of AZO films used for solar cells. **Key Eng. Mater.** 703: 214-218.

Song, W., So, S. K., and Cao, L. (2001). Angular-dependent photoemission studies of indium tin oxide surfaces **Appl. Phys. A.** 72: 361-365.

Tabassum, S., Yamasue, E., Okumura, H., and Ishihara, K. N. (2014). Damp heat stability of AZO transparent electrode and influence of thin metal film for enhancing the stability. **J Mater Sci: Mater Electron.** 25: 3203-3208.

Takashi, T., and Mitsuji, H. (2000). Influence of oxygen partial pressure on transparency and conductivity of RF sputtered Al-doped ZnO thin films. **Appl. Surf. Sci.** 157: 47-51.

Tang, F., Liu, D. L., and Ye, D. X. (2003). Magnetic properties of Co nanocolumns fabricated by oblique-angle deposition. **Journal of Applied Physics.** 93: 4194-4200.

Tang, F., Parker, T., Wang, G-C., and Lu, T-M. (2007). Surface texture evolution of polycrystalline and nanostructured films: RHEED surface pole figure analysis. **J. Phys. D: Appl. Phys.** 40: R427-R439

Tanusevskia, A., and Georgieva, V. (2010). Optical and electrical properties of nanocrystal zinc oxide films prepared by dc magnetron sputtering at different sputtering pressures. **Appl Surface Sci.** 5: 19964-19965.

Travis, B., and Farinaz, H. (2013). **High volume optical component testing using an Agilent Cary 7000 Universal Measurement Spectrophotometer (UMS) with Solids Autosampler.** Australia: Agilent Technologies.

Valenti, I., Benedetti, S., di Bona, A., Lollobrigida, V., Perucchi, A., Di Pietro, P., Lupi, S., Valeri, S., and Torelli, P. (2015). Electrical, Optical, and electronic properties of Al:ZnO film in a wide doping range. **J. Appl. Phys.** 118: 165304.

Vera, K. (2006). **Electron diffraction structure analysis: Specimens and their electron diffraction patterns.** Netherlands. Springer.

Vick, D., Friedrich, L. J., Dew, S. K., Brett, M. J., Robbie, K., Seto, M., and Smy, T. (1999). Self-shadowing and surface diffusion effects in obliquely deposited thin flms. **Thin Solid Films.** 339: 88-94.

Waits, R. K., and Vac, J. (2000). Erratum: "Evolution of integrated-circuit vacuum processes: 1959–1975". **Sci. Technol. A.** 18: 1736.

Wei, H., Liu, Z., and Yao, K. (1999). Monte Carlo simulation of thin-film growth on a surface with a triangular lattice. **Vacuum.** 52: 435-440.

Weiyan, W., Quanyu, F., Kemin, J., Jinhua, H., Xianpeng, Z., Weijie, S., and Ruiqin, T. (2011). Dependence of aluminum-doped zinc oxide work function on surface cleaning method as studied by ultraviolet and X-ray photoelectron spectroscopies. **Appl Surf Sci.** 257: 3884-3887.

Yildiz, A., Cansizoglu, H., Abdulrahman, R., and Karabacak, T. (2015). Effect of grain size and strain on the bandgap of glancing angle deposited AZO nanostructures. **J Mater Sci.** 26: 5952-5957.

Yildiz, A., Cansizoglu, H., Turkoz, M., Abdulrahman, R., Al-Hilo, A., Cansizoglu, M. F., Demirkan, T. M., and Karabacak, T. (2015). Glancing angle deposited Al-doped ZnO nanostructures with different structural and optical properties. **Thin Solid Films.** 589: 764-769.

Ýlker, A., and Hüseyýn, T. (2001). Optical Transmission Measurements on Glow-Discharge Amorphous Silicon Nitride Films. **Turk. J. Phy.** 25: 215-222.

Youn, J. K., Su, B. J., Sung, I. K., Yoon, S. C., In, S. C., and Jeon, G. H. (2010). Effect of oxygen flow rate on ITO thin films deposited by facing targets sputtering. **Thin Solid Films.** 518: 6241-6244.

Zhang, W., Xiong, J., Liu, L., Zhang, X., and Gu, H. (2016). Influence of annealing temperature on structural, optical and electrical properties of AZO/Pd/AZO films. **Sol. Energ. Mat. Sol. C.** 153: 52-60.

Zhdanov, G. S. (1965). **Crystal physics.** London: Oliver & Body.

Zhou, Q., Li, Z., Ni, J., and Zhang, Z. (2011). A Simple Model to Describe the Rule of Glancing Angle Deposition. **Mater. Trans.** 52: 469-473.

APPENDICES
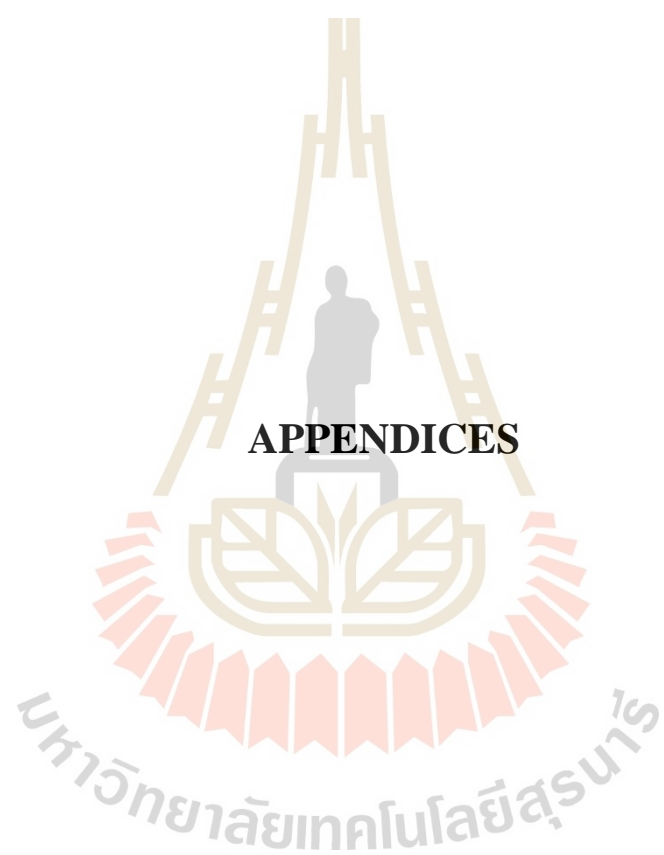
APPENDIX A

NOTATION FOR XPS

XPS measure the energy of electrons emitted from a material. It is necessary, therefore, to have some formalism to describe which electron is involved with each of the observed transitions. XPS uses the so-called spectroscopists' or chemists' notation while Auger electrons are identified by the X-ray notation.

1. Spectroscopists' notation

In this notation, the photoelectrons observed are described by means of their quantum numbers. Transitions are usually labeled according to the scheme nl_j. The first part of this notation is the principal quantum number, n. This takes integer values of 1, 2, 3 etc. The second part of the nomenclature, l, is the quantum number which describes the orbital angular momentum of the electron. This takes integer values 0, 1, 2, 3 etc. However, this quantum number is usually given a letter rather than a number as shown in Table 1.

Table A.1 Notation given to the quantum numbers which describe orbital angular momentum.

Value of l	Usual notation
0	**s**
1	**p**
2	**d**
3	**f**

The peak in XPS spectra, derived from orbitals whose angular momentum quantum number is greater than 0, are usually split into two. This is a result of the interaction of the electron angular momentum due to its spin with its orbital angular momentum. Each electron has a quantum number associated with its spin angular momentum, s^2. The value of s can be either +1/2 or -1/2. The two angular momenta are added vectorially to produce the quantity j in the expression nl_j, i.e., $j = |l + s|$. Thus, an electron from a **p** orbital can have a j value of 1/2 ($l + s$) or 3/2 ($l + s$); similarly, electron from a **d** orbital can have j values of either 3/2 or 5/2. The relative intensity of the components of the doublets formed by the spin orbit coupling is dependent upon their relative population (degeneracies) which are given by the expression ($2j$+1) so, for an electron from a **d** orbital, the relative intensities of the 3/2 and 5/2 peaks are 2:3. The spacing between the components of the doublets depends upon the strength of the spin orbit coupling. For a given value of both n and l the separation increases with the atomic number of the atom. For a given atom, it decrease both with increasing n and with increasing l. Figure 1 shows an XPS spectrum from AZO with the peaks labeled according to this notation and illustrating the splitting observed in the peaks due to electrons in Zn3s, Zn3p and Zn3d orbitals while the peaks in the Al2p and O2p peaks are too small to be observed.
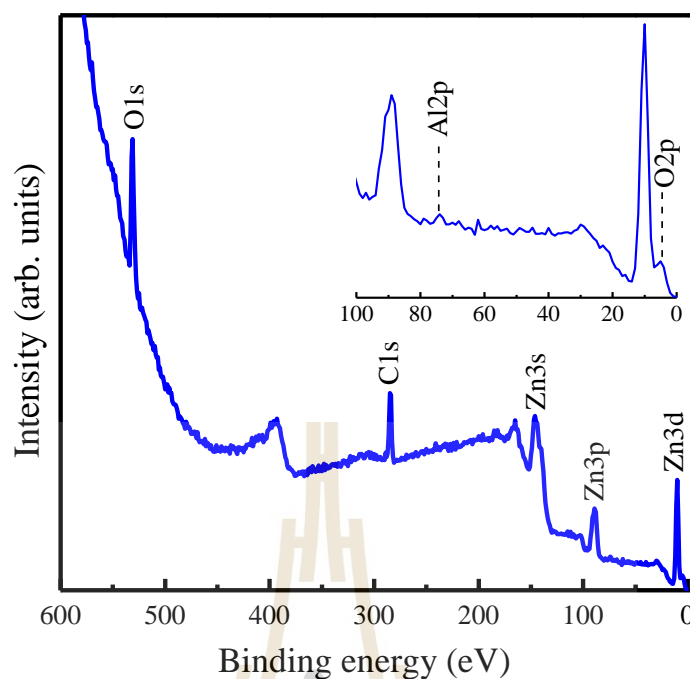
Figure A.1 Survey spectrum from AZO showing the XPS transition accessible using soft X-ray radiation, the features marked with an asterisk are electron energy loss features due to plasmon excitation.

2. X-ray notation

In X-ray notation, the principle quantum numbers are given letters *K*, *L*, *M*, etc. while subscript numbers refer to the j values described above. The relationship between the notations is giving in Table 2. As well be seen later, the Auger process involves three electrons and so the notation has to take account of this. This is done simply by listing the three electrons; a peak in an Auger spectrum may be labelled, for example, KL_1L_3 or $L_2M_5M_5$. For convenience, the subscripts are sometimes omitted.

Table A.2 the relationship between quantum numbers, spectroscopists' notation and X-ray notation.

Quantum numbers				Spectroscopists'	X-ray
n	l	s	j	notation	notation
1	0	+1/2, -1/2	1/2	$1s_{1/2}$	K
2	0	+1/2, -1/2	1/2	$2s_{1/2}$	L_1
2	1	+1/2	1/2	$2p_{1/2}$	L_2
2	1	-1/2	3/2	$2p_{3/2}$	L_3
3	0	+1/2, -1/2	1/2	$3s_{1/2}$	M_1
3	1	+1/2	1/2	$3p_{1/2}$	M_2
3	1	-1/2	3/2	$3p_{3/2}$	M_3
3	2	+1/2	3/2	$3d_{3/2}$	M_4
3	2	-1/2	5/2	$3d_{5/2}$	M_5
					etc.

APPENDIX B

XRD STANDARD AND THE RELATIVE ENERGY

Table B.1 The data reference of crystal structure plane and d-spacing of AZO films.

2-Theta	d-spacing	(	h	k	l)	Material	2-Theta	d-spacing	(	h	k	l)	Material
18.982	4.6714	(	1	1	1)	AZO	66.398	1.4068	(	2	0	0)	ZnO
25.572	3.4806	(	0	1	2)	Al_2O_3	66.507	1.4048	(	2	1	4)	Al_2O_3
31.242	2.8607	(	2	2	0)	AZO	67.971	1.378	(	1	1	2)	ZnO
31.778	2.8136	(	1	0	0)	ZnO	68.197	1.374	(	3	0	0)	Al_2O_3
34.434	2.6025	(	0	0	2)	ZnO	68.558	1.3677	(	5	3	1)	AZO
35.146	2.5514	(	1	0	4)	Al_2O_3	69.11	1.3581	(	2	0	1)	ZnO
36.265	2.4751	(	1	0	1)	ZnO	69.669	1.3485	(	4	4	2)	AZO
36.812	2.4396	(	3	1	1)	AZO	70.405	1.3362	(	1	2	5)	Al_2O_3
37.77	2.3799	(	1	1	0)	Al_2O_3	72.595	1.3012	(	0	0	4)	ZnO
38.48	2.3376	(	1	1	1)	Al	74.042	1.2793	(	6	2	0)	AZO
38.512	2.3357	(	2	2	2)	AZO	74.29	1.2757	(	2	0	8)	Al_2O_3
41.673	2.1656	(	0	0	6)	Al_2O_3	76.864	1.2392	(	1	0	10)	Al_2O_3
43.347	2.0857	(	1	1	3)	Al_2O_3	76.987	1.2376	(	2	0	2)	ZnO
44.73	2.0244	(	2	0	0)	Al	77.225	1.2344	(	1	1	9)	Al_2O_3
44.768	2.0228	(	4	0	0)	AZO	77.259	1.2339	(	5	3	3)	AZO
46.171	1.9645	(	2	0	2)	Al_2O_3	78.247	1.2208	(	3	1	1)	Al
47.555	1.9105	(	1	0	2)	ZnO	78.321	1.2198	(	6	2	2)	AZO
49.036	1.8562	(	3	3	1)	AZO	80.406	1.1933	(	2	1	7)	Al_2O_3
52.543	1.7403	(	0	2	4)	Al_2O_3	80.684	1.1899	(	2	2	0)	Al_2O_3
55.601	1.6516	(	4	2	2)	AZO	81.418	1.181	(	1	0	4)	ZnO
56.613	1.6245	(	1	1	0)	ZnO	82.455	1.1688	(	2	2	2)	Al
57.491	1.6017	(	1	1	6)	Al_2O_3	82.535	1.1679	(	4	4	4)	AZO
59.298	1.5572	(	5	1	1)	AZO	83.202	1.1602	(	0	3	6)	Al_2O_3
59.73	1.5469	(	2	1	1)	Al_2O_3	84.34	1.1474	(	2	2	3)	Al_2O_3
61.12	1.515	(	1	2	2)	Al_2O_3	85.124	1.1388	(	1	3	1)	Al_2O_3
61.295	1.5111	(	0	1	8)	Al_2O_3	85.668	1.133	(	7	1	1)	AZO
62.88	1.4768	(	1	0	3)	ZnO	86.335	1.1259	(	3	1	2)	Al_2O_3
65.111	1.4315	(	2	2	0)	Al	86.489	1.1243	(	1	2	8)	Al_2O_3
65.169	1.4303	(	4	4	0)	AZO	88.984	1.0992	(	0	2	10)	Al_2O_3

Table B.1 The data reference of crystal structure plane and d-spacing of AZO films.
(Continued)

2-Theta	d-spacing	(	h	k	l)	Material	2-Theta	d-spacing	(	h	k	l)	Material
89.647	1.0927	(	2	0	3)	ZnO	116.585	0.9054	(	0	1	14)	Al_2O_3
90.698	1.0828	(	0	0	12)	Al_2O_3	116.605	0.9053	(	4	2	0)	Al
90.865	1.0812	(	6	4	2)	AZO	116.753	0.9046	(	8	4	0)	AZO
91.171	1.0784	(	1	3	4)	Al_2O_3	117.821	0.8995	(	4	1	0)	Al_2O_3
92.827	1.0635	(	2	1	0)	ZnO	120.182	0.8886	(	2	3	5)	Al_2O_3
93.984	1.0534	(	7	3	1)	AZO	120.3	0.8881	(	7	5	3)	AZO
94.801	1.0465	(	3	1	5)	Al_2O_3	121.51	0.8828	(	8	4	2)	AZO
95.231	1.0429	(	2	2	6)	Al_2O_3	121.624	0.8823	(	3	0	2)	ZnO
95.343	1.0419	(	2	1	1)	ZnO	122.003	0.8807	(	4	1	3)	Al_2O_3
98.373	1.0178	(	0	4	2)	Al_2O_3	124.565	0.8701	(	0	4	8)	Al_2O_3
98.66	1.0156	(	1	1	4)	ZnO	125.237	0.8675	(	0	0	6)	ZnO
99.107	1.0122	(	4	0	0)	Al	126.524	0.8625	(	6	6	4)	AZO
99.213	1.0114	(	8	0	0)	AZO	127.652	0.8583	(	1	3	10)	Al_2O_3
101.058	0.9979	(	2	1	10)	Al_2O_3	129.849	0.8505	(	0	3	12)	Al_2O_3
102.386	0.9885	(	7	3	3)	AZO	130.507	0.8482	(	9	3	1)	AZO
102.809	0.9856	(	1	1	12)	Al_2O_3	131.076	0.8463	(	2	0	14)	Al_2O_3
102.976	0.9844	(	2	1	2)	ZnO	132.178	0.8426	(	3	2	7)	Al_2O_3
103.294	0.9823	(	4	0	4)	Al_2O_3	132.594	0.8413	(	2	1	13)	Al_2O_3
103.452	0.9812	(	6	4	4)	AZO	134.006	0.8368	(	2	0	5)	ZnO
104.183	0.9763	(	1	0	5)	ZnO	136.034	0.8307	(	1	4	6)	Al_2O_3
104.619	0.9734	(	1	3	7)	Al_2O_3	136.625	0.829	(	1	0	6)	ZnO
107.487	0.9553	(	2	0	4)	ZnO	137.511	0.8265	(	4	2	2)	Al
107.766	0.9536	(	8	2	2)	AZO	137.746	0.8258	(	8	4	4)	AZO
109.515	0.9432	(	3	2	1)	Al_2O_3	138.607	0.8234	(	2	1	4)	ZnO
109.841	0.9413	(	1	2	11)	Al_2O_3	139.329	0.8215	(	3	1	11)	Al_2O_3
110.434	0.9379	(	3	0	0)	ZnO	140.975	0.8172	(	2	3	8)	Al_2O_3
110.966	0.9349	(	3	1	8)	Al_2O_3	142.284	0.814	(	1	1	15)	Al_2O_3
111.07	0.9343	(	7	5	1)	AZO	142.613	0.8132	(	7	7	1)	AZO
112.052	0.9289	(	3	3	1)	Al	143.019	0.8122	(	2	2	0)	ZnO
112.187	0.9281	(	6	6	2)	AZO	145.123	0.8074	(	4	0	10)	Al_2O_3
114.046	0.9182	(	2	2	9)	Al_2O_3	148.243	0.8009	(	2	2	12)	Al_2O_3
116.071	0.908	(	3	2	4)	Al_2O_3	149.153	0.7991	(	0	5	4)	Al_2O_3
116.331	0.9067	(	2	1	3)	ZnO							

Table B.2 the relative solar energy of the standard spectrum distribution for solar

energy as specified in the visible wavelength.

Wavelength (nm)	Relative Energy
380	2.06
400	3.00
420	4.02
440	4.55
460	5.56
480	5.83
500	5.71
520	5.50
540	5.46
560	5.27
580	5.40
600	5.30
620	5.25
640	5.20
660	5.12
680	5.00
700	4.89
720	4.73
740	4.57
760	3.32
780	4.27

APPENDIX C

PUBLICATION AND PRESENTATIONS

Conferences presentation

1) SPC 2016 Ubon Ratchthani Thailand: Growth and Characterizations of AZO Thin Films by Pulsed DC Magnetron Sputtering. (Oral presentation)

2) International Conference on Science and Technology of Emerging Materials (STEMa2016): Effects of Sputtering Power Towards the AZO Thin Film Prepared by Pulsed. (Oral presentation)

3) The 4th Southeast Asia Conference on Thermoelectrics, Sea Garden Hotel, Danang, Vietnam: Glancing-angle pulsed dc magnetron sputtered AZO thin films for TCO applications. (Oral presentation)

4) The 3rd International Conference on Applied Physics and Material Application (ICAPMA2017): A Comparative Study of Glancing-Angle Deposited AZO Thin Films from Magnetron Sputtering Deposition. (Oral presentation)

5) The first Materials Research Society of Thailand International Conference (1st MRS Thailand International Conference): Structural, optical and electrical properties of transparent conductive AZO thin films prepared by pulsed DC magnetron sputtering. (Oral presentation / Best Oral Presentation Award)

6) AUM2018: The Investgation of Glancing-Angle Deposited AZO Thin Films Prepared by Pulsed DC Magnetron Sputtering. (Poster presentation)

7) 2ndInternational Conference on Science and Technology of Emerging Materials (STEMa2018): The Transparen Conductive Nanocolumnar AZO Film Coating by GLAD. (Oral presentation)

8) 7th International Symposium on Transparent on Conductive Materials (TCM 2018) Minoa Palace Hotel, Platanias – Chania, Crete, Greece : Effects of Post Annealing Treatment on Vertically Aligned Nanocolumnar AZO Thin Films Fabricated by Glancing Angle Deposition Technique. (Oral presentation)

9) The 2nd Materials Research Society of Thailand International Conference (MRS-Thailand 2019): Influence of vacuum annealing temperature on structural, optical and electrical of nanocolumnar AZO films for TCO application. (Oral presentation / Best Oral Presentation Award)

Journal publication

1) Kittikhun, S., Mati, H., Pitak, E., Viyapol, P., Saksorn, L, Pennapa, M, Chanchana, T., and Prayoon, S. (2017). Effects of sputtering power toward the Al-doped ZnO thin Film prepared by pulsed DC magnetron sputter. **Mater. Today-Proc.** 4: 6466-6471.

2) Kittikhun, S., Mati, H., Pitak, E., Viyapol, P., Saksorn, L., Pennapa, M., Chanchana, T., Hideki, N., and Prayoon, S. (2017). Structural, optical and electrical properties of transparent conductive AZO thin films prepared by pulsed DC magnetron sputtering. **MRS Thailand International Con. Proc.** 1: 366-371.

3) Kittikhun, S., Mati, H., Pitak, E., Viyapol, P., Saksorn, L., Pennapa, M., Chanchana, T., and Prayoon, S. (2018). Glancing-angle pulsed dc magnetron sputtered AZO thin films for TCO applications. **Mater. Today-Proc.** 5: 14166-14171.

4) Kittikhun, S., Mati, H., Pitak, E., Viyapol, P., Saksorn, L., Pennapa, M., Chanchana, T., and Prayoon, S. (2018). Transparent conductive nanocolumnar AZO film coating by glancing angle deposition Technique. **AIP Conf. Proc.** 2010: 020017-1-020017-5.

5) Kittikhun, S., Mati, H., Pitak, E., Viyapol, P., Saksorn, L., Chanunthorn, C., Pennapa, M., Chanchana, T., Annop, K., Tuksadon, W., Hideki, N., Miskawan, S., and Prayoon, S. (2020). Influence of vacuum annealing temperature on structural, optical and electrical of nanocolumnar AZO films for TCO application. **Chiang Mai J. Sci.** 47.

6) Lertvanithphol, T., Rakreungdet, W., Chanunthorn, C., Pitak, E., Saksorn, L., Nuntawong, N., Viyapol, P., Klamchuen, A., Khemasiri, N., Nukeaw, J., Kittikhun, S., Songsiriritthigul, C., Chanlek, N., Hideki, N., Prayoon, S., and Mati, H. (2019). Spectroscopic study on amorphous tantalum oxynitride thin films prepared by reactive gas-timing RF magnetron sputtering. **Appl. Surf. Sci**. 19: 31915.

7) Lomon, J., Chaiyabin, P., Saisopa, T., Kittikhun, S., Saowiang, N., Promsakha, K., Poolcharuansin, P., Pasaja, N., Chingsungnoen, A., Supruangnet, R., Chanlek, N., Hideki, N., and Prayoon, S. (2018). XPS and XAS preliminary studies of diamond-like carbon films prepared by HiPIMS technique. **J. Phys. Conf. Ser.** 1144.

8) Miskawan, S., Songsiriritthigul, C., Mothong, N., Kittikhun S., Saisopa1, T., Mati, H., and Prayoon, S. (2018). Grazing Incident X-Ray Diffraction using Synchrotron Light at SLRI. **J. Phys. Conf. Ser.** 1144.

CURRICULUM VITAE

1. Name /Nationality: Mr. Kittikhun Seawsakul/ Thailand

2. Date & County of Birth: 24 September 1985/ Thailand

3. Education: 2008, B.Sc. in Wood Science and Technology, Kasetsart University.

2014, M.Sc. in Physics, Ubon Ratchathani University. Thailand

4. Current Position: PhD. student, School of Physics, Suranaree University of

Technology.

5. Work experience:

2008 Assistance process engineering at PRIME BOX MFG. LTD. Company.

2009 Forestry academics at Department of National Parks, Wildlife and Plant

Conservation.

2010 QC and R&D at Vanachai Group (VNG).

2011 Teacher at Sripatum Pittayakarn School and Demonstration Pali School Ubon.

2015-2019 PhD. Student Research at Optical Thin-Film Technology Laboratory

(OTL) at NECTEC

2019-Present PhD. Student Research Assistant at BL 3.2: PES Techniques beamline

at Synchrotron Light Research Institute (Public Organization).